Posted on 25 May 2023 — The copyright holder is the author/funder. All rights reserved. No reuse without permission. — https://doi.org/10.22541/essoar.168500350.09716718/v1 — This a preprint and has not been peer reviewed. Data may be preliminary.

Dynamics of oceanic slab tearing during transform-fault horizontally-oblique subduction: Insights from 3D numerical modeling

Jie Xin[1], Huai Zhang[1], Felipe Orellana-Rovirosa[2], Zhong-Hai Li[1], Liang Liu[3], Yigang Xu[3], Zhen Zhang[1], and Yaolin Shi[4]

[1]University of Chinese Academy of Sciences
[2]Ocean Science and Engineering department, Southern China University of Science and Technology, Shenzhen 518055, P. R. China
[3]Guangzhou Institute of Geochemistry, Chinese Academy of Sciences
[4]University of Chinese Academy of Science

May 25, 2023

Abstract

Oceanic-plates vertical tearing is seismically-identified in the present-day Earth. This type of plate tearing is frequently reported in horizontally-oblique subduction zones where transform-faulted oceanic plates are subducting (or subducted). However, the mechanisms behind vertical slab tearing are still poorly understood, thus we utilize 3D time-dependent Stokes' flow thermo-mechanical models to further study this problem. We find that (i) the age offset of transform fault and (ii) the horizontal obliqueness of subduction fundamentally control the tearing behavior of two generic, materially-homogeneous oceanic slabs separated by a low-viscosity zone. The overriding-continental plate bends one slab first, which combined with the age-thickness difference between slabs, causes the differential sinking of them. Based on the modeling results, well-developed slabs vertical tearing would happen when the oblique angle of subduction is [?]30° or the age ratio of the secondly-bent to firstly-bent slab being ˜<0.6. Quantifying the horizontal distance-vector between sinking slabs, we find that subduction at medium-low horizontal-obliqueness angles ([?]30deg) of young lithosphere (slabs-average ˜15 Myr) tends to produce fault-perpendicular tearing. Contrastingly, old-age slabs (average [?] 30 Myr) with medium-large obliqueness angles (˜>20deg) tend to produce fault-parallel tearing, related to differential slab-hinge retreat or rollback. Correlations between slabs' (i) computed tearing horizontal-width and (ii) scaling-theory forms of their subduction-velocity differences, are reasonable (0.76-0.97). Our numerically-predicted scenarios are reasonably consistent with plate-tear imaging results from at least 4 natural subduction zones. Our modeling also suggests that continual along-trench variation in subduction dip angle may be related to a special case of oblique subduction.

Posted on 25 May 2023 — The copyright holder is the author/funder. All rights reserved. No reuse without permission. — https://doi.org/10.22541/essoar.168500350.09716718/v1 — This a preprint and has not been peer reviewed. Data may be preliminary.

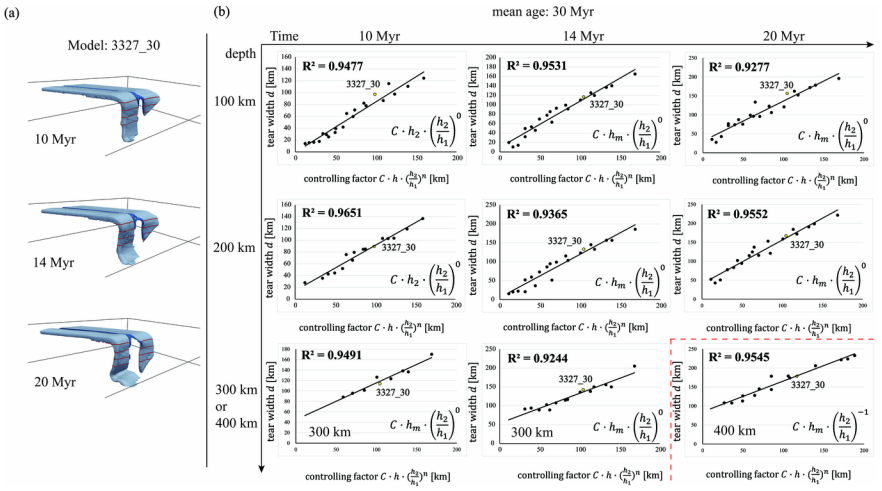

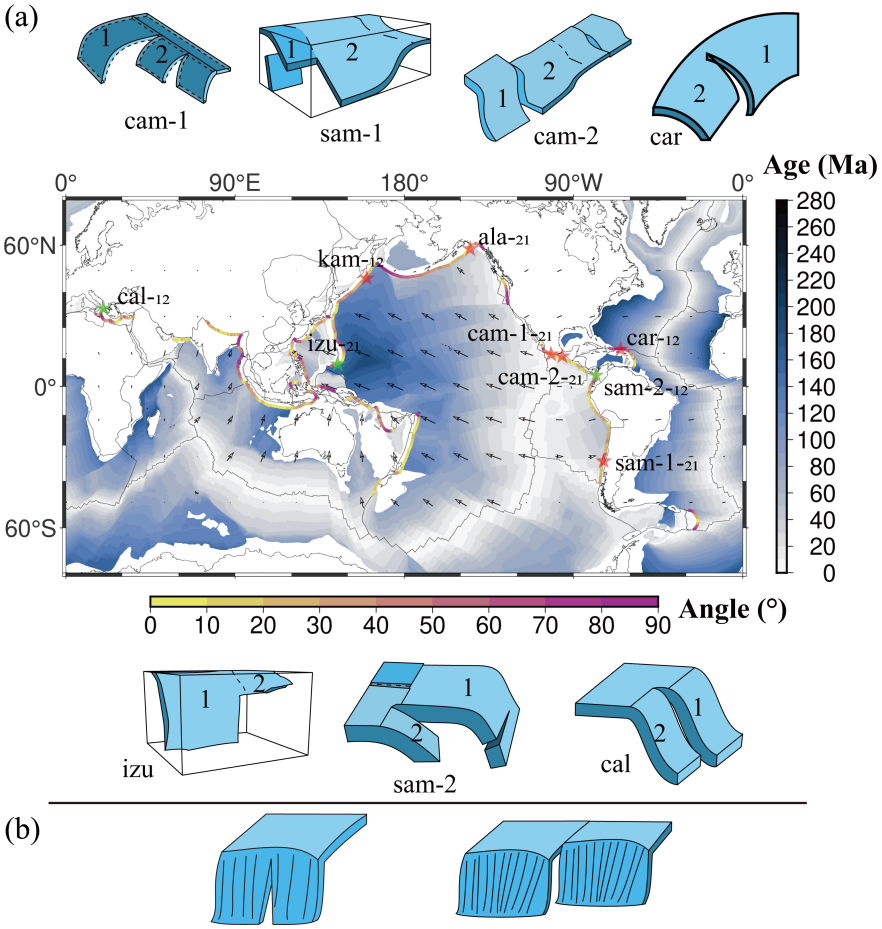

Posted on 25 May 2023 — The copyright holder is the author/funder. All rights reserved. No reuse without permission. — https://doi.org/10.22541/essoar.168500350.09716718/v1 — This a preprint and has not been peer reviewed. Data may be preliminary.

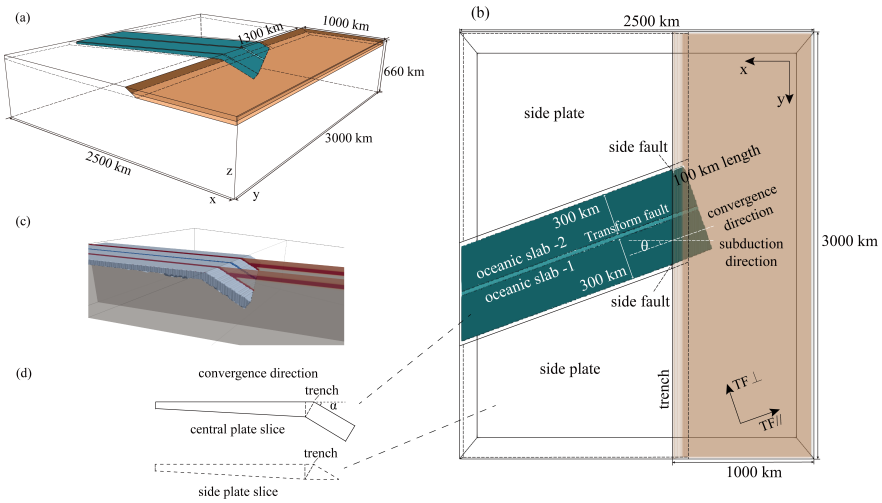

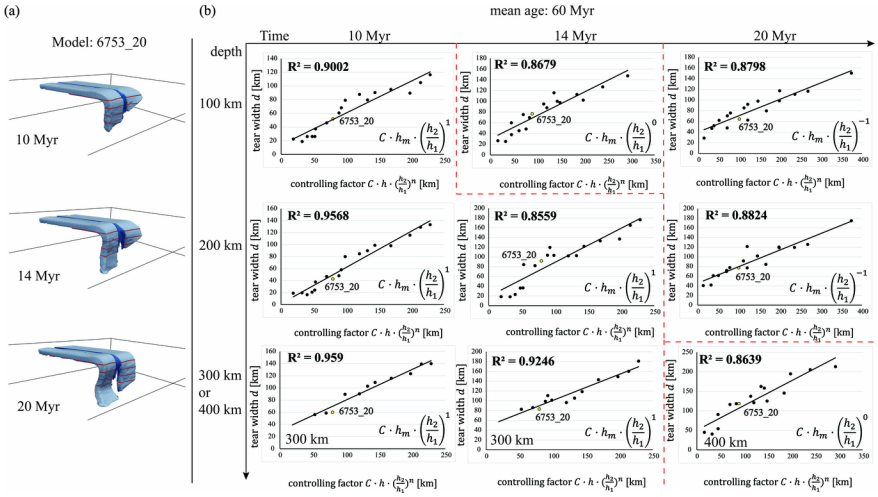

Posted on 25 May 2023 — The copyright holder is the author/funder. All rights reserved. No reuse without permission. — https://doi.org/10.22541/essoar.168500350.09716718/v1 — This a preprint and has not been peer reviewed. Data may be preliminary.

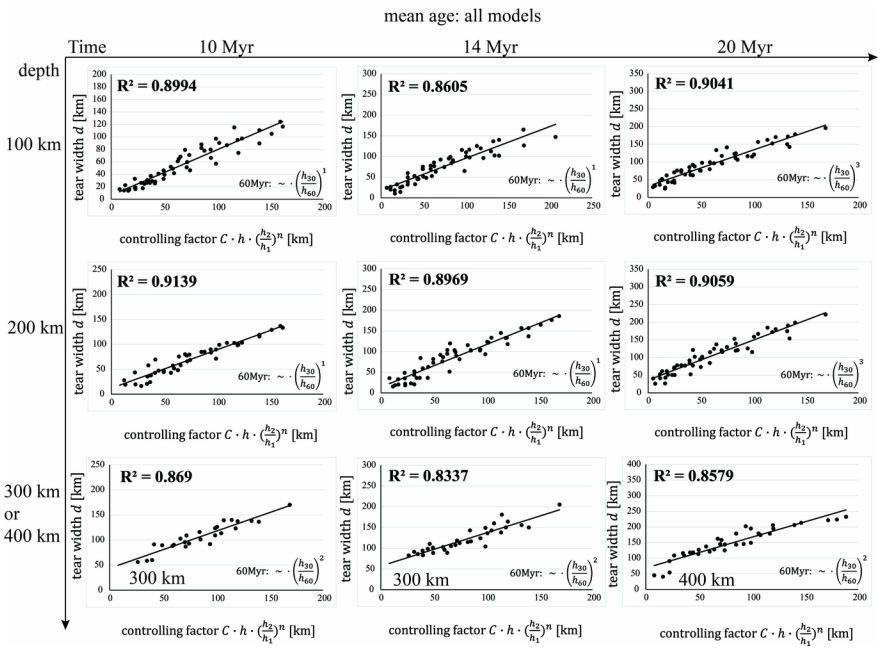

Posted on 25 May 2023 — The copyright holder is the author/funder. All rights reserved. No reuse without permission. — https://doi.org/10.22541/essoar.168500350.09716718/v1 — This a preprint and has not been peer reviewed. Data may be preliminary.

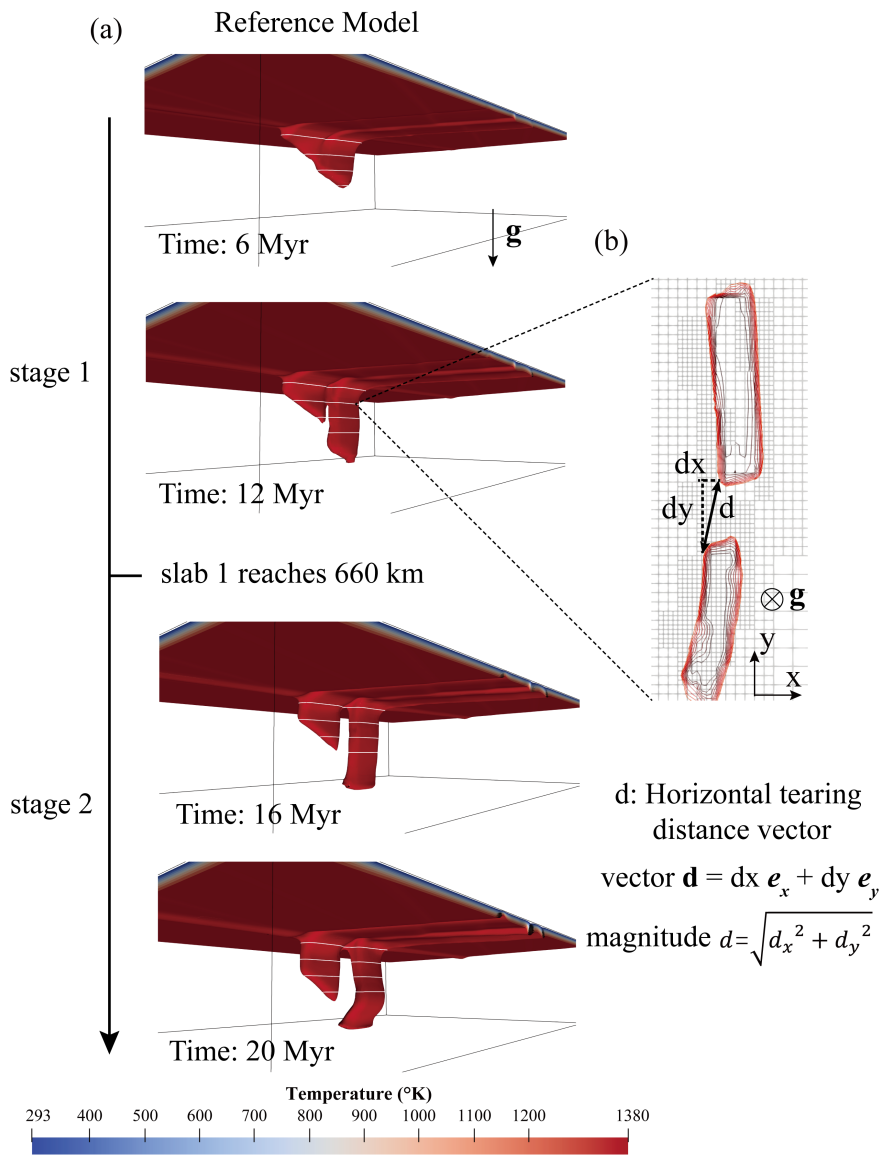

Posted on 25 May 2023 — The copyright holder is the author/funder. All rights reserved. No reuse without permission. — https://doi.org/10.22541/essoar.168500350.09716718/v1 — This a preprint and has not been peer reviewed. Data may be preliminary.

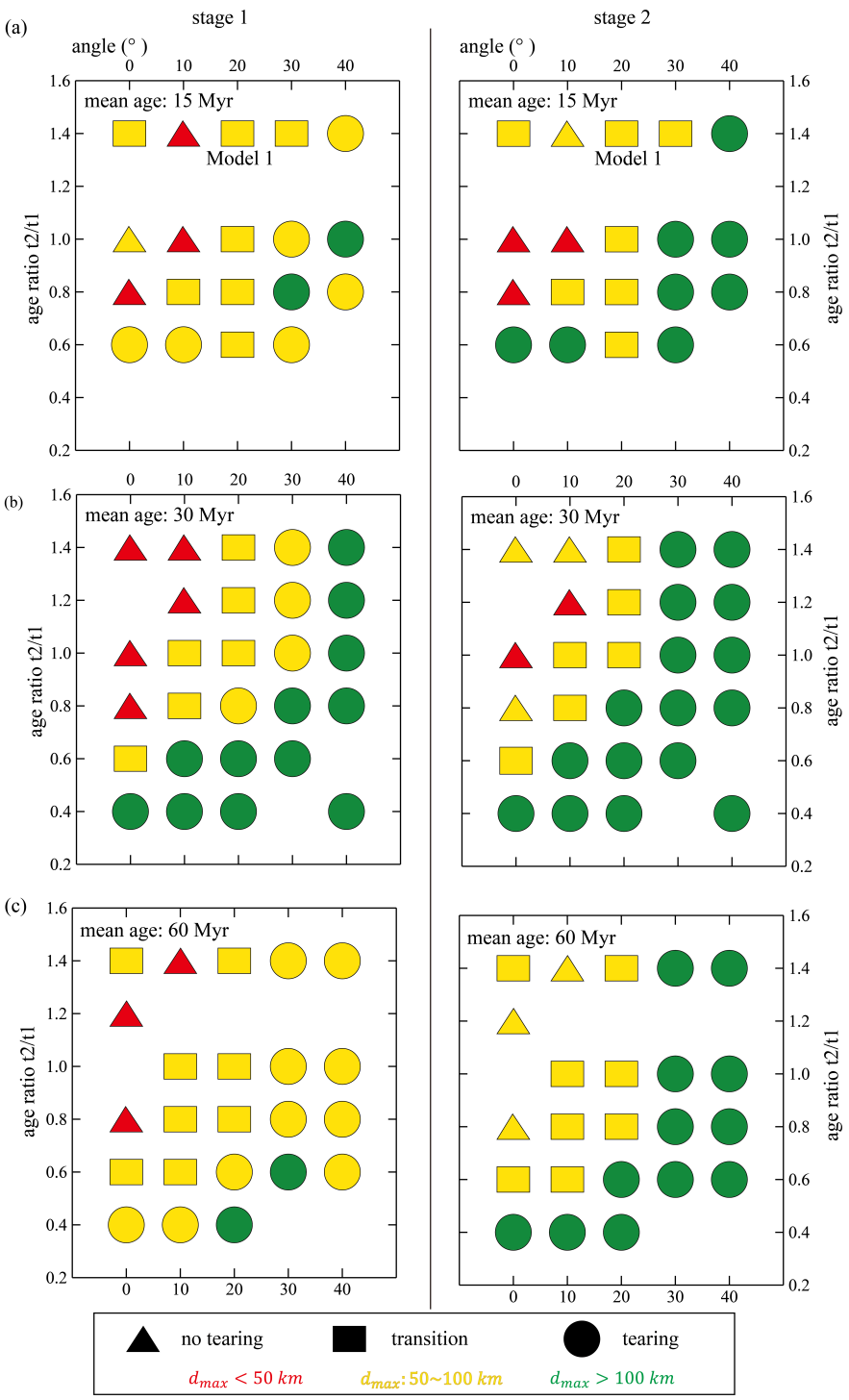

Posted on 25 May 2023 — The copyright holder is the author/funder. All rights reserved. No reuse without permission. — https://doi.org/10.22541/essoar.168500350.09716718/v1 — This a preprint and has not been peer reviewed. Data may be preliminary.

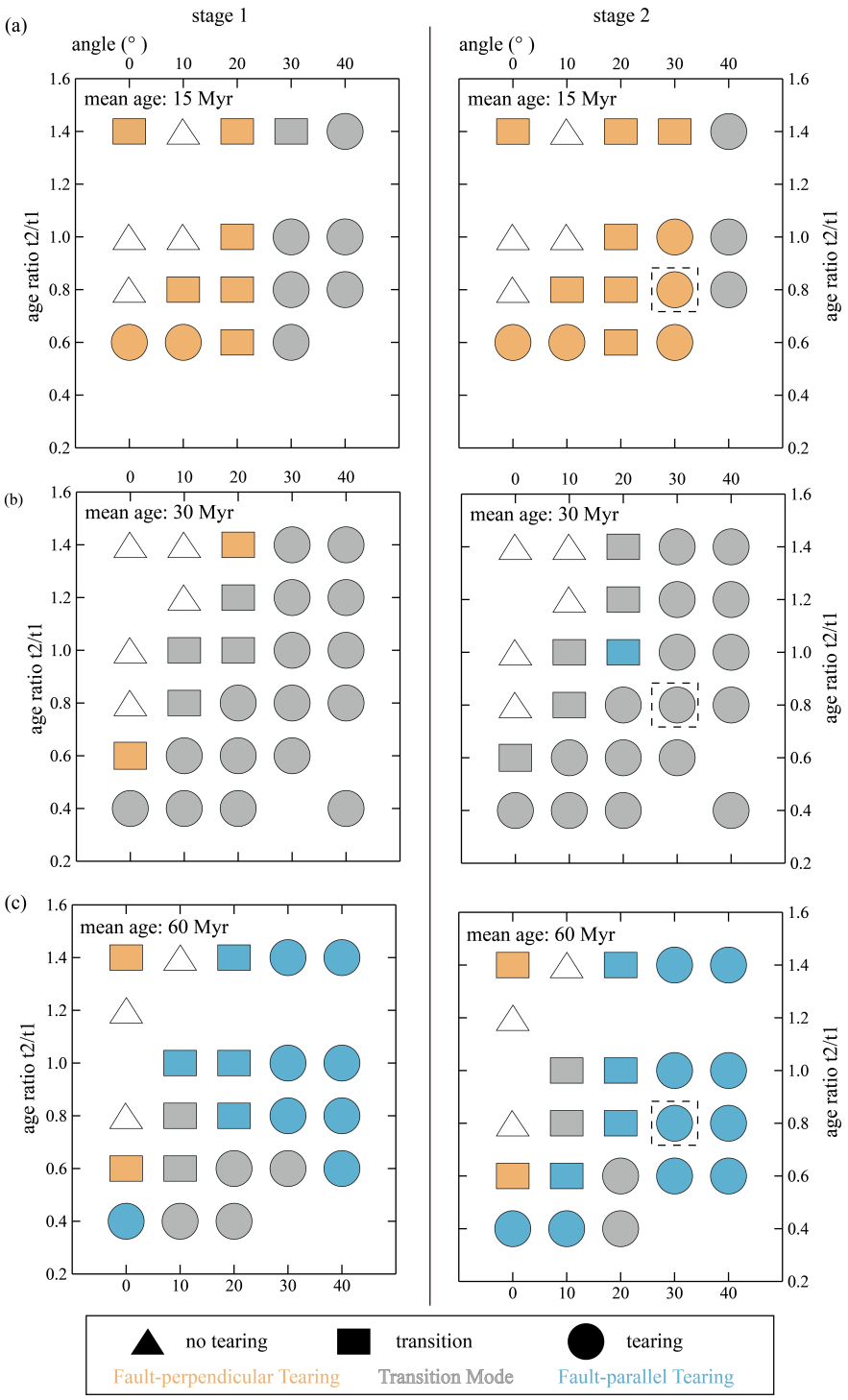

Posted on 25 May 2023 — The copyright holder is the author/funder. All rights reserved. No reuse without permission. — https://doi.org/10.22541/essoar.168500350.09716718/v1 — This a preprint and has not been peer reviewed. Data may be preliminary.

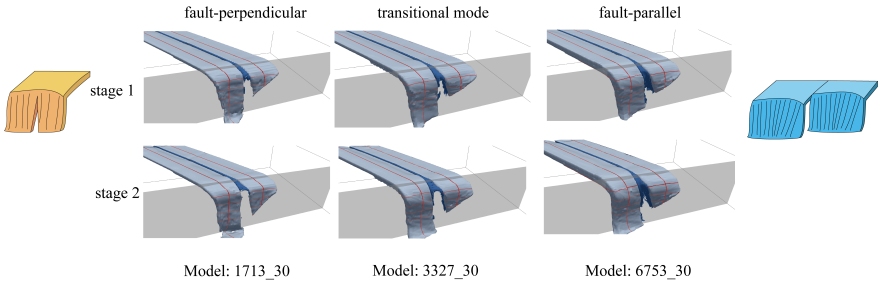

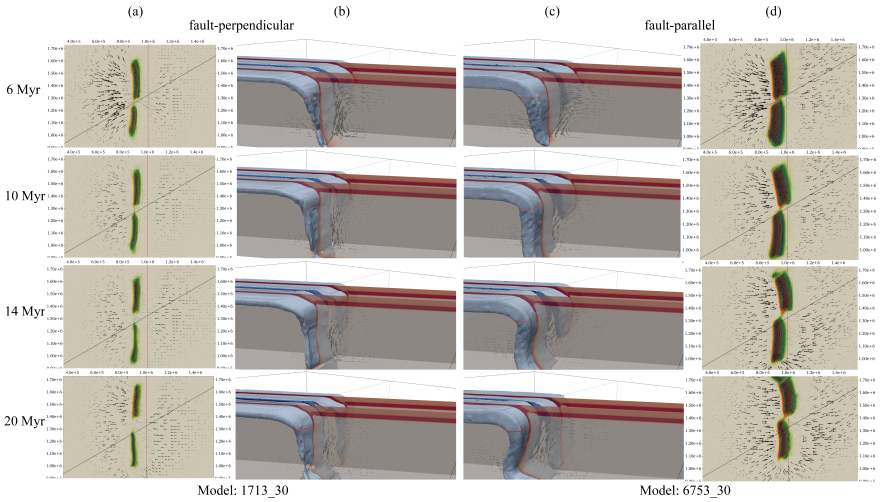

Posted on 25 May 2023 — The copyright holder is the author/funder. All rights reserved. No reuse without permission. — https://doi.org/10.22541/essoar.168500350.09716718/v1 — This a preprint and has not been peer reviewed. Data may be preliminary.

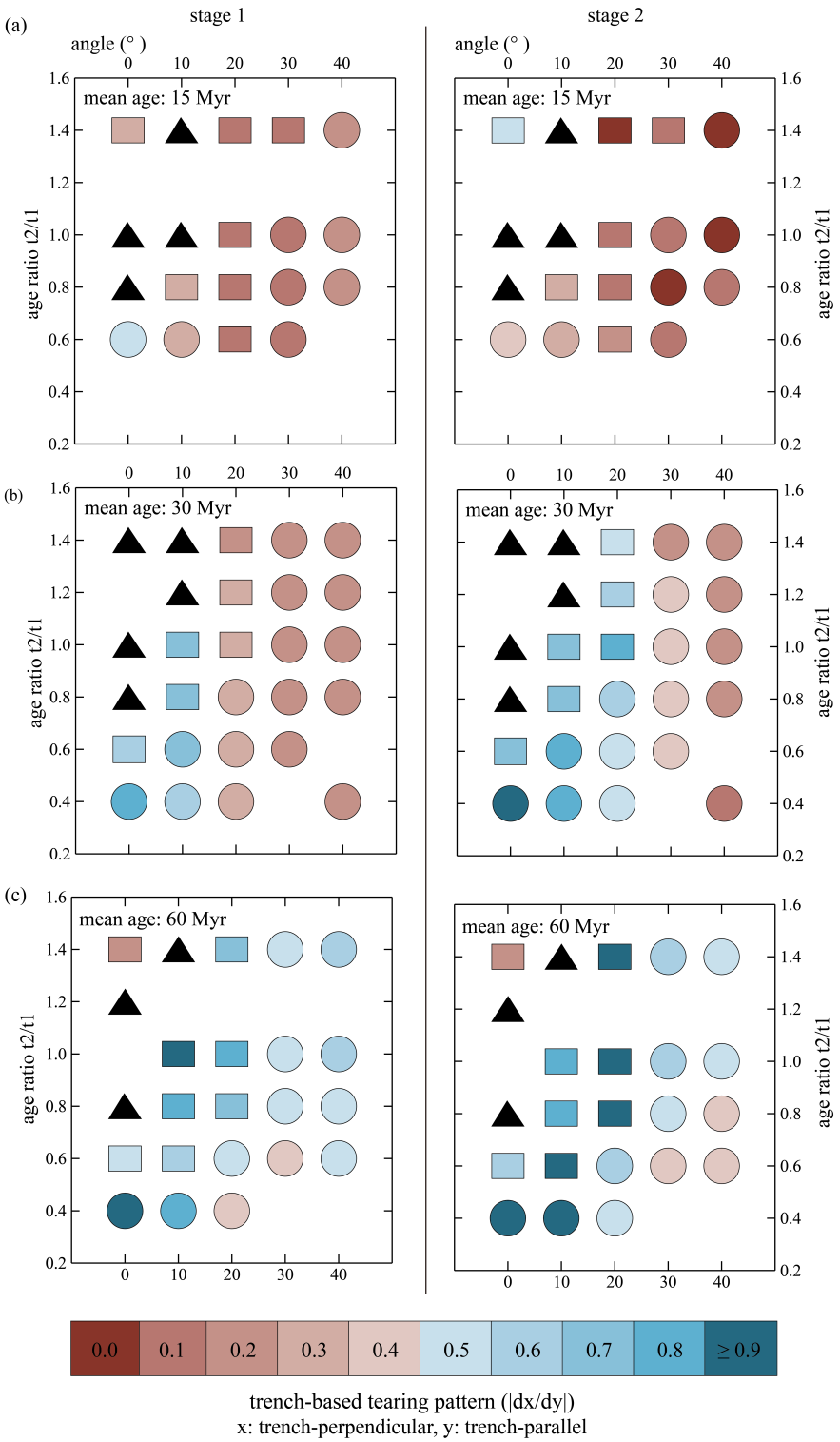

Posted on 25 May 2023 — The copyright holder is the author/funder. All rights reserved. No reuse without permission. — https://doi.org/10.22541/essoar.168500350.09716718/v1 — This a preprint and has not been peer reviewed. Data may be preliminary.

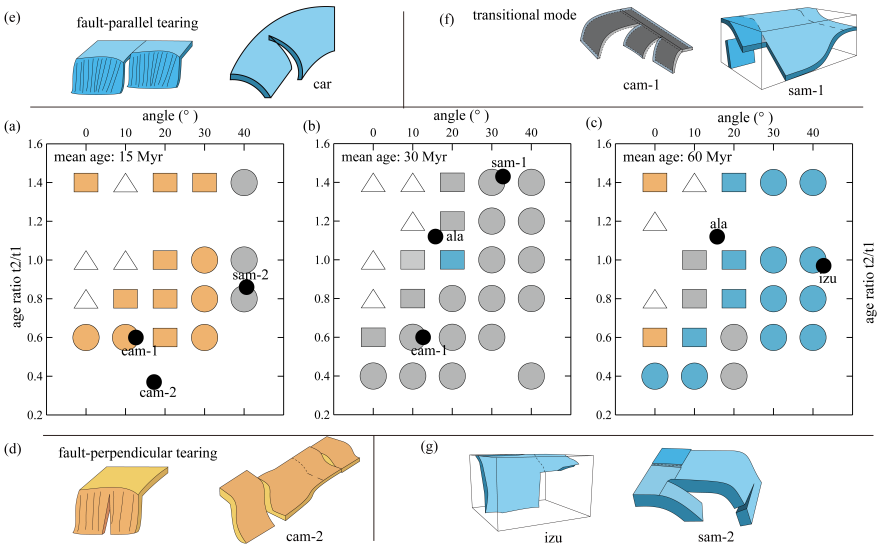

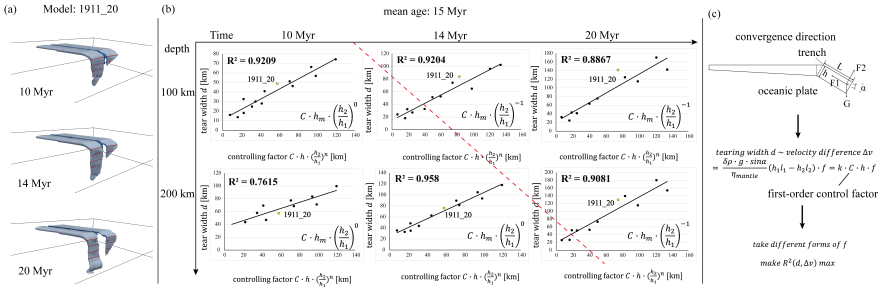

Dynamics of oceanic slab tearing during transform-fault horizontally-oblique subduction: Insights from 3D numerical modeling

Jie Xin[1], Huai Zhang[1,4,5,*], Felipe Orellana-Rovirosa[2], Zhong-Hai Li[1], Liang Liu[3], Yi-Gang Xu[3], Zhen Zhang[1], Yaolin Shi[1]

[1]Key Laboratory of Computational Geodynamics, College of Earth and Planetary Sciences, University of Chinese Academy of Sciences, Beijing 100049, China

[2]Department of Ocean Science and Engineering, Southern University of Science and Technology, Shenzhen 518055, China

[3]State Key Laboratory of Isotope Geochemistry, Guangzhou Institute of Geochemistry, Chinese Academy of Sciences, Guangzhou 510640, China

[4]Beijing Yanshan Earth Critical Zone National Research Station, University of Chinese Academy of Sciences, Beijing 101408, China

[5]Southern Marine Science and Engineering Guangdong Laboratory (Zhuhai), Guangdong Zhuhai 519080, China

Key Points:

- 3-D numerical models are conducted to study the vertical tearing mechanism of the transform-faulted oceanic slabs during oblique subduction.
- The horizontal obliqueness and slab transform age difference play dominant roles in determining the style of vertical slab tearing.
- Correlations between slabs' computed tearing width and scaling-theory forms of subduction-velocity difference, are useful and strong.

Abstract

Oceanic-plates vertical tearing is seismically-identified in the present-day Earth. This type of plate tearing is frequently reported in horizontally-oblique subduction zones where transform-faulted oceanic plates are subducting (or subducted). However, the mechanisms behind vertical slab tearing are still poorly understood, thus we utilize 3D time-dependent Stokes' flow thermo-mechanical models to further study this problem. We find that (i) the age offset of transform fault and (ii) the horizontal obliqueness of subduction fundamentally control the tearing behavior of two generic, materially-homogeneous oceanic slabs separated by a low-viscosity zone. The overriding-continental plate bends one slab first, which combined with the age-thickness difference between slabs, causes the differential sinking of them. Based on the modeling results, well-developed slabs vertical tearing would happen when the oblique angle of subduction is ⩾30° or the age ratio of the secondly-bent to firstly-bent slab being ~<0.6. Quantifying the horizontal distance-vector between sinking slabs, we find that subduction at medium-low horizontal-obliqueness angles (≤30°) of young lithosphere (slabs-average ~15 Myr) tends to produce fault-perpendicular tearing. Contrastingly, old-age slabs (average ≥ 30 Myr) with medium-large obliqueness angles (~>20°) tend to produce fault-parallel tearing, related to differential slab-hinge retreat or rollback. Correlations between slabs' (i) computed tearing horizontal-width and (ii) scaling-theory forms of their subduction-velocity differences, are reasonable (0.76-0.97). Our numerically-predicted scenarios are reasonably consistent with plate-tear imaging results from at least 4 natural subduction zones. Our modeling also suggests that continual along-trench variation in subduction dip angle may be related to a special case of oblique subduction.

Keywords: Oceanic slabs vertical tearing, horizontally-oblique subduction, transform-fault offset, 3D numerical models, Stokes' flow.

Plain Language Summary

Oceanic tectonic plates can tear-off through time as they plunge and sink into the Earth's mantle and are especially favored when plates have preexisting fault-weak zones. Two primary conditions promote oceanic tectonic slabs' tearing: (1) Obliqueness of a plate's horizontal velocity with respect to the overriding-plate coastline and trench, as the latter will enforce bending of one side of the slab first causing differences in deformation; (2) Differences in slab-age between two sides of a displaced fault-zone that created an offset in plate age and thickness. To understand these processes, we present 3D numerical models that simulate tectonic evolution and deformations, and we compare model results with analytical studies as well as with natural observations from seismic imaging. Age differences across fault-zones combined with subduction horizontal obliqueness control the generation and development of vertical tearing. Furthermore, two geometrical patterns of vertical tearing are largely consistent with observations. Our findings suggest that along-trench changes in the steep angle between the slab and surface (dip angle) may be related to the early stages of oblique subduction. Observing the age contrast across faults and the horizontal obliqueness of plates' motion allows predictions of the tearing pattern, evolution, and local mantle flow.

1. Introduction

Oceanic lithosphere tearing (or break-off) is a general phenomenon on present-day Earth. When occurring, the resulting slab window allows hot mantle materials to pass through, resulting in anomalous thermal and chemical conditions in convergent-margin environments (Gianni & Luján, 2021; Thorkelson, 1996). If slab tearing occurs at shallow depths (Freeburn et al., 2017; Király et al., 2020), the asthenospheric upwelling causes significant geological and geophysical responses, including complex mantle flow in subduction zones (Bolton et al., 2022; R. Govers & Wortel, 2005; Rosenbaum et al., 2008), anomalous thermal and mechanical structures of the overlying plate (Georgieva et al., 2016; Guillaume et al., 2010; Jolivet et al., 2015; Roche et al., 2018), as well as active arc and back-arc magmatism (Gianni & Luján, 2021; K. Liu et al., 2020; Xu et al., 2020).

Plate tearing can be categorized into horizontal and vertical tearing patterns (Rosenbaum et al., 2008). The horizontal tearing normally occurs along a sub-horizontal plane, in which the lower segment of the slab detaches from the upper and then sinks into the mantle. In this case, the negative buoyancy of the subducted slab contributes to the slab break-off (tearing) process (Duretz et al., 2011; Gerya, 2022; Hildebrand et al., 2018; Kufner et al., 2017; L. Liu et al., 2021). On the other hand, it is generally considered difficult for a coherent subducting slab to tear along sub-vertical planes perpendicular to the trench (Cui & Li, 2022) due to the lack of major force gradients in the along-strike direction. However, according to studies of seismic tomography, vertical slab tearing (sub-vertically-oriented anelastic (brittle-visco-plastic) tears, that may be propagating in the subducted-subducting portions of oceanic slabs) seems to have developed in many subduction zones of present-day Earth (Figure 1), including the Mariana's subduction zone (M. S. Miller et al., 2004; Meghan S. Miller et al., 2006), the Calabria subduction zone (Jolivet et al., 2021; Suckale et al., 2009), the Aegean and Anatolia regions (Rob Govers & Fichtner, 2016; Jolivet et al., 2015), the Central America subduction zone (Carciumaru et al., 2020; Dougherty & Clayton, 2014; Stubailo et al., 2012; Thorkelson, 1996), the South American subduction zone (Pesicek et al., 2012; Rosenbaum et al., 2008; Vargas & Mann, 2013), the Caribbean

subduction zone (Meighan et al., 2013), and the Kamchatka subduction zone (Levin et al., 2002).

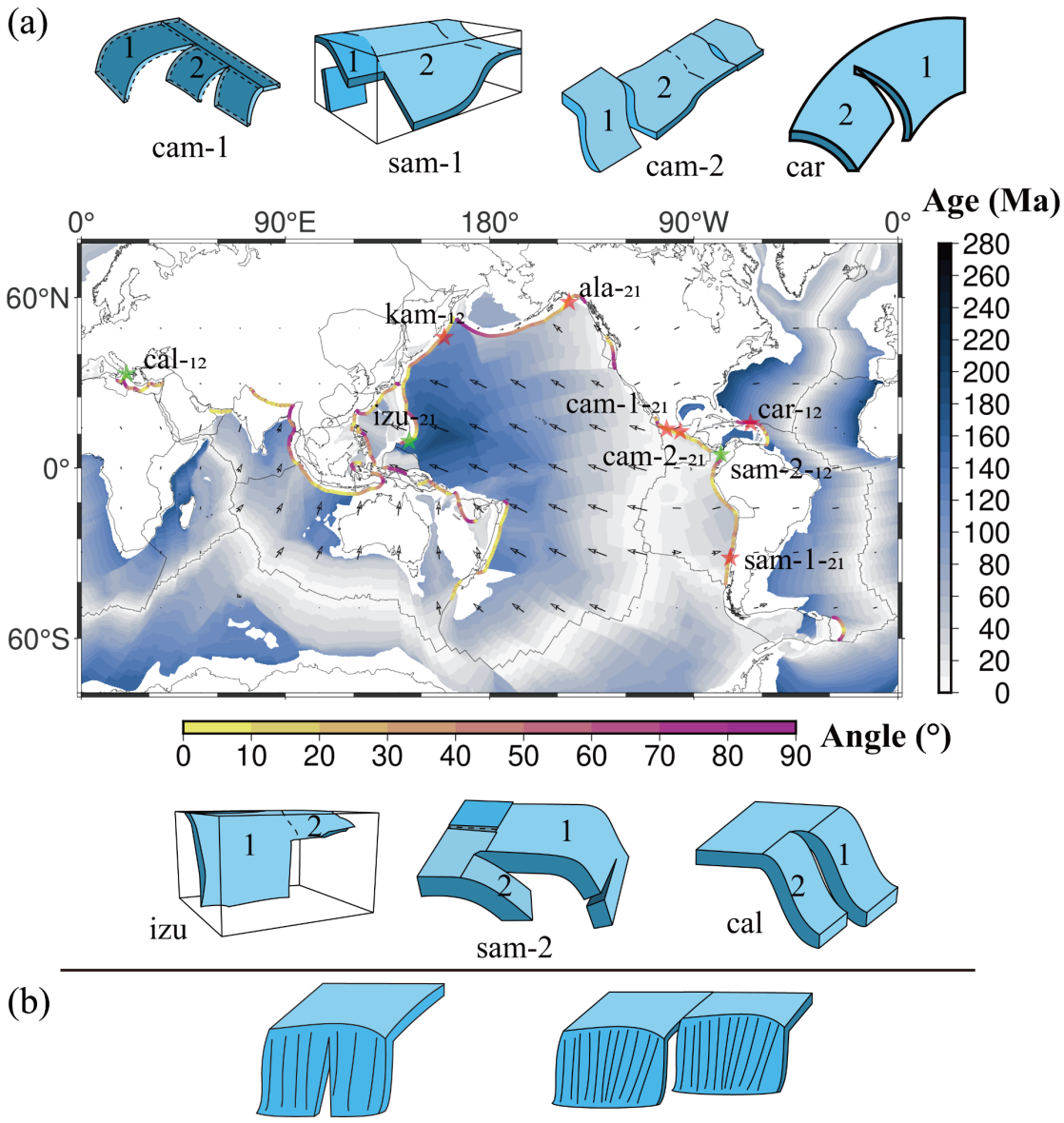

Figure 1. Global distribution of vertical plate tearing in the present-day oceanic subduction zones. (a) The stars on the map and the cartoons above or below show each case's position and deep structure. Red stars represent tearing involving transform-fault subduction, and green stars involve other factors (e.g., ocean-continent transform zone, ridge subduction). The cartoons are shown for '**ala**' and '**kam**' due to the lack of relevant data. The references for these subduction zones are: Central America (**cam-2**): Carciumaru et al., 2020; Dougherty and Clayton, 2014; Kamchatka (**kam**): Levin et al., 2002; Caribbean (**car**): Meighan et al., 2013; Izu-Bonin (**izu**): Miller et al., 2006; South America (**sam-1**): Pesicek et al., 2012; Central America (**cam-1**): Stubailo et al., 2012; Calabria (**cal**): Suckale et al., 2009; South America (**sam-2**): Vargas and Mann, 2013; Alaska (**ala**): Yang and Gao, 2020. The identifications of slab-1 and slab-2 are defined as follows: slab-1 is the slab that would arrive and contact the

trench earlier, whereas slab-2 would do it later. The vertical color bar represents the age of the oceanic lithosphere, and the horizontal color bar is the magnitude of the angle between horizontal plate velocity and the direction perpendicular to the trench. The angle sign is coded-indicated by the numbers after the second hyphen, the first number corresponds to the left-side slab when standing above the subduction zone and looking toward the continent, and the second indicates the right-side slab. The arrows indicate the plate velocity in the hot spot reference frame (Becker et al., 2015). The data on the subduction zone, seafloor age, and color bar are referred to (Hayes et al., 2018), (Müller et al., 2008), and (Crameri, 2021), respectively. (b) Cartoons illustrate the two typical slab vertical tearing patterns (Rosenbaum et al., 2008).

Slab quasi-vertically-oriented tears (and frequently sub-vertically propagating) within the mantle generally require along-strike physical variations (such as gradients in morphology, forces, material properties, etc.), with several mechanisms being proposed: non-uniform rollback due to lateral temperature and age differences in subducting plates or step faulting at the edges of active margins (Burkett & Billen, 2010; R. Govers & Wortel, 2005), opposite rotation of slab segments (Gianni et al., 2019), oceanic/continental plate transition along-trench (Li et al., 2013; Magni et al., 2014; Pusok et al., 2018), subduction of spreading ridges (Burkett & Billen, 2010), and perhaps finally, variable orientations of passive margins (Fernández-García et al., 2019). Therefore, various factors can affect the specific subduction mode, with slabs undergoing translation, rotation, and deformation during the sinking, with tearing being an extreme case of slab deformation involving topological changes. Due to this complexity, in this study, we would narrow our focus to the scenarios where the oblique subduction of transform-faulted slabs develops.

As proposed in previous studies, due to the contrasting seafloor ages (and mechanical properties) across a transform fault, the vertical tearing of transform-faulted oceanic plate likely happens (Burkett & Billen, 2010). In addition, we consider the horizontal obliqueness of the subduction direction with respect to the trench as playing a key role in combination with the transform-fault age contrasts.

In this study, by systematically conducting 3D time-dependent numerical modeling to investigate the effects of the two factors for vertical oceanic-plate tearing, we will summarize the key conditions for different observed patterns for vertical slab (Figure 1

and Table 1) tearing and use a scaling method to reveal the controlling variables behind them.

We hope this work will improve our understanding of these “abstract” systems, but also our understanding of real-Earth systems that comprise geological/physical ingredients of this kind; and to help us for example, when attempting to infer the pre-subduction obliqueness angle of a subducted plate that may lack hotspot-track constraints, and also to improve the accuracy of plate reconstructions.

Table 1. Parameters of the natural subduction zones with slab tearing [a].

Symbol (subduction zone)	Name of the fracture zone [b]	Oblique convergence angle	Age of Slab-1 (t_1, Ma)	Age of Slab-2 (t_2, Ma)
cam-1 (Central America)	Tehuantepec	12.6°	23.6	14.3
cam-2 (Central America)	Orozco	17.2°	12.7	4.7
sam-1 (South America)	Mocha	32.8°	24.6	35.3
sam-2 (South America)	——[b]	40.6°	12.7	10.9
Izu (Izu-Bonin)	——[b]	42.7°	156.0	150.8
cal (Calabria)	Kephalonia [b]	22.9°	247.2	245.3
car (Caribbean)	——	70.2°	88.7	115.4
ala (Alaska)	Between the Pacific plate and the Yakutat plate	15.8°	34.0	38.2
kam (Kamchatka-Kuril)	——	22.7°	111.9	110.2

[a] The slabs convergence angle and lithospheric ages use the averaged values within 300 km of both sides of the corresponding symbol sites on the map (Figure 1). [b] Other types of subduction tectonic environments are distinguished by green stars (Figure 1), e.g., ocean-continent transform zone, ridge subduction.

2. Model setup

We use the finite-element software ASPECT (version 2.3.0) to solve the incompressible Stokes' viscous flow equations (1-2) coupled with thermal advection-diffusion equation (3) velocity $\boldsymbol{u}$, pressure p, temperature T (Bangerth et al., 2021; Glerum et al., 2018). Equation (4) describes the evolution of additional (compositional) fields transported along with the velocity field $\boldsymbol{u}$, without diffusion. For the Stokes' flow equation, we employ the Taylor-Hood spatial element.

$$-\nabla \cdot \left[2\eta\left(\varepsilon(\boldsymbol{u})\right)\right] + \nabla p = \rho \boldsymbol{g} \tag{1}$$

$$\nabla \cdot \boldsymbol{u} = 0 \tag{2}$$

$$\rho C_p \left(\frac{\partial T}{\partial t} + \boldsymbol{u} \cdot \nabla T\right) - \nabla \cdot k \nabla T = 0 \tag{3}$$

$$\frac{\partial c_i}{\partial t} + \boldsymbol{u} \cdot \nabla c_i = 0 \tag{4}$$

where c_i is the i-th compositional field that defines and tracks subsets of distinct chemical compositions and properties, $\varepsilon(u) = \frac{1}{2}(\nabla u + \nabla u^T)$ is the linear strain rate, η, ρ, C_p and k are the fluid's shear viscosity, mass-density, specific isobaric heat capacity and thermal conductivity, respectively; and **g** is the gravitational acceleration.

A 3D Cartesian model box with spatial dimensions of 2500 km×3000 km×660 km is used. Figure 2 shows the initial model configuration demonstrated in composition, including a partially-subducted oceanic lithosphere: two slabs separated by a weak transform fault-zone in the middle, a continental lithosphere as the overriding plate, and two side plates (Figure 2a). Although these denominations may conflict with previous studies, this will be, for the sake of cleanliness, our formal language-terminology from this point onward in this article: our model has one single oceanic plate or lithosphere, separated in two slabs by the transform-fault zone.

The width of the weak transform fault-zone is 30 km, and its thickness is consistent with that of the thicker lithosphere on both sides. A low-viscosity oceanic crust defines the uppermost part of the subducting lithosphere (slabs), and act as a weak contact zone with the overriding continental plate. The initial vertical dip angle of the subducting slabs is fixed at 30°. The subducting oceanic plate is decoupled from the side plates by

applying two side faults, as shown in Figure 2b. In contrast to the central plate, which is 10 km from the left boundary and undergoes free subduction, no subducting slab is prescribed for the side plates (Figure 2d).

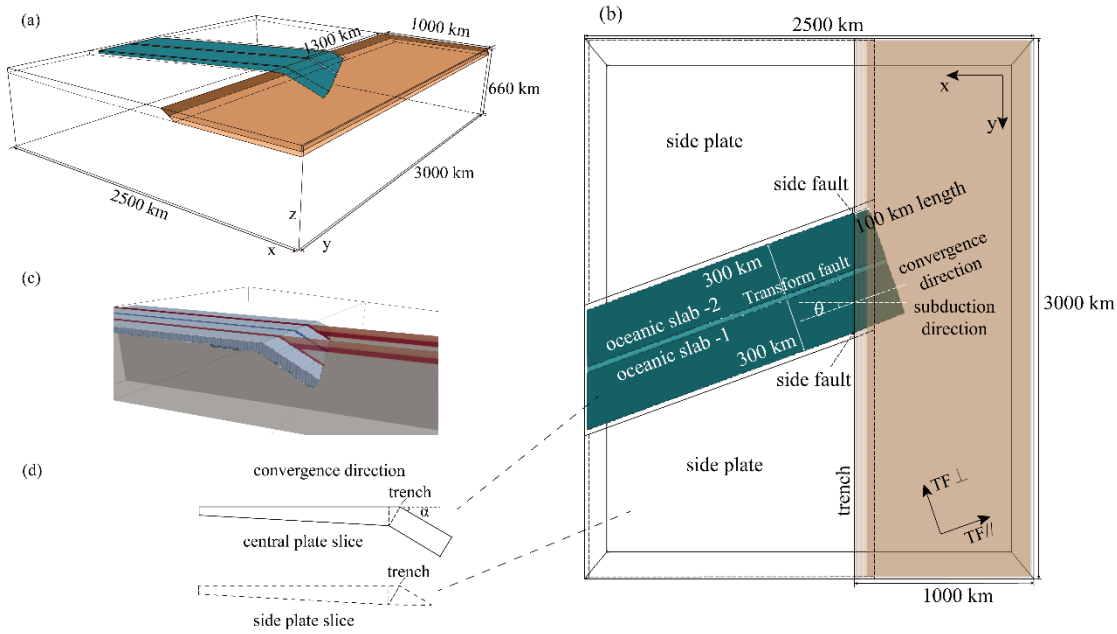

Figure 2. Initial condition model setup. (a) 3D oblique view of the model structure with the subducting (cyan) and overriding (brown) plates. (b) View from above. The oceanic lithosphere's weak central region (transform fault zone) is 30 km wide and separates the plate in two distinct slabs. The two fundamental coordinate systems are shown, with trench -perpendicular (X) and -parallel (Y) axes, and transform-fault -parallel (TF//) and -perpendicular (TF ⊥) axes. (c) The initial composition of the oceanic lithosphere (blue) and vertical slices of density (red). (d) The vertical cross-sections on the lateral edges of subducting lithosphere and adjacent plate slice lithosphere. The initial dip angle of the subducting slab is α =30° (vertical angle, same value for all the models). The horizontal angle θ parameterizes the horizontally-oblique subduction. The length of the shortest subducted slab segment is 100 km (in slab-2) and increases gradually to the other side (slab-1).

The half-space cooling model is used to calculate the oceanic plate's initial-condition thermal-age thickness as $h \approx 2.32\sqrt{\kappa t}$ ($h_{max} = 100km$) (Turcotte & Schubert, 2002), where k is thermal diffusivity, and t is seafloor age. In this sense, the thickness ratio between slabs 1 and 2, *i.e.*, h_1/h_2, is dynamically similar to the square root of the ratio of lithospheric ages $\sqrt{t_1/t_2}$. The ocean plate's initial (unsubducted) maximum thickness is limited to 100 km, consistent with thermo-rheological observations (Schubert et al.,

2001). The model-box's top and bottom boundary temperatures are fixed at 293 °K and 1775 °K (calculated using the mantle adiabatic thermal gradient), respectively.

Our representation assumes the oceanic-plate as a numerical compositional field, with two distinct variable-thickness domains, layers or slabs whose initial-condition upper and lower surfaces (and thicknesses) are defined by two isothermal surfaces of the half-space cooling model (whose maximum depth depends on the horizontal transform-fault-parallel coordinate as previously indicated). The slabs' density and viscosity are assumed to remain constant (this is a major simplification: these model-variables do not depend on pressure, temperature, or strain rate) with well-established values (Table 2), thermal expansion coefficient is assumed null and thermal conductivity is fixed. This simplification is only a first-order approximation which allows faster computations. In the mantle domain, an adiabatic temperature profile is applied as initial condition.

Our model slabs can change their thickness as they evolve in time, but solely by virtue of divergence-free flow advection and deformation (they can thicken/thin if their perpendicular area decreases/increases), a dynamical consequence of 3D-time-dependent velocity field. The thermal field spatio-temporally evolves and its coldest regions fairly approximate the compositional slabs (especially at early times given slow-enough thermal diffusion), and this provides additional supporting information on the system (later on used in two of our figures).

The velocity field boundary conditions (at all times) are of tangential flow boundary, i.e. free-slip (zero shear stress) and no-flow-through (zero normal velocity), on all the model-box surface boundaries except for that at the bottom: the lower boundary is fixed (3D zero velocity vector) and intended to simulate the effect of the 660 km phase-transition interface.

Finally, the computational grid is adaptively refined five times until its smaller cell reaches a minimum size of 6.51 km×6.25 km×6.88 km, and the coarsest cell size is 8 times larger. The maximum number of cells is ~3×10^5 and the number of unknowns is ~8×10^7. Usually, it takes 24 to 48 hours for each model, running with 220 computing

cores, to simulate a geological time of about 30 Myr.

Table 2. Material properties of the numerical models [a].

Compositional units	Density($kg \cdot m^{-3}$) [b]	Viscosity(Pa·s)
Underlying upper mantle	3300	1.4×10^{20}
Oceanic crust	3390	2.8×10^{20}
Oceanic lithospheric mantle	3390	1.4×10^{23}
Continental crust	2800	1.4×10^{24}
Continental lithospheric mantle	3390	1.4×10^{23}
Transform-fault zone	3390	7.0×10^{20}
Side faults	3390	7.0×10^{20}
Crust of side plates	3350	2.8×10^{20}
Lithospheric mantle of side plates	3390	1.4×10^{23}

[a] Other parameter values: Reference temperature = 293 °K; heat capacity = 1250 J/kg/°K; thermal conductivity = 4 W/m/°K; thermal expansion coefficient = 0.

[b] The value of density implicitly includes the thermal-effect dependence.

3. Results

A total of 69 experiments/simulations are conducted with different relevant combinations of oceanic lithosphere's (i) horizontal-obliqueness angles and (ii) slabs age offset. To quantify the size of the tear width, we visualized and post-processed the output data in ParaView, specifically by selecting horizontal slices of the oceanic lithosphere at various times and depths and measuring the horizontal vector distance between the two slabs (Figure 3).

3.1. Tested conditions for vertical slab tearing

In our simulations, the slabs' tearing process can be separated, before and after, by the event of slab 1 reaching the 660 km depth (as mapped by the oceanic-lithosphere compositional field (in Aspect software) value >0.5 within 15 km from such depth). In particular, for our reference model (t_1=33 Myr, t_2=27 Myr, θ=20°; abbreviated as

3327_20), we show snapshots of its evolution in Figure 3a by isolating temperatures ≤1380 °K, so the sinking slabs appear bounded by isothermal surfaces (with the hotter ambient mantle made invisible).

Using ASPECT-software compositional fields, for all the simulations, we isolate the slabs from the embedding ambient mantle (as for the reference simulation in Figure 3b), and then we measure the tear horizontal-widths at different depths in both time-stages (as in Figure 3b).

As can be seen from the white contour lines (depths: 100-200-300-400 km) in Figure 3a, vertical tearing can occur at deep locations (>200 km depth). As the subduction progresses, the finite-width tear gradually (after 12 Myr) expands and vertically-propagates to the shallow part (~100 km). After slab 1's tip arrives at the box bottom, its sinking velocity decreases, contributing to the increase in tearing width (Figure 3) at intermediate depths. After identifying the 660 km-depth contact event of slab 1, we select two sampling times: 2 Myr before and 2 Myr after the event. At each one of those times, we take the maximum value of tearing width d_{max} over the different depths for the subsequent determination of the tearing conditions (as in Figure 3b). Figure 4 displays the tearing judgments/decision array of the full set of numerical experiments.

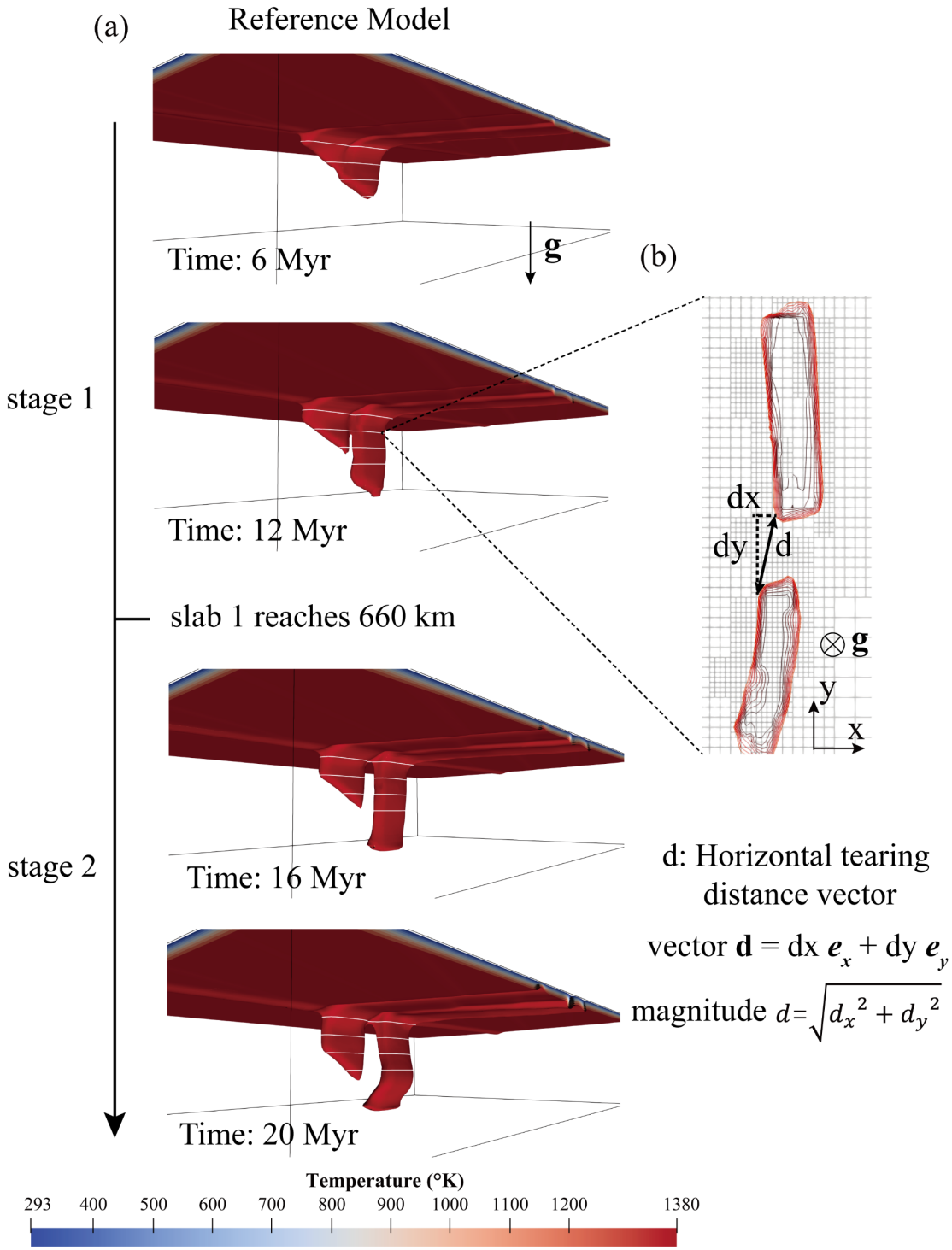

Figure 3. (a) Oblique view: Reference model evolution shown by isolating temperatures ≤1380 °K (so the slabs are visible approximately as an isothermal surface, and at shallow depths a thermal gradient is visible). Model parameters: oceanic-lithosphere slab ages t_1 = 33 Ma, t_2 = 27 Ma; horizontal obliqueness θ=20°. **(b) View from above**: Definition and quantification of slabs tearing at different depths (100-200-300-400 km), with the variable "d" being the time-dependent horizontal vector distance (of magnitude 'width') of slabs' tearing window. The vector-components ratio "dx/dy" and the oblique-convergence angle θ are used to characterize

the slabs' tearing patterns as explained in subsection 3.2 and 4.3.

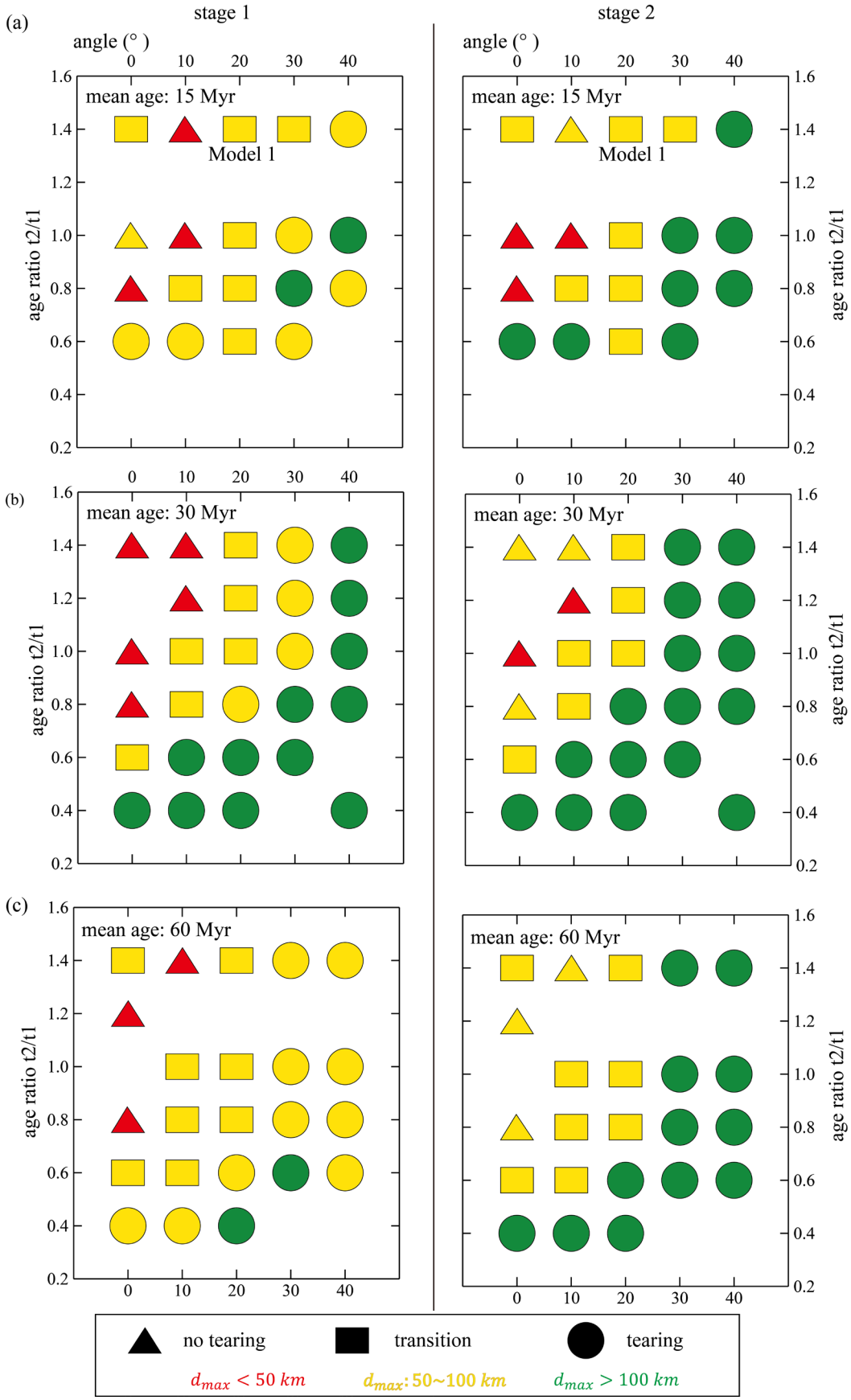

Figure 4. Check-box diagrams for the models' tested conditions. *Angle* means the horizontal obliqueness angle in the systems. The arithmetic-mean lithospheric age of slabs 1 and 2, $((t_1+t_2)/2)$, is 15 Myr (a), 30 Myr (b), and 60 Myr (c), respectively, defining the rows of the array plot. A slab reaching the 660 km-depth event defines the columns of the array plot: stage 1 (before) and stage 2 (after). The category of slab-tearing discrimination: Colors indicate the geometric state of slab tearing at each particular time-stage (at 1 (left) and at 2 (right)), as Red: maximum tearing width d_{max}<50 km, yellow: d_{max}: 50-100 km, green: d_{max}>100 km. Symbol shapes indicate the situation integrated through both time-stages: If at any of the two stages the tearing width is <50 km, the model is classified as "no tearing" (triangles), and if >100 km the model is "tearing" (circles), while cases in between are transitional modes (rectangles). These symbol shapes are necessary for the subsequent figures of this article.

Each one of the three major rows on the diagram in Figure 4 summarizes the results of simulations with the same arithmetic-mean age $\frac{t_1+t_2}{2}$ of the plates separated by the transform fault. To classify each simulation, we use relative age ratio rather than age difference as a way to avoid discussing parameters that deviate far from nature, i.e., $t_1 - t_2 = t_1\left(1 - \frac{t_2}{t_1}\right)$, For the same age ratio, a younger mean age suggests a smaller absolute age difference. For any given mean age, significant oceanic-plate tearing is favored by a large obliqueness angle and/or by older slab-1 age relative to slab-2. Most models fail to tear without horizontal obliqueness of the subduction (angle θ=0°) except for medium-aged plates with substantial age differences.

In particular, due to thin slabs, Model 1 (1318_20) in the low mean absolute age group (15 Myr) exhibits lateral break-off, increasing tearing width. At 60 Myr-30° and 60 Myr-40°, the tearing width does not increase beyond a certain extent before slab 1 reaches the bottom, so its tearing width is small during stage 1. In cross-sectional comparison, we find that the tearing area is larger in stage 2 than in stage 1, especially the 60 Myr group changes from yellow to green color code. In the vertical comparison, we found that the tear area increases and then decreases with increasing mean age, which will be further analyzed in the subsequent discussion.

In conclusion, our simulations suggest that for any values of obliquity, the subducting plates tear for age ratios less than 0.6, meaning that an older-thicker slab-1 entering the

trench first, then sinking first and faster, progressively tears off from slab-2. Furthermore, regardless of the transform-fault age ratios, all the plates tear at horizontal obliqueness greater than 30°. This latter behavior is certainly an effect of the contact surface forces exerted by the overriding (continental) plate on forcing the bending of an obliquely-subducting slab-1 first and then later on slab-2. The larger the horizontal-obliqueness angle, the larger the difference between the slabs' subducted areas (especially during the early stages of the process) and the more intensive and extensive the strain of the weak fault zone between the slabs. Finally, as crucial reference cases, we must note the case when the horizontal-obliqueness $\theta = 0°$ and simultaneously slabs' age-ratio=1, meaning two identical slabs separated by a weak zone and converging perpendicular to the trench. Those simulations show tearing displacements that when existing and being measurable at all, have values $d_{max} < 50$-75 km, meaning that tearing almost does not occur (symbolized as triangles, in red and yellow in Figure 4).

3.2. Patterns of vertical slab tearing

In this study, we consider the horizontal distance vector of tearing displacement between the slabs: $d = d_x\,\mathbf{e_x} + d_y\,\mathbf{e_y}$, measured at depth in their vertical portions inside the ambient mantle.

The maximum tearing width (displacement magnitude) over different depths of the subducting plate (depths: 100-200-300-400 km) is used to indicate whether tearing occurs (summarized in Figure 4). In addition, the ratio of the tearing vector components in the transform-fault-based system (given an obliqueness angle θ, see Figures 2 and 3 for definitions) is employed to characterize the tearing patterns. We project the tearing distance-vector components d_x and d_y (referred to trench perpendicular-and-parallel coordinates, respectively) onto the initial horizontally-oblique-convergence direction and its normal direction (i.e., onto the coordinate system defined by the transform-fault direction and its perpendicular), respectively, to obtain the fault-parallel $d_{fault//}$ and fault-perpendicular- $d_{fault\perp}$ tearing components. We obtain:

$$\frac{d_{fault//}}{d_{fault\perp}} = \frac{d_x cos\theta + d_y sin\theta}{-d_x sin\theta + d_y cos\theta} = \frac{\frac{d_x}{d_y} + tan\theta}{1 - \frac{d_x}{d_y} tan\theta} \quad (5).$$

When $|\frac{d_{fault//}}{d_{fault\perp}}|$ >1.3, the tearing pattern is defined as fault-parallel tearing (related to slabs' differential hinge retreat or rollback) (Figure 5). In contrast with $|\frac{d_{fault//}}{d_{fault\perp}}|$ <0.7, the pattern is defined as fault-perpendicular tearing, in which the along-slabs-hinge-axis tearing dominates. A transitional-intermediate mode is defined as between (0.7-1.3).

Specifically, at each desired time, we take the average (arithmetic mean) value of the aforementioned ratio at the different depths and consider that average for the subsequent determination of the tearing pattern (Figure 3b and Figure 5).

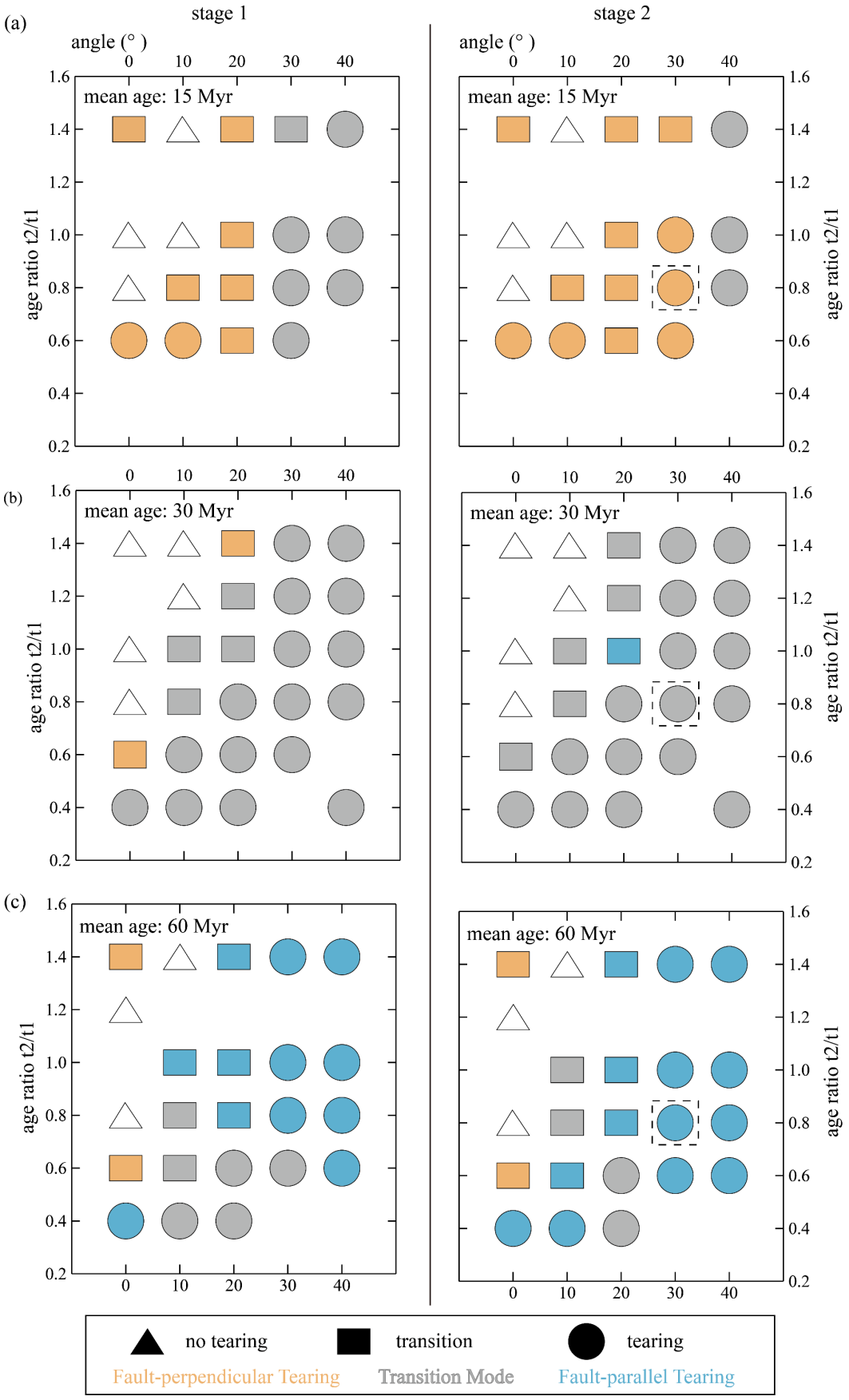

Figure 5. Check-box diagrams for the tearing patterns on time-stages 1 (left) and 2 (right). *Angle* means the horizontal-obliqueness angle. The arithmetic-mean lithospheric age of slabs 1

and 2, ($(t_1+t_2)/2$), is 15 Myr (a), 30 Myr (b), and 60 Myr (c), respectively. The category of slabs tearing pattern, depending on the ratio "$|d_{fault//}/d_{fault\perp}|$". Orange: If $|d_{fault//}/d_{fault\perp}| < 0.7$, the pattern is defined as fault-perpendicular tearing. Blue: In contrast with $|d_{fault//}/d_{fault\perp}| >$ 1.3, the pattern is defined as fault-parallel tearing. Gray: A transition-hybrid mode is 0.7-1.3. The definition of symbol shapes is the same as in Figure 4. Each age-group stage-2 simulations enclosed by dashed-line squares are used in figures 6 and 7.

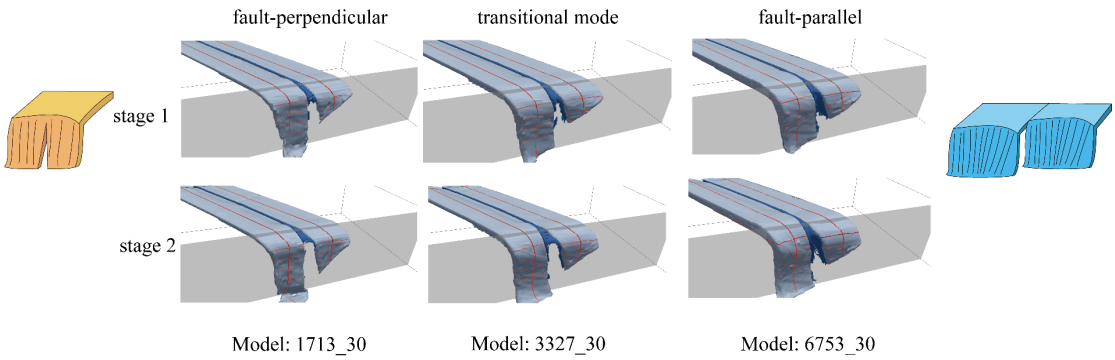

Figure 6. Example models illustrating the three different slab tearing patterns (determined by the ratio of tearing horizontal-displacement components). End-member cartoons are provided for illustration. These three particular example simulations (signaled by dashed squares in Figures 5a,b,c), while differing only in their slabs' mean age, all have age ratios of about ~0.8 and obliqueness-angle θ=30°.

Plate-motion horizontal obliquity influences the fault-parallel and also the transverse/fault-perpendicular direction of forces and resulting tearing displacements. However, it seems dominant only in young slabs, such as the region less than 40° in the 15 Myr group in Figure 5. On the other hand, large absolute age differences generally result in large sinking velocity differences that project in the convergence direction, such as the region θ ~> 20° and t_2/t_1 ~< 0.6 (bottom left corner) in the 60 Myr group in Figure 5.

As shown by Figure 6, considering older slabs at the initial condition, with mean ages from 15 to 30 to 60 Myr, fault-perpendicular tearing patterns tend to disappear (occurring only in some cases), meaning that it is mostly a young-age tearing behavior. On the other hand, fault-parallel manifests commonly-extensively only for old slabs with a mean age of 60 Myr, with only one exception at a mean age of 30 Myr.

Figure 7 shows the evolution of the typical models of the two tearing patterns,

simulation 1713_30 for fault-perpendicular tearing and simulation 6753_30 for fault-parallel tearing. The larger mean age/thickness enhances the differential retreat of the two slabs in the convergence direction, causing the vertical tearing (while inside the mantle) pattern to be dominated by fault-parallel tearing (Figures 7 a,d). In fact, at old slab ages (such as 60 Myr), the same age ratios as in the other age groups are attained with larger absolute-age differences, and these latter ones imply larger absolute sinking-and-subduction velocity differences (see subsection 4.1). Therefore, old-age slabs tend to favor differential slabs' retreat and fault-parallel tearing (Figure 5). Additionally, the distance from the trench to the 90° slab-dip angle position, called the bending length l_b, varies between the two differentially-retreating slabs and with time evolution, and this will be further analyzed in the subsequent discussion section (Figures 7 b,c).

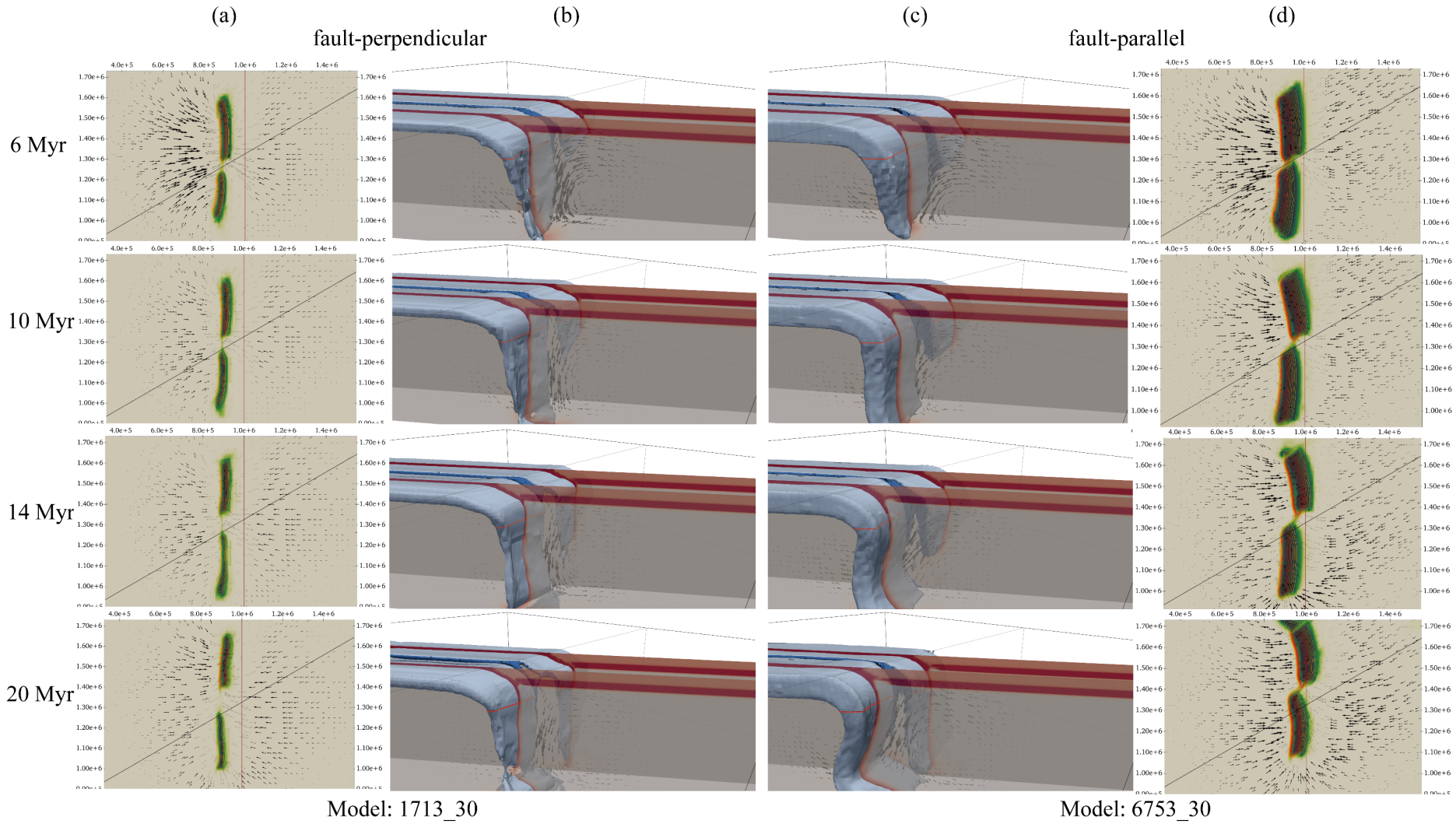
(a)
(b)
(c)
(d)
fault-perpendicular
fault-parallel
6 Myr
10 Myr
14 Myr
20 Myr
Model: 1713_30
Model: 6753_30

Figure 7. Evolution of the two case simulations that exemplify the two tearing patterns, singled out and indicated by dashed-line squares in Figure 5. Panels (a) and (d): View from above, thermal contour (yellow, the legend is the same as Figure 3) and viscosity (green) structure (Table 2) at 150 km depth. Small black arrows: ambient-mantle velocity vector field. Black oblique line: All-time slabs' prescribed horizontal convergence direction. The red line at fixed abscissa x: initial trench-line position. Panels (b) and (c): Oblique views, oceanic lithosphere (light blue) and transform fault (dark blue) as compositional fields. Additionally, 2D vertical slices of the overriding-continental plate's mass-density field are shown (plum-red colors and density values specified in Table 2).

4. Discussions

4.1. Analytical study of the slab tearing dynamics

In order to understand how the various controlling factors operate in our simulations and to enhance the verifiability of the model results, we utilize scaling similarity theory and available analytical-numerical studies.

We hypothesize that the horizontal width (d) of the tearing window is correlated to the difference in subduction velocity Δv between the two slabs separated by a transform fault. In a 2D subduction model, the oceanic slab is primarily subjected to (i) downward-buoyancy force $\delta\rho \cdot \mathbf{g} \cdot h \cdot l$ per unit length (with $\delta\rho$ density anomaly, $\mathbf{g}$ gravity acceleration, h the oceanic plate thickness, and l the slab tip-length along convergence direction), (ii) surrounding mantle resistance F_1 along the tangential direction of the slab $\eta_{\text{mantle}} \cdot v$ (where v is the plate speed, η_{mantle} the ambient-mantle viscosity), and (iii) unbending resistance F_2 perpendicular to the slab $\eta_{\text{plate}} \cdot v \cdot h^3/l_b^3$, where η_{plate} is the oceanic-plate viscosity, l_b is the bending length from the slab tip to the unbending place behind the hinge point (similar to the previous description of Figure 7 (Li & Ribe, 2012; Ribe, 2001) (Figure 8c). Then we take the one-slab tangential velocity $v_{2D} = \frac{\delta\rho \cdot g}{\eta_{mantle}} sin\alpha \cdot h \cdot l$ (in an idealized, terminal steady-state scenario where the slab, driven by the downward-buoyancy force, is 'gliding' inside the viscous mantle) along the slab subduction direction, as the major component that defines the tangential velocity difference Δv between slabs, yielding

$$\Delta v = \frac{\delta\rho \cdot g * sin\alpha}{\eta_{mantle}} (h_1 l_1 - h_2 l_2) \tag{6}$$

where α is the subduction dip (vertical) angle.

We assume that at the initial-condition of the subduction zone, in each one of the two slabs subducted portions (Figure 2), their thicknesses h_1 and h_2 remain constant. Then in this initial configuration and due to horizontal obliqueness, the initial slabs subducted-length l varies along the trench direction (y-direction) following $l(y, \theta) = \frac{c + y \cdot tan\theta}{cos\alpha}$, with $l_{min} = \frac{c}{cos\alpha}, l_{max} = \frac{c + 2w \cdot tan\theta}{cos\alpha}$, where c is fixed at 100 km (Figure 2b). Then we get $v_{3D} = \int_0^w v dy / \int_0^w 1 dy$, as the spatial-average velocity of the entire slab tip, with

w the horizontal span of the slab along the trench axis.

So, $v_{3D,1} = \frac{\delta\rho \cdot g sin\alpha}{\eta_{mantle}} \int_{w}^{2w} h_1 l(y) dy / \int_{w}^{2w} 1 dy$, $v_{3D,2} = \frac{\delta\rho \cdot g sin\alpha}{\eta_{mantle}} \int_{0}^{w} h_2 l(y) dy / \int_{0}^{w} 1 dy$.

Then, the simple-theoretical spatial-average velocity difference between slabs is obtained as $\Delta v_{3D} = v_{3D,1} - v_{3D,2} = \frac{\delta\rho \cdot g sin\alpha}{\eta_{mantle}} \cdot \frac{1}{2cos\alpha} \cdot [2c(h_1 - h_2) + (3h_1 - h_2) w \tan\theta] = \frac{\delta\rho \cdot g \cdot b \cdot tan\alpha}{2\eta_{mantle}} \cdot \left[2\frac{c}{b}\left(\frac{h_1}{h_2} - 1\right) + \left(3\frac{h_1}{h_2} - 1\right)\frac{sin\theta}{(cos\theta)^2}\right] \cdot h_2 \doteq k \cdot C \cdot h$, where $k = \frac{\delta\rho \cdot g \cdot b \cdot tan\alpha}{2\eta_{mantle}}$ (the unit is s^{-1}) is a functional factor composed of several dynamic parameters kept constant in each model simulation for simplicity, $b=w/cos\theta$ is the fixed slab width (Figure 2b), and the functional factor $C = 2\frac{c}{b}\left(\sqrt{\frac{t_1}{t_2}} - 1\right) + \left(3\sqrt{\frac{t_1}{t_2}} - 1\right)\frac{sin\theta}{(cos\theta)^2}$ considers the geometrical parameters reflecting the horizontally-oblique subduction effects, with the ratios of the square root of time representing ratios of thermal-age thicknesses, as $h \approx 2.32\sqrt{\kappa t}$ gives each oceanic slab thickness h versus its seafloor age t.

Following the logic of the unbending-resistance form $\eta_{plate} \cdot v \cdot h^3 / l_b^3$, in order to find the correlation between the model-output computed tearing distance d and the theoretical underlying controlling factors for the velocity difference Δv, we consider an additional multiplying variable factor f in the former simple-theoretical expression. f is a dimensionless parameter representing additional effects on Δv, such as unbending resistance along the slab-normal direction, differences between the two slabs' bending-sinking lengths and thicknesses, viscosity and width of the weak zone (transform fault), etc.; all of which depend on time as the sinking process evolves.

Therefore the original dimensional expression $k \cdot C \cdot h$ is expanded, upgraded and refined to $k \cdot C \cdot h \cdot f$. In this way, the dimensionless parameter f should accommodate for the aforementioned additional effects, and we use trial expressions of the form $f \approx \left(\frac{h_2}{h_1}\right)^n \frac{l_{b_1}}{l_{b_2}}$ to represent and account for them.

We used a set of fixed times (10 Myr, 14 Myr, 20 Myr) and depth range (100-400 km) to compare and correlate the tearing horizontal-width d with the spatial-average velocity difference Δv between slabs (brought by analytical scaling theory), and the results are shown in Figures 8-11. The figures are plotted for respective absolute mean ages of plates at {15, 30, 60} Myr and all of them together.

Upon constructing the correlations shown in Figures 8-11 and Table 3, we have removed four simulations from the data set, specifically simulations 1318_30, 1318_40, 1515_20, and 1515_30. This was done because these particular young "ultra-thin" slabs broke off during the subduction process, so we cannot precisely measure the tearing width in these models. Simulation 4317_40 can greatly increase the correlation coefficient in a way we distrust, so we also discarded it.

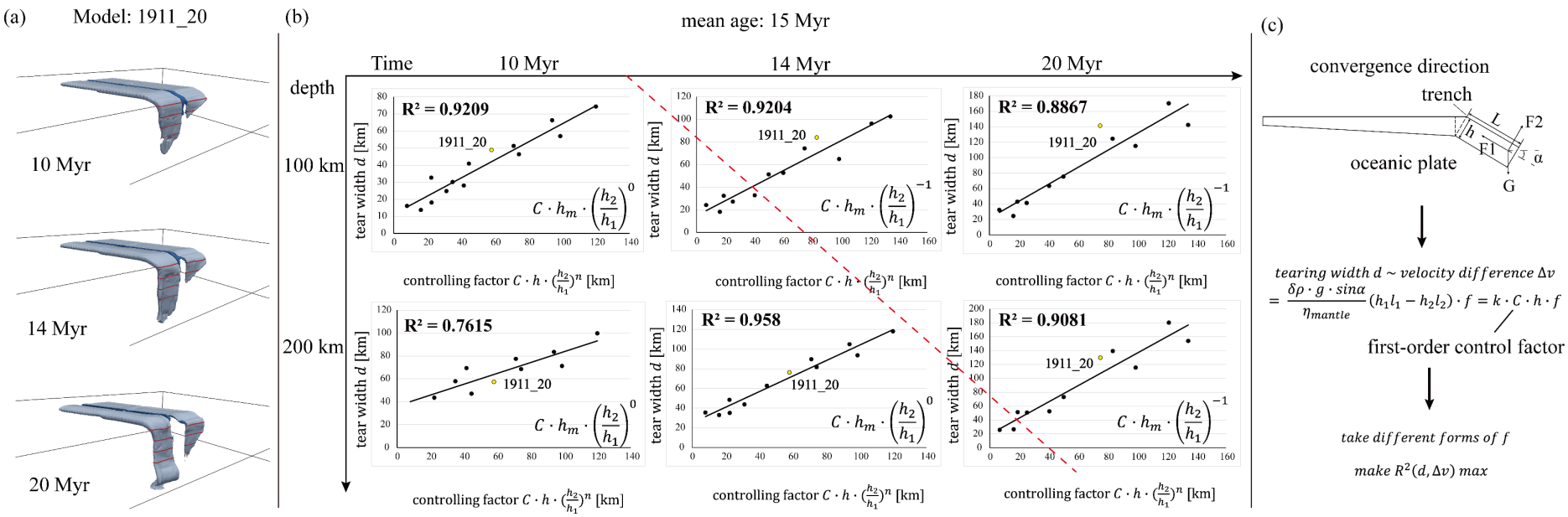

Figure 8. (a) Snapshots of model 1911_20 (slabs reference ages t_1=19 Myr, t_2=11 Myr, mean age 15 Myr, and subduction obliqueness θ=20°) at 10, 14, and 20 Myr of simulated time, showing the evolution of the oceanic lithosphere and the transform fault-zone tearing. The thin red curves on slabs are selected paths for geometry and tearing assessment computation (at 100, 200, 300, and 400 km depths). (b) The six different panels display trials on the functional forms of the slabs' velocity difference ($\Delta v/k = C{\cdot}h{\cdot}f$) depending on evolution time (large horizontal axis) and depth (large vertical axis), and their correlation with the slabs' horizontal tearing width (d). The correlation coefficient between tearing horizontal width (small vertical axis) and velocity difference controlling factor (small horizontal axis) is shown on each panel's top-left corner. The control parameters are consistent within each one of the areas delimited by the red dashed slash. (c) The major forces analysis on the tip part of a two-dimensional subducting slab with slab thickness h, initial slab length l, and subduction dip angle α. These plots illustrate the search for the maximum correlation coefficient between the slabs' tear horizontal width and the slabs-segments velocity difference by trying different functional forms of the latter.

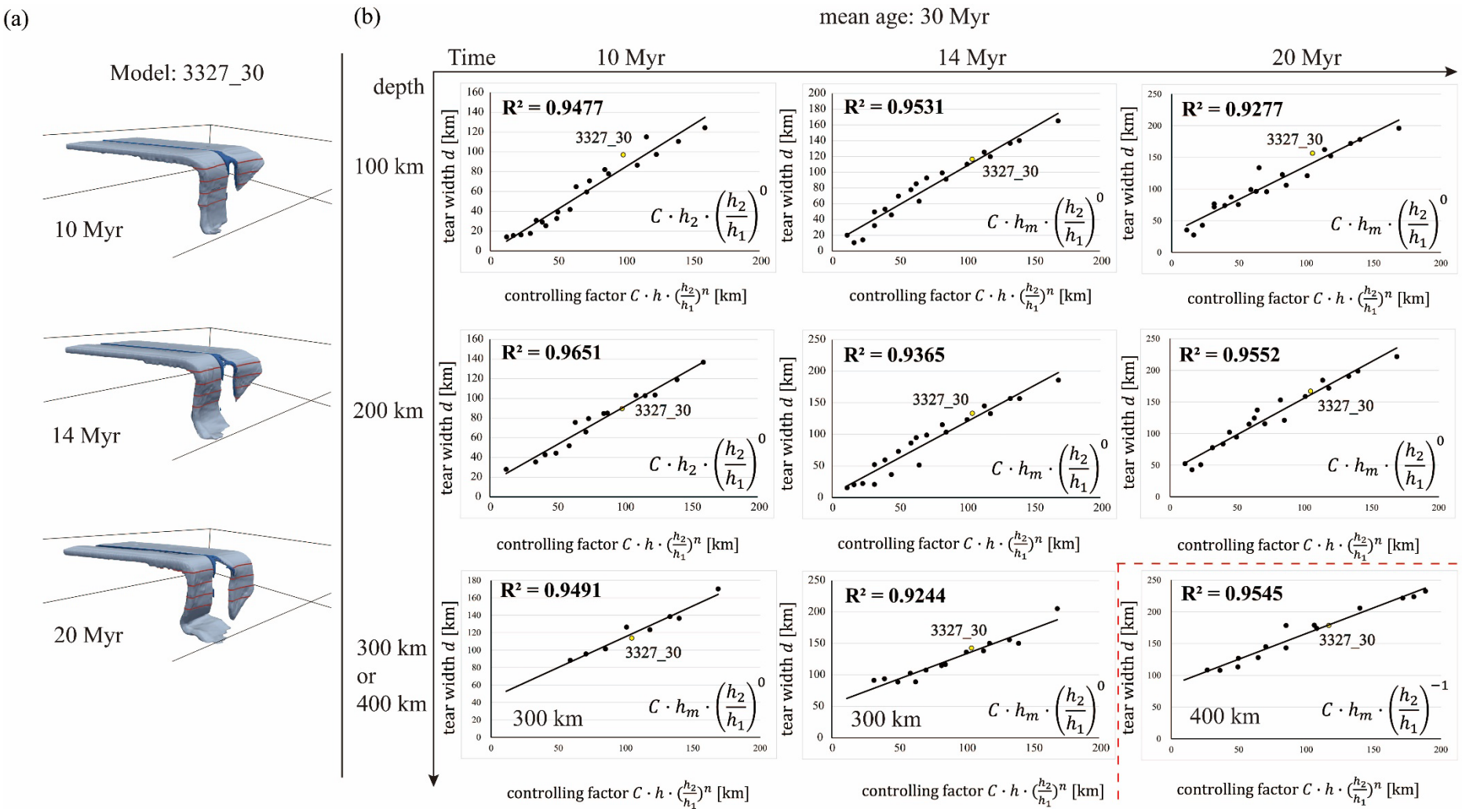

Figure 9. (a) Snapshots of particular model 3327_30 (slabs reference ages t_1=33 Myr, t_2=27 Myr, mean age 30 Myr, and subduction obliqueness θ=30°) at 10,

14, and 20 Myr, showing the evolution of the oceanic lithosphere tearing. The thin red curves on slabs are selected slices for geometry and tearing assessment computation (at 100, 200, 300, and 400 km depth). (b) The nine different panels display the correlation between slabs tearing horizontal width (d) and the integrated controlling factor ($\Delta v/k = C \cdot h \cdot f$). Correlation coefficients (R^2) are shown on the top-left corner of each panel. The control parameters are consistent within each one of the areas delimited by the red dashed line.

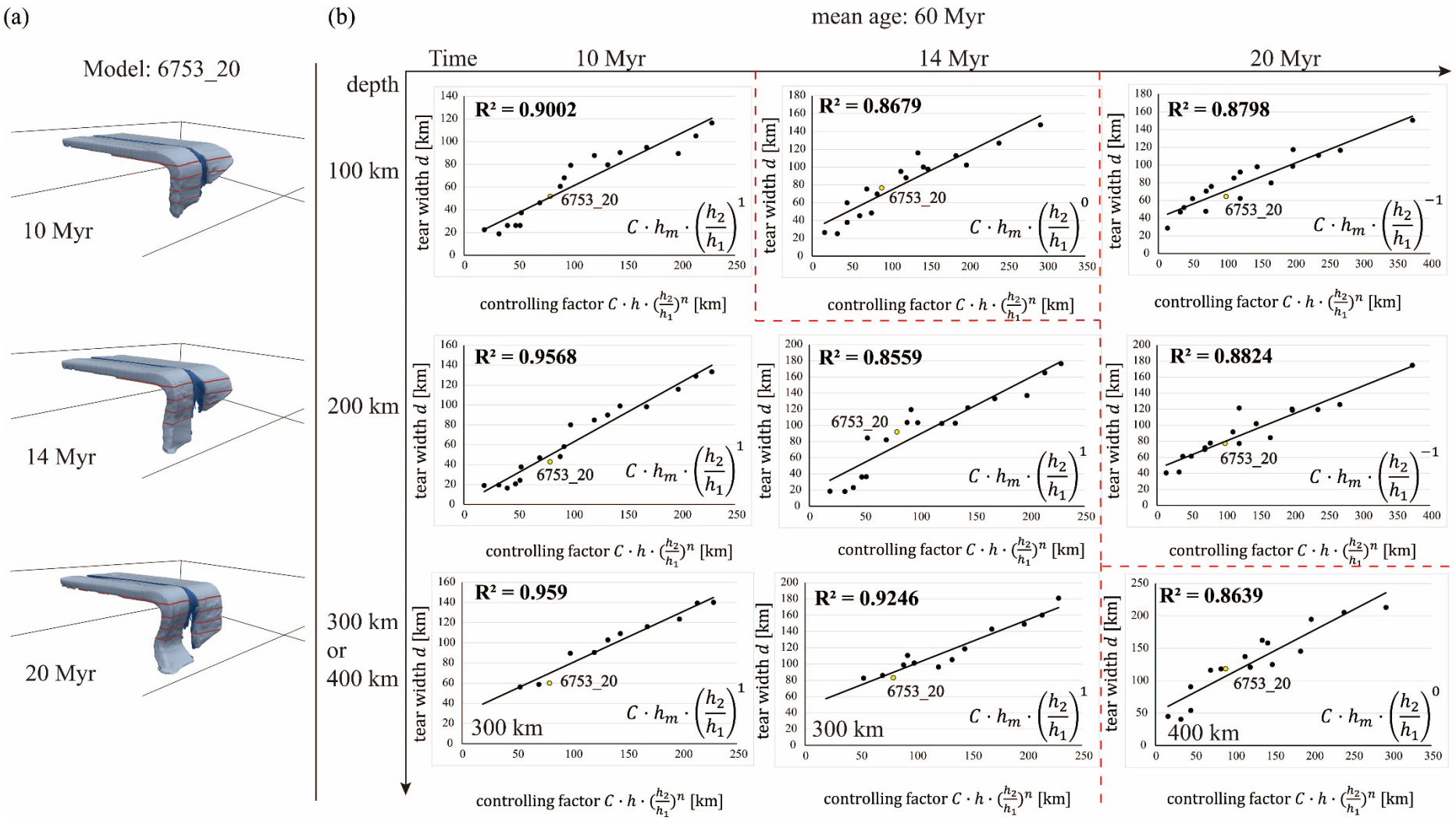
(a)
Model: 6753_20
10 Myr
14 Myr
20 Myr
(b)
mean age: 60 Myr
Time
10 Myr
14 Myr
20 Myr
depth
100 km
200 km
300 km
or
400 km
R² = 0.9002
R² = 0.8679
R² = 0.8798
R² = 0.9568
R² = 0.8559
R² = 0.8824
R² = 0.959
R² = 0.9246
R² = 0.8639
6753_20
300 km
400 km
tear width d [km]
controlling factor C · h · (h2/h1)^n [km]

Figure 10. (a) Snapshots of particular model 6753_20 (slabs reference ages t_1=67 Myr, t_2=53 Myr, mean age 60 Myr, and subduction obliqueness θ =20°) at 10, 14, and 20 Myr, showing the evolution of the oceanic lithosphere tearing. The red curves on slabs are selected slices for geometry and tearing assessment computation. (b) The nine different panels display the correlation between slabs tearing horizontal width (d) and the integrated controlling factor ($\Delta v/k = C \cdot h \cdot f$). Correlation coefficients (R^2) are shown on the top-left corner of each panel. The control parameters are consistent within each one of the areas delimited by the red dashed lines.

After a detailed analysis of our numerical experiments (Figures 8-10), we find that the tearing horizontal width d is sensibly and roughly proportional to the slabs' velocity difference. Our hypothesis is reasonably confirmed. If we consider the "full" scaling form for the velocity difference $\Delta v = k \cdot C \cdot h \cdot (h_2/h_1)^n$, the correlation coefficient R^2 is in the range of 0.76~0.97 (see Table 3) considering all depths and times, age groups and simulation cases. For comparison, if employing the much simpler "incomplete" scaling form $\Delta v = k \cdot C$, the range of R^2 is 0.69~0.96 for the same simulations cases as in the previous trial (see Table 3). Therefore, regarding the similarity between the two correlation-values intervals, it is inferred that the first-order governing factor is the oblique convergence given by the characteristic parameter $C=C(\theta)$, as defined in Equation 6.

Table 3. Correlation between the slabs tearing horizontal width d and the "full" scaling form for the velocity difference ($\Delta v = k \cdot C \cdot h \cdot f$) at different times and depths. In parentheses: Correlation between d and the "incomplete" scaling form ($\Delta v = k \cdot C$). The range of {min, arithmetic mean, max} values of correlations R^2 for the "full" and "incomplete" scaling forms are {0.76, 0.91, 0.97} and {0.69, 0.84, 0.96}, respectively.

R^2 (d, Δv) Mean age:15 Myr	10 Myr	14 Myr	20 Myr
100 km	0.92 (0.92)	0.92 (0.84)	0.89 (0.80)
200 km	0.76 (0.76)	0.96 (0.96)	0.91 (0.83)
300 km	——	——	——
400 km	——	——	——
R^2 (d, Δv) Mean age:30 Myr	10 Myr	14 Myr	20 Myr
100 km	0.95 (0.93)	0.95 (0.95)	0.93 (0.93)
200 km	0.97 (0.91)	0.94 (0.94)	0.96 (0.96)
300 km	0.95 (0.95)	0.92 (0.92)	——
400 km	——	——	0.95 (0.88)
R^2 (d, Δv) Mean age:60 Myr	10 Myr	14 Myr	20 Myr
100 km	0.90 (0.81)	0.87 (0.87)	0.88 (0.82)
200 km	0.96 (0.84)	0.86 (0.81)	0.88 (0.88)
300 km	0.96 (0.86)	0.92 (0.86)	——
400 km	——	——	0.86 (0.87)
R^2 (d, Δv) All simulations	10 Myr	14 Myr	20 Myr
100 km	0.90 (0.76)	0.86 (0.77)	0.90 (0.69)
200 km	0.91 (0.79)	0.90 (0.80)	0.91 (0.69)

300 km	0.87 (0.71)	0.83 (0.74)	——
400 km	——	——	0.86 (0.76)

In particular, if we divide each group of time-depth diagrams along the diagonal line (Figures 8-10), the parameter changes can roughly reflect the tearing width evolution in different segments of the ocean plate. Most parameters remain consistent within each one of the areas delineated by the red slash, reflecting the previous deformation history inherited by the slab during most of the subduction. The variation of parameters in various intervals from the lower left to the upper right depicts the variation of governing factors with subduction, which is dependent on $(h_2/h_1)^n$, like n = 0→-1 in the 15 Myr-age group and n = 1→0→-1 in the 60 Myr-age group (Figures 8b, 10b), and n = 0→-1 at 300-400 km depth in the 30 Myr-age group (Figure 9b).

This overall reduced evolution represents the effect of unbending resistance F_2 in various plate segments. The oceanic lithosphere subducted length l of slab-2 is obviously smaller than that of slab-1 during the early stages of subduction (well before the two slabs are dipping sub-vertically). The smaller l in slab-2, the stronger the unbending resistance and the apparently “stiffer” the slab. Accordingly, "stiffer" slab-2 affects the change of tearing width when $h=h_2$, $n=1$. The overall subduction dip angle (including that of slab-1) increases as slab-2 subducts, and the effects of F_2 grow weaker at this point with $h=h_{mean}$ and $n=0$. Later on, with continued slabs sinking, there is the singular event of slab-1 reaching 660 km depth: slab-1 is subjected to a force at the bottom that resists bending. At this point, the velocity-difference Δv turns to be controlled by slab-1, with the exponent transitioning to $n=-1$. As for the variation of the specific value of n in different age groups (15, 30, 60 Myr), we believe it is f that is also correlated with l_{b1}/l_{b2}. The changes in bending length compensate for some of the changes in slabs’ thickness ratio.

Finally, it can be seen that the controlling parameters change in the slabs deepest regions (400 km) on stage 2 (20 Myr) (Figure 9b, 10b). We think it is slab-1 here that is bent at the bottom of the model, that is associated with the folding pattern in the 30

Myr-age group and the trench retreating pattern in the 60 Myr-age group (Figure 9a, 10a) (Li & Ribe, 2012).

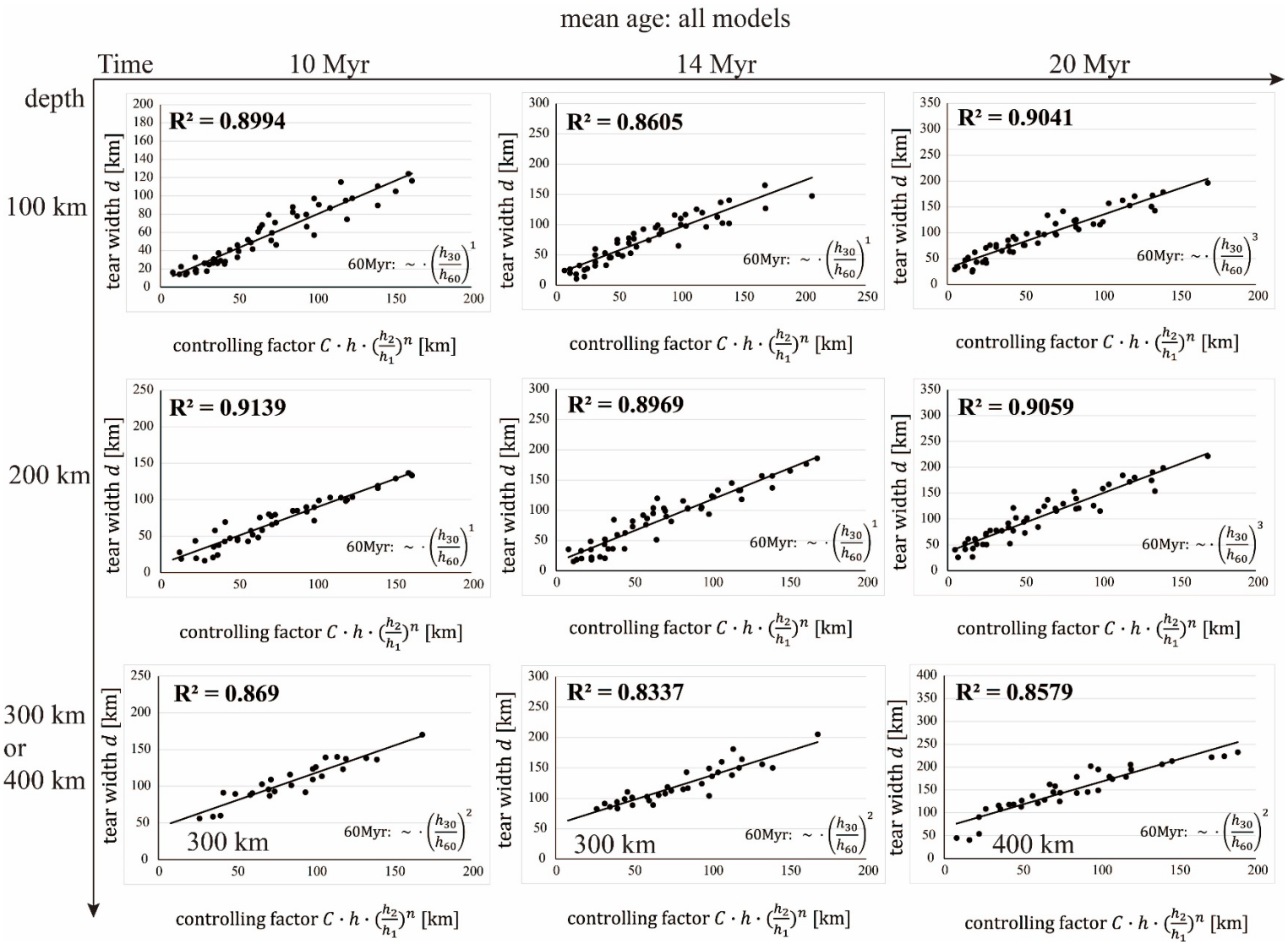
mean age: all models
Time
10 Myr
14 Myr
20 Myr
depth
100 km
200 km
300 km
or
400 km
R² = 0.8994
R² = 0.8605
R² = 0.9041
R² = 0.9139
R² = 0.8969
R² = 0.9059
R² = 0.869
R² = 0.8337
R² = 0.8579
300 km
400 km
60Myr: ~ · (h30/h60)^1
60Myr: ~ · (h30/h60)^3
60Myr: ~ · (h30/h60)^2
tear width d [km]
controlling factor C · h · (h2/h1)^n [km]

Figure 11. The nine panels display the correlation between slabs tearing width (d) and the integrated controlling factor ($\Delta v/k = C \cdot h \cdot f$) for all models. The correlation coefficients (R^2) are shown in the top left corner of each panel. We find that an additional multiplication factor $(h_{30}/h_{60})^p$ must be applied in the 60 Myr mean-age simulations for the $dv=k \cdot C \cdot h \cdot f$ function-group to capture a certain influence of slabs thickness differences on tearing width, and in this way they fit in reasonably with the other age groups.

The comparison among the models with different mean slab ages indicates that the older slabs of 60 Myr generally have a narrower tearing window than the mid-age slabs with mean ages of 30 Myr (Figures 4, 11).

Certainly, an additional multiplication factor $(h_{30}/h_{60})^p$ must be applied in the 60 Myr mean-age simulations to fit in with the other age groups at similar correlation levels (Figure 11). At old-plate ages (mean 60 Myr), the full scaling form $\Delta v = k \cdot C \cdot h \cdot f$ (with $f = (h_2/h_1)^n$) yields values that are too big (because h is big). Therefore, an additional post-factor <1 is needed to fit the observed values of d through the range of Δv values of the different simulations and to get similar correlation levels to those of the other age groups.

Beyond this, we believe that the smaller values of tearing width in the 60 Myr than in the 30 Myr age group may be related to the difference in bending length (to measure the effect of bending length (l_{b1}/l_{b2}), we use the average slab-thickness ratio $(h_{30}/h_{60})^p$, which can be compared quantitatively) involving viscous dissipation, with older-thicker slabs offering higher viscous resistance to bending and retarding the development of the bending-length increase. The sequence of slabs-1,2 changing from small to large bending length is different when plate age-thicknesses are large (Figure 6). The apparently rheologically weaker slab-1 changes "earlier" in the plate-thickness sinking-velocity parameter space than slab-2, increasing the tearing width from 15 Myr-age groups to 30 Myr-age groups and then decreasing (just to some extent) from 30 Myr-age groups to 60 Myr-age groups. This effect is more apparent in the later phases of subduction and at larger depths, as shown by the change of p in Figure 11. This feature is also shown in the shift of the age ratio cut-off with absolute age in Figure 4.

In summary, vertical oceanic-plate tearing is controlled by two dominant factors, (i) the subduction horizontal obliqueness: the larger the obliqueness angle, the larger the difference in the subducted area of the two slabs, the higher the likelihood for slabs tearing; (ii) the difference between the ages of the two slabs: tearing across/along the transform-fault zone is favored by older, heavier, thicker slab-1 relative to slab-2, as this configuration plays constructively with the obliqueness. The plate unbending

resistance effect varies among the individual slabs thicknesses and also among the different subduction zones (in real Earth), but seems to only play a secondary role in tearing generation and development.

4.2 On transform-fault-perpendicular tearing

In subsection 3.2 we showed that tearing horizontal-displacement-components ratio, when expressed in the transform-fault-based coordinate frame can take diverse values far-from yet about 1. If dominated by fault-parallel component, we recall that slabs differential roll-back and differential hinge retreat is a relatively normal phenomenon in geosciences. Contrastingly, if dominated by fault-perpendicular component the slabs may be slightly separating inside the asthenosphere, parallel to their transversal/hinge axes. We will shed light on this hitherto yet-to-be-understood phenomenon.

We already provided kinematical (visual displays of geometry versus time) evidence that this transform-fault-perpendicular tearing displacement can dominate the tearing, and that it manifests only for horizontal-obliqueness $\theta \leq 30°$ and more frequently in young slabs (section 3.2, Figure 5). We shall now show some supporting dynamical evidence for this tearing behavior.

Let's consider X' as the fault-parallel axis and Y' the fault-perpendicular axis. Appendix figure S1 displays the viscous horizontal shear stress on the slabs surface for simulation 1713_30 (lithospheric ages t_1 = 17 Ma, t_2 =13 Ma; horizontal obliqueness θ = 30°) which exemplifies transform-fault-perpendicular tearing. The viscous horizontal shear stress $\sigma_{y'x'}$ is shown at 6 and 12 Myr of computed geological time. Given the horizontal-obliqueness angle θ = 30°, the relative motion between the slabs and the overriding continental plate, particularly the tangential/trench-parallel component, influences the local stress field on the surface of these bodies: the surface viscous friction imprinted by the relative motion dictates the shear stress. The effects of this shearing may not be equal on the two slabs regarding their different ages and subducted volumes versus time, and the interaction with the overriding plate may even be unsteady in time, resulting in an increasing separation between the slabs.

Appendix figure S2 (in its left column) shows the viscous horizontal normal deviatoric stress on a 2D vertical slice along the transform-fault-zone central-axis for simulation 1713_30 exemplifying transform-fault-perpendicular tearing. The stress $\sigma_{y'y'}$ is shown at {4, 6, 8, 10, 12, 14} Myr of computed geological time. The normal deviatoric stress $\sigma_{y'y'}$ (left-side panel) inside the transform-fault-zone is extensive in-and-around the subduction hinge (bent), and slightly compressive where the slabs are close to each other far from the trench in the horizontal portions; and this stress pattern changes only slightly during this particular subduction process. With time, the fault-zone extensive stresses slightly oscillate in magnitude, meanwhile and incrementally, the slabs separate horizontally inside the ambient mantle (right-side panel).

4.3 On the trench-based alternative tearing patterns

In this study we opted to express the tearing horizontal-displacement vector in reference frames defined by the transform-fault-based system in each simulation, case by case depending on the horizontal-obliqueness angle. An interesting alternative is to use a universal (for all the simulations) reference frame, the one that defines the model-box: we shall now express the tearing in the 'universal' trench-based system, with axes X (trench-perpendicular) and Y (trench-parallel) as in Figure 2. This is important as the overriding continental plate with its fixed trench, is a common single entity which all the different simulated systems have and interact with.

In this 'universal' reference frame, the tearing displacement (dx,dy) is used to directly compute the magnitude of the tearing horizontal-components ratio |dx/dy| to characterize the tearing patterns. The values of this ratio tend to be <1 due to the horizontal obliqueness: when the angle θ>0° the "dy" component tends to be non-zero in most cases, but "dx" can be about zero in several cases. When the ratio is <0.5 trench-parallel tearing dominates thoroughly and more than half of the simulations are represented, and when >1 the pattern is trench-perpendicular-dominated but only 1 (in stage 1) and 4 (in stage 2) out of 69 cases were found.

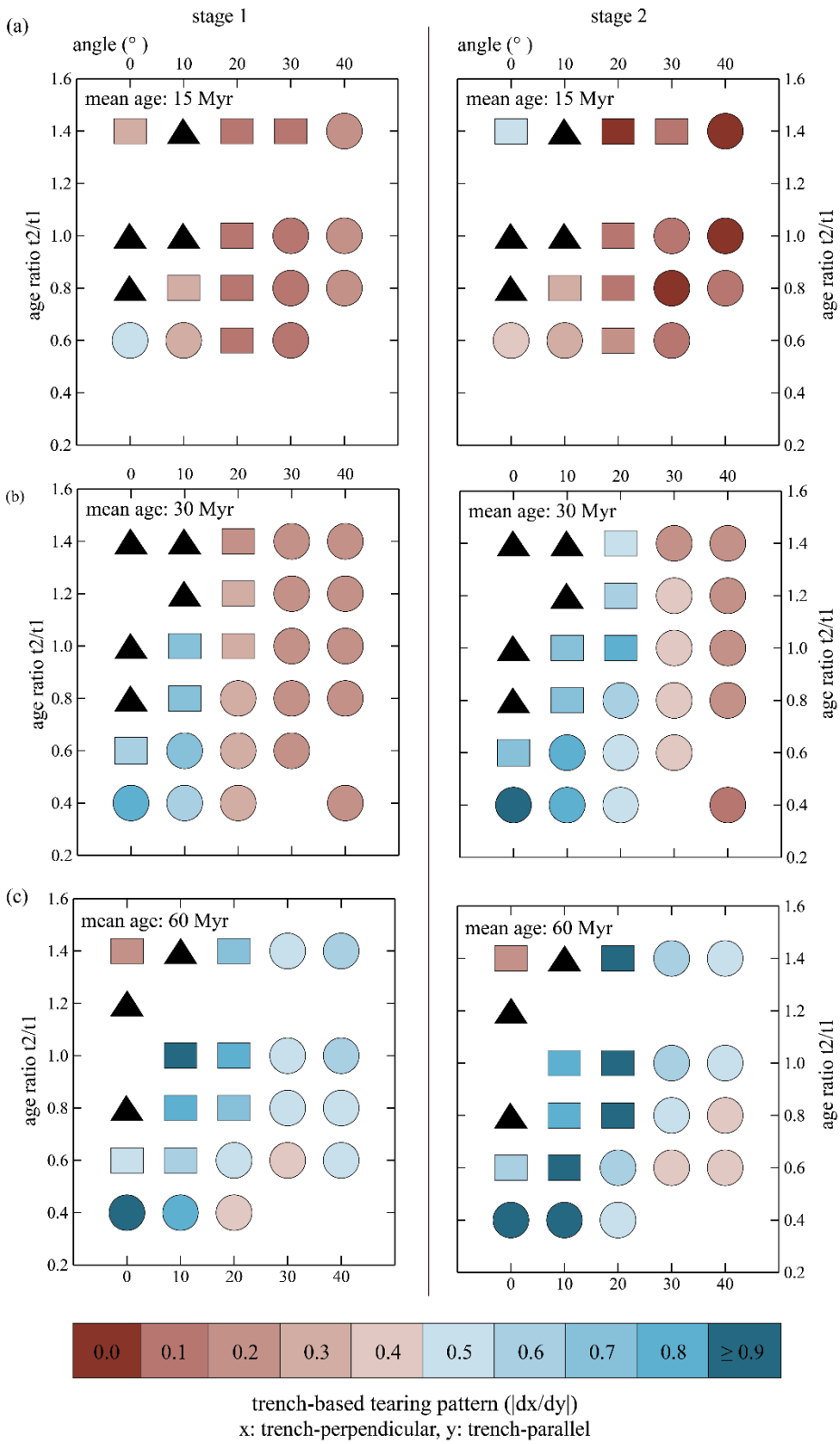

Figure 12. Check-box diagrams for trench-based tearing patterns on time-stages 1 (left) and 2 (right). *Angle* means the slabs' horizontal-obliqueness angle. The arithmetic-mean lithospheric age of plates 1 and 2, $((t_1+t_2)/2)$, is 15 Myr (a), 30 Myr (b), and 60 Myr (c), respectively. The category of slab trench-based tearing pattern, depending on the ratio "$|d_x/d_y|$". Red-color tones: $|d_x/d_y| < 0.5$, contrasting with Blue-color tones: $|d_x/d_y| \geqslant 0.5$.

The trench-based coordinate frame is as shown in Figure 2: X axis (trench-perpendicular), Y axis (trench-parallel). The definition of symbol shapes is the same as in Figure 4. Black triangles are the no-tearing simulations.

Particularly, when the subduction horizontal-obliqueness is zero, the two coordinate-frames coincide, and fault-perpendicular equals trench-parallel. Indeed, observing Figures 5 and 12, we can confirm that for angle θ=0° all the simulations colored in orange in Figure 5 have a ratio<0.7 colored correspondingly in Figure 12, and the only simulation colored blue (ratio >1.3) in Figure 5 is correspondingly colored as >0.9 in Figure 12. For obliqueness θ>0°, the relationship between the patterns from the two coordinate-frames-descriptions is non-trivial, specifically it is non-linear and given by trigonometric projections.

The overall tearing patterns in the trench-based system are the following:

(i) Trench-parallel tearing is mostly a young-slabs at high horizontal-obliqueness phenomenon: There is a clear dominance of ratio values <0.5 (strong trench-parallel tearing displacement) for young-intermediate (15-30 Myr) ages, and being more prevalent for high obliqueness angles but virtually independent of transform-fault age ratios. Aside from this, for young slabs this pattern accentuates with temporal evolution, more prevalent and intense in stage 2 after one slab reaches the bottom; and only slightly more prevalent in late stage for the 60 Myr age group; however, the opposite occurs for mid-age slabs (pattern is more prevalent at early stage).

(ii) The trench-perpendicular tearing-displacement component, being relatively smaller in general, becomes significant only for intermediate-old (30-60 Myr) ages and mostly low horizontal-obliqueness (for the transform-fault-parallel tearing to project effectively on that axis). The components-ratio becomes comparable or larger than unit (ratio ≳1) only in a few simulations (Figure 12). Also, trench-perpendicular tearing component becomes (excepting for two simulations) more important (prevalent and intense) in late times in stage 2, as an effect of one slab reaching the bottom and blocking the motion for some time.

The evident dominance and prevalence of trench-parallel tearing (ratios<0.5), being

common for young slabs' mean ages and high obliqueness angles, is interpreted as: Young ages signify smaller sinking-velocity differences (constructively-combined with older slab-2 preventing excessive vertical separation, in the 15 Myr group only) combined with high obliqueness angles that signify higher trench-parallel relative velocities between slabs and trench, thus higher viscous trench-parallel shear stress on the contact. These conditions, of low vertical velocity-displacement difference between slabs, with high tangential forces on them, may favor the dominance of trench-parallel tearing. On the other hand, the manifestation of trench-perpendicular tearing is more complex, as it not only depends on the time stage, but perhaps on an obvious trade-off: similar constructive-tearing results for low age-ratio (relatively older slab-1) and high obliqueness angle, which can result in non-uniform (differential) rollback and smaller (delayed) bending-length of "apparently stiffer" plate 2, respectively. Finally, as seen in figure 12, the overall temporal change of patterns between stages 1 and 2 is due to one slab reaching the bottom, and the consequential difference in sinking-subducting style that ensues, which affects the slabs tearing displacement.

4.4. Geological application

As shown in Figure 13, examples of slab tearing of natural subduction zones are projected onto our model phase diagrams. Some cases (such as "Central America subduction zone (cam-1)" and "Alaska subduction zone (ala)") occur simultaneously in two mean-age groups, given our sparse and imprecise sampling of this variable. Except for the "Alaska (ala)" point, all the natural cases fall in our model-predicted regime where tearing occurs. The misfit of the "Alaska (ala)" case may be due to a secondary plate with different seafloor ages (Yang & Gao, 2020). Furthermore, because the horizontal-obliqueness angle of "Caribbean (car)" subduction is ≥60°, we have not carried out corresponding simulations considering the numerical stability problems they face. According to our analysis, the Aleutian slab window's low-velocity zone emplaced on a high oblique-convergence angle may undergo tearing due to slab-1 bending enforced by the overriding plate (Bai et al., 2020).

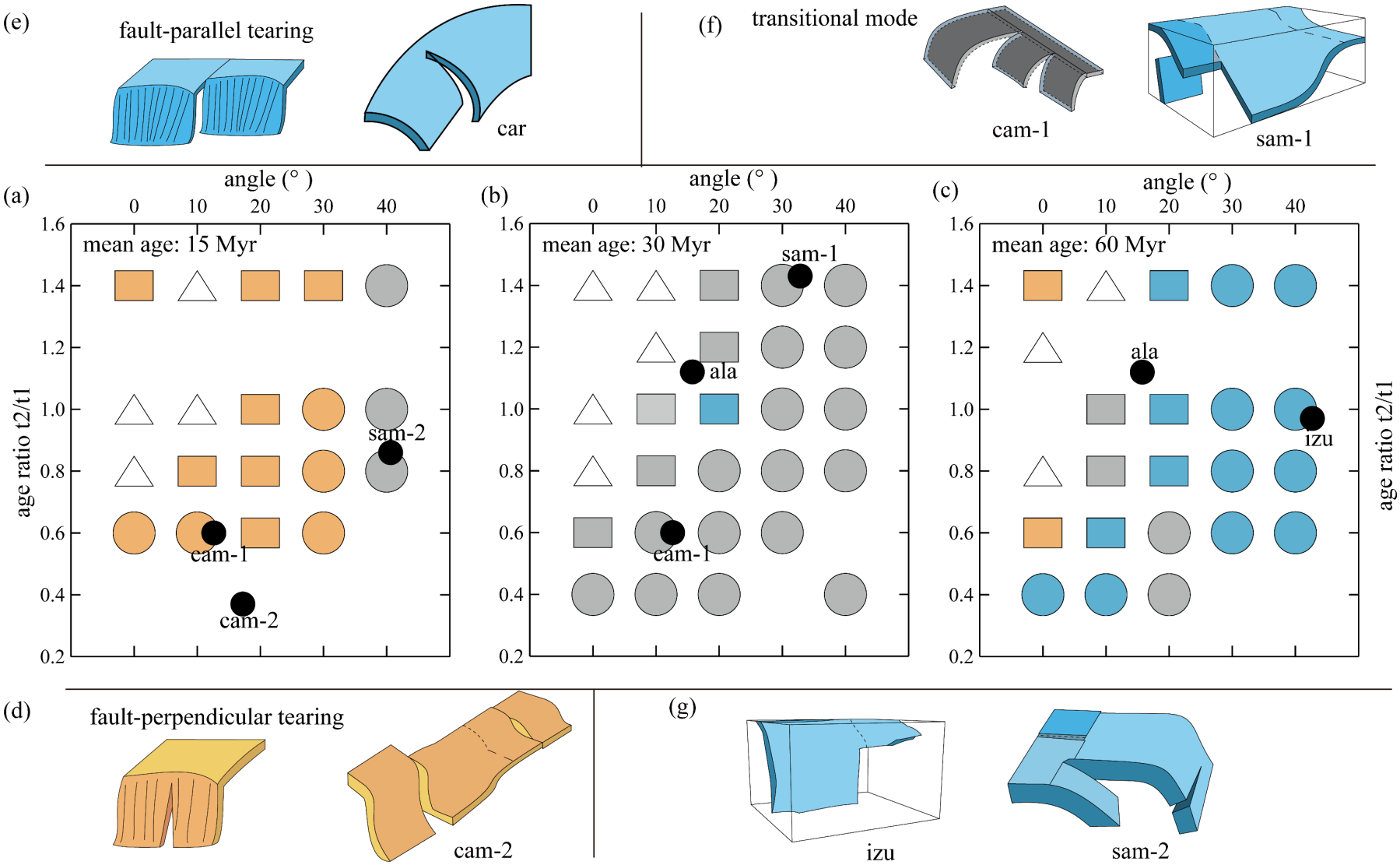
(e)
fault-parallel tearing
car
(f)
transitional mode
cam-1
sam-1
(a)
angle (°)
0
10
20
30
40
mean age: 15 Myr
sam-2
cam-1
cam-2
(b)
mean age: 30 Myr
sam-1
ala
cam-1
(c)
mean age: 60 Myr
ala
izu
age ratio t2/t1
1.6
1.4
1.2
1.0
0.8
0.6
0.4
0.2
(d)
fault-perpendicular tearing
cam-2
(g)
izu
sam-2

Figure 13. Comparisons between our numerical-model predictions on time-stage 2 (phase diagrams color-coded for tearing pattern and shape-coded for overall tearing occurrence) and natural subduction-zones observations (small black circles) along with their simplified observation-based interpreted structures (cartoons). The "Alaska **(ala)**" natural case falling in the predicted no-tearing zone may be affected by a secondary, so far unobserved, slab tear. In contrast, the "South America **(sam-1 and sam-2)** differential retreat" case with a fault-parallel pattern may be affected by a lateral break-off in the younger slab but also lack more detailed local observations. Colored diagram: the same as in Figure 5.

We measured the tear widths observed in the literature. We projected the tearing widths onto the convergence (transform-fault-parallel) direction and its perpendicular direction, which were used to determine the corresponding vertical tearing patterns (Caribbean (car):(Meighan et al., 2013); South America (sam-1):(Pesicek et al., 2012); Central America (cam-1): (Stubailo et al., 2012); Central America (cam-2):(Carciumaru et al., 2020)) (Figure S3). Colored cartoons represent the tearing patterns in nature, and the tearing patterns predicted by the model are represented by colors in the phase diagram (Figure 13).

We find that fault-perpendicular tearing manifests in "Central America (cam-2)", the transitional node manifests in "Central America (cam-1)", and fault-parallel tearing manifests in "Caribbean (car)" and "Izu-Bonin (izu)."

The simulations do not fit the real "South America (sam-1 and sam-2)" tearing pattern, most likely due to the real plate being too thin and experiencing break-off during subduction, as shown in Figure 1 and Table 1, which increases the tearing width in the along-fault direction. According to our understanding, the vertical tearing pattern of "Kamchatka (kam)" is most likely fault-parallel tearing.

In order to investigate whether our model can be applied to other types of subduction, such as "Calabria (cal)" involving ocean-continental transition zone, "Izu-Bonin (izu)" and "South America (sam-2)" involving ridge subduction, we performed six comparative experiments of oblique subduction with/without ocean-continental transition and oblique subduction with/without a ridge (Figure S4, S5). We find that a less-dense continental crust, as expected, causes flat subduction of the slab on that side, thus causing our transform-faulted oceanic slabs model to be inapplicable to the subduction of continental material. For a ridge subduction case, as long as a weak zone exists in front of the ridge, the presence of this latter does not change the vertical tearing results/pattern of the forward slab, indicating that our model can be potentially applied to cases where a weak zone exists in front of the ridge (Figure S6). In addition, we find that when the oceanic ridge is at the front edge of the plate, and the weak zone is behind, its oblique subduction results in a pattern similar to the tearing pattern of the opposite

rotation of slab segments (Gianni et al., 2019) (Figure S6). Details of oblique subduction of a ridge need to be studied further in dedicated future studies.

We also carried out additional simulations altering the viscosity of the weak transform-fault zone and found that a high-enough fault-zone viscosity can (in some cases) preclude and inhibit tearing. However, we must note that when slab-2 is not entirely subducted during the early stages of subduction evolution, the variable slab length l along the trench generates transverse non-uniform slab "stiffness" (Li & Ribe, 2012). In these cases, the deformation results in a continuous variation in subduction dip angle (Figure S7), like the imaging on the right side of "South America (sam-1)" (Figure 1).

4.3. Model limitations

Our model is simplified by having constant (yet adequate) density, viscosity, and thermal properties values. This was chosen to isolate the first-order controls on the slab tearing during transform-fault subduction. This simplification, also applied in order to facilitate the quantitative scaling analysis, may lead to some inaccuracies related to the following:

(1) The age difference between the two sides of the transform fault should lead to additional lateral variations in the oceanic plate's physical properties (e.g., viscosities).

(2) The viscosity and density should vary continuously with depth (pressure and temperature), particularly through and between lithospheric and asthenospheric mantle regions.

(3) Additional complexities and effects on the sinking-tearing plate, i.e., more specific and refined forms of the post-factor function f, were not tried.

(4) The obliqueness angle and age-ratio in the natural cases may have changed through time. Therefore, their values during the early stages of subduction (Myr ago) may differ from those observed at the present day.

All the aforementioned neglected factors/processes can influence the slabs' tearing vector (magnitude and direction) at all stages during subduction. However, we believe that the first-order controlling mechanisms are adequately represented in our study.

5. Conclusions

Subduction horizontal obliqueness and slabs' transform-fault age-offset play dominant first-order roles in the development and evolution of slabs tearing during the subduction of such complex systems. The viscous unbending resistance varies among the two subducting slabs during the subduction process, and also varies among different subduction zones, yet it seems to only have a secondary role in slab tearing.

When the subduction horizontal-obliqueness angle is ≥30° or the age ratio of slab-2 to slab-1 is less than 0.6, fast and well-developed oceanic plate vertical tearing occurs and develops inside the mantle without any other requirements. In contrast, no tearing occurs for small obliqueness angles (<20°) if slab-2 is approximately older and thicker (age ratio >0.6-0.8).

The vector nature of slab tearing can occur/be decomposed in two patterns or modes when referred to the convergence direction or transform-fault orientation: fault-parallel and fault-perpendicular tearing. Fault-perpendicular tearing manifests mostly (not solely) in young-age slabs and for medium-low subduction horizontal-obliqueness angles (≤30°) and somewhat more favorably for low-age ratios (slab-1 being older). Fault-parallel tearing (related to differential slabs-hinge retreat or rollback) is relatively well-known and manifests almost solely for old-age slabs (60 Myr-mean-age group) and mostly for medium-high obliqueness (~>20°) angles but almost independently of age ratios.

Transform-fault-perpendicular tearing of subducting slabs' is here kinematically identified fairly/slightly above numerical errors and model uncertainties, and classified in a parametric way using the tearing horizontal-distance vector. Dynamically speaking, some of our simulations suggest that this tearing mode is accompanied by viscous horizontal normal deviatoric stresses of extension across the weak fault-zone, in-and-around the hinge (subduction bent) region, with some slight variations in time; all of this concomitant to the slabs' increasing horizontal separation inside the ambient mantle. Future research is needed to better understand this particular tearing behavior, but hereby we have provided a first step in that direction.

Compared to the several transform-fault-based systems in our simulations, the universal trench-based reference frame is defined by a single common entity (overriding plate), and when the slabs' horizontal-obliqueness angle is 0° (normal subduction) the two reference frames coincide. Trench-parallel tearing is frequent and dominant for young slabs, and may be caused by low vertical-velocity difference between slabs, and moving at high horizontal-obliqueness angles (~>20°) causing high tangential shear stress at the trench. Trench-perpendicular tearing is relatively infrequent and likely an old-age phenomenon (~>30 Myr), favored by mid-low obliqueness angles, and closely related to non-uniform slabs rollback.

Our modeling suggests that the continual spatial variation in dip angle along the trench observed in real-Earth subduction zones could be potentially related to the initial evolution of subducting slabs under horizontally-oblique convergence. Further beyond, knowing the age combination across a transform fault (ratio and average) and the horizontal obliqueness of an oceanic subduction scenario would, with a framework like the one here presented, allow a prediction of the tearing occurrence, potential pattern, and the likely evolution of the subducting slabs, and perhaps of the associated locally-perturbed mantle flow.

Acknowledgments

We appreciate Dr. Yimin Jin's great help in troubleshooting-running the ASPECT software. We appreciate comments on the article from anonymous reviewers. We thank National Supercomputing Center in Chengdu, China, for the support during the parallel computing lengthy tasks. This research is supported by the National Science Foundation of China (U2239205, 41725017) and the National Key R&D Program of the Ministry of Science and Technology of China (2020YFA0713401). It is also partially supported by the National Key Scientific and Technological Infrastructure project "Earth System Science Numerical Simulator Facility" (EarthLab).

The original datasets are published as a Zenodo data package (https://zenodo.org/record/7898295#.ZFSf6XZByUk). The numerical software ASPECT (version 2.3.0) is from

https://github.com/geodynamics/aspect/releases/tag/v2.3.0, and the visualization software ParaView is https://www.paraview.org/. Figure 1 is plotted with GMT https://www.generic-mapping-tools.org/, and the original data on the subduction zone, seafloor age, plate velocity, and color bar is referred to (Hayes et al., 2018)(Müller et al., 2008)(Becker et al., 2015)(Crameri, 2021), respectively.

References

Bai, Y., Zhang, D., Dong, D., Wu, S., & Wang, Z. (2020). Aleutian island arc magma production rates and primary controlling factors. *Marine Geology*, *430*, 106346. https://doi.org/10.1016/j.margeo.2020.106346

Bangerth, W., Dannberg, J., Fraters, M., Gassmoeller, R., Glerum, A., Heister, T., & Naliboff, J. (2021). *ASPECT v2.3.0*. Zenodo. https://doi.org/10.5281/zenodo.5131909

Becker, T. W., Schaeffer, A. J., Lebedev, S., & Conrad, C. P. (2015). Toward a generalized plate motion reference frame. *Geophysical Research Letters*, *42*(9), 3188–3196. https://doi.org/10.1002/2015GL063695

Bolton, A. R., Schutt, D. L., Aster, R. C., Audet, P., Schaeffer, A. J., Estève, C., et al. (2022). Evidence for asthenospheric flow rotation in northwest Canada: insights from shear wave splitting. *Geophysical Journal International*, *228*(3), 1780–1792. https://doi.org/10.1093/gji/ggab396

Bonnardot, M.-A., Régnier, M., Christova, C., Ruellan, E., & Tric, E. (2009). Seismological evidence for a slab detachment in the Tonga subduction zone. *Tectonophysics*, *464*(1), 84–99. https://doi.org/10.1016/j.tecto.2008.10.011

Burkett, E. R., & Billen, M. I. (2010). Three-dimensionality of slab detachment due to ridge-trench collision: Laterally simultaneous boudinage versus tear propagation. *Geochemistry, Geophysics, Geosystems*, *11*(11). https://doi.org/10.1029/2010GC003286

Carciumaru, D., Ortega, R., Castellanos, J. C., & Huesca-Pérez, E. (2020). Crustal Characteristics in the Subduction Zone of Mexico: Implication of the Tectonostratigraphic Terranes on Slab Tearing. *Seismological Research Letters*,

91(3), 1781–1793. https://doi.org/10.1785/0220190117

Crameri, F. (2021). *Scientific colour maps*. Zenodo. https://doi.org/10.5281/zenodo.5501399

Cui, Q., & Li, Z.-H. (2022). Along-Strike Variation of Convergence Rate and Pre-Existing Weakness Contribute to Indian Slab Tearing Beneath Tibetan Plateau. *Geophysical Research Letters*, *49*(4), e2022GL098019. https://doi.org/10.1029/2022GL098019

Dougherty, S. L., & Clayton, R. W. (2014). Seismicity and structure in central Mexico: Evidence for a possible slab tear in the South Cocos plate. *Journal of Geophysical Research: Solid Earth*, *119*(4), 3424–3447. https://doi.org/10.1002/2013JB010883

Duretz, T., Gerya, T. V., & May, D. A. (2011). Numerical modelling of spontaneous slab breakoff and subsequent topographic response. *Tectonophysics*, *502*(1), 244–256. https://doi.org/10.1016/j.tecto.2010.05.024

Fernández-García, C., Guillaume, B., & Brun, J.-P. (2019). 3D slab breakoff in laboratory experiments. *Tectonophysics*, *773*, 228223. https://doi.org/10.1016/j.tecto.2019.228223

Freeburn, R., Bouilhol, P., Maunder, B., Magni, V., & van Hunen, J. (2017). Numerical models of the magmatic processes induced by slab breakoff. *Earth and Planetary Science Letters*, *478*, 203–213. https://doi.org/10.1016/j.epsl.2017.09.008

Georgieva, V., Melnick, D., Schildgen, T. F., Ehlers, T. A., Lagabrielle, Y., Enkelmann, E., & Strecker, M. R. (2016). Tectonic control on rock uplift, exhumation, and topography above an oceanic ridge collision: Southern Patagonian Andes (47°S), Chile. *Tectonics*, *35*(6), 1317–1341. https://doi.org/10.1002/2016TC004120

Gerya, T. (2022). Numerical modeling of subduction: State of the art and future directions. *Geosphere*, *18*(2), 503–561. https://doi.org/10.1130/GES02416.1

Gianni, G. M., & Luján, S. P. (2021). Geodynamic controls on magmatic arc migration and quiescence. *Earth-Science Reviews*, *218*, 103676. https://doi.org/10.1016/j.earscirev.2021.103676

Gianni, G. M., Navarrete, C., & Spagnotto, S. (2019). Surface and mantle records reveal an ancient slab tear beneath Gondwana. *Scientific Reports*, *9*(1), 19774. https://doi.org/10.1038/s41598-019-56335-9

Glerum, A., Thieulot, C., Fraters, M., Blom, C., & Spakman, W. (2018). Nonlinear viscoplasticity in ASPECT: benchmarking and applications to subduction. *Solid Earth*, *9*(2), 267–294. https://doi.org/10.5194/se-9-267-2018

Govers, R., & Wortel, M. J. R. (2005). Lithosphere tearing at STEP faults: response to edges of subduction zones. *Earth and Planetary Science Letters*, *236*(1), 505–523. https://doi.org/10.1016/j.epsl.2005.03.022

Govers, Rob, & Fichtner, A. (2016). Signature of slab fragmentation beneath Anatolia from full-waveform tomography. *Earth and Planetary Science Letters*, *450*, 10–19. https://doi.org/10.1016/j.epsl.2016.06.014

Guillaume, B., Moroni, M., Funiciello, F., Martinod, J., & Faccenna, C. (2010). Mantle flow and dynamic topography associated with slab window opening: Insights from laboratory models. *Tectonophysics*, *496*(1), 83–98. https://doi.org/10.1016/j.tecto.2010.10.014

Hayes, G. P., Moore, G. L., Portner, D. E., Hearne, M., Flamme, H., Furtney, M., & Smoczyk, G. M. (2018). Slab2, a comprehensive subduction zone geometry model. *Science*. https://doi.org/10.1126/science.aat4723

Hildebrand, R. S., Whalen, J. B., & Bowring, S. A. (2018). Resolving the crustal composition paradox by 3.8 billion years of slab failure magmatism and collisional recycling of continental crust. *Tectonophysics*, *734–735*, 69–88. https://doi.org/10.1016/j.tecto.2018.04.001

Jolivet, L., Menant, A., Sternai, P., Rabillard, A., Arbaret, L., Augier, R., et al. (2015). The geological signature of a slab tear below the Aegean. *Tectonophysics*, *659*, 166–182. https://doi.org/10.1016/j.tecto.2015.08.004

Jolivet, L., Menant, A., Roche, V., Pourhiet, L. L., Maillard, A., Augier, R., et al. (2021). Transfer zones in Mediterranean back-arc regions and tear faults. *BSGF - Earth Sciences Bulletin*, *192*, 11. https://doi.org/10.1051/bsgf/2021006

Király, Á., Portner, D. E., Haynie, K. L., Chilson-Parks, B. H., Ghosh, T., Jadamec, M.,

et al. (2020). The effect of slab gaps on subduction dynamics and mantle upwelling. *Tectonophysics*, *785*, 228458. https://doi.org/10.1016/j.tecto.2020.228458

Kufner, S.-K., Schurr, B., Haberland, C., Zhang, Y., Saul, J., Ischuk, A., & Oimahmadov, I. (2017). Zooming into the Hindu Kush slab break-off: A rare glimpse on the terminal stage of subduction. *Earth and Planetary Science Letters*, *461*, 127–140. https://doi.org/10.1016/j.epsl.2016.12.043

Levin, V., Shapiro, N., Park, J., & Ritzwoller, M. (2002). Seismic evidence for catastrophic slab loss beneath Kamchatka. *Nature*, *418*(6899), 763–767. https://doi.org/10.1038/nature00973

Li, Z.-H., & Ribe, N. M. (2012). Dynamics of free subduction from 3-D boundary element modeling. *Journal of Geophysical Research: Solid Earth*, *117*(B6). https://doi.org/10.1029/2012JB009165

Li, Z.-H., Xu, Z., Gerya, T., & Burg, J.-P. (2013). Collision of continental corner from 3-D numerical modeling. *Earth and Planetary Science Letters*, *380*, 98–111. https://doi.org/10.1016/j.epsl.2013.08.034

Liu, K., Zhang, J., Xiao, W., Wilde, S. A., & Alexandrov, I. (2020). A review of magmatism and deformation history along the NE Asian margin from ca. 95 to 30 Ma: Transition from the Izanagi to Pacific plate subduction in the early Cenozoic. *Earth-Science Reviews*, *209*, 103317. https://doi.org/10.1016/j.earscirev.2020.103317

Liu, L., Liu, L., & Xu, Y.-G. (2021). Mesozoic intraplate tectonism of East Asia due to flat subduction of a composite terrane slab. *Earth-Science Reviews*, *214*, 103505. https://doi.org/10.1016/j.earscirev.2021.103505

Magni, V., Faccenna, C., van Hunen, J., & Funiciello, F. (2014). How collision triggers backarc extension: Insight into Mediterranean style of extension from 3-D numerical models. *Geology*, *42*(6), 511–514. https://doi.org/10.1130/G35446.1

Meighan, H. E., Pulliam, J., Brink, U. ten, & López-Venegas, A. M. (2013). Seismic evidence for a slab tear at the Puerto Rico Trench. *Journal of Geophysical Research: Solid Earth*, *118*(6), 2915–2923. https://doi.org/10.1002/jgrb.50227

Miller, M. S., Kennett, B. L. N., & Lister, G. S. (2004). Imaging changes in morphology, geometry, and physical properties of the subducting Pacific plate along the Izu–Bonin–Mariana arc. *Earth and Planetary Science Letters*, *224*(3), 363–370. https://doi.org/10.1016/j.epsl.2004.05.018

Miller, Meghan S., Gorbatov, A., & Kennett, B. L. N. (2006). Three-dimensional visualization of a near-vertical slab tear beneath the southern Mariana arc. *Geochemistry, Geophysics, Geosystems*, *7*(6). https://doi.org/10.1029/2005GC001110

Müller, R. D., Sdrolias, M., Gaina, C., & Roest, W. R. (2008). Age, spreading rates, and spreading asymmetry of the world's ocean crust. *Geochemistry, Geophysics, Geosystems*, *9*(4). https://doi.org/10.1029/2007GC001743

Pesicek, J. D., Engdahl, E. R., Thurber, C. H., DeShon, H. R., & Lange, D. (2012). Mantle subducting slab structure in the region of the 2010 M8.8 Maule earthquake (30–40°S), Chile. *Geophysical Journal International*, *191*(1), 317–324. https://doi.org/10.1111/j.1365-246X.2012.05624.x

Pusok, A. E., Kaus, B. J. P., & Popov, A. A. (2018). The effect of rheological approximations in 3-D numerical simulations of subduction and collision. *Tectonophysics*, *746*, 296–311. https://doi.org/10.1016/j.tecto.2018.04.017

Ribe, N. M. (2001). Bending and stretching of thin viscous sheets. *Journal of Fluid Mechanics*, *433*, 135–160. https://doi.org/10.1017/S0022112000003360

Roche, V., Sternai, P., Guillou-Frottier, L., Menant, A., Jolivet, L., Bouchot, V., & Gerya, T. (2018). Emplacement of metamorphic core complexes and associated geothermal systems controlled by slab dynamics. *Earth and Planetary Science Letters*, *498*, 322–333. https://doi.org/10.1016/j.epsl.2018.06.043

Rosenbaum, G., Gasparon, M., Lucente, F. P., Peccerillo, A., & Miller, M. S. (2008). Kinematics of slab tear faults during subduction segmentation and implications for Italian magmatism. *Tectonics*, *27*(2). https://doi.org/10.1029/2007TC002143

Schubert, G., Turcotte, D. L., & Olson, P. (2001). *Mantle Convection in the Earth and Planets* (1st ed.). Cambridge University Press.

https://doi.org/10.1017/CBO9780511612879

Stubailo, I., Beghein, C., & Davis, P. M. (2012). Structure and anisotropy of the Mexico subduction zone based on Rayleigh-wave analysis and implications for the geometry of the Trans-Mexican Volcanic Belt. *Journal of Geophysical Research: Solid Earth*, *117*(B5). https://doi.org/10.1029/2011JB008631

Suckale, J., Rondenay, S., Sachpazi, M., Charalampakis, M., Hosa, A., & Royden, L. H. (2009). High-resolution seismic imaging of the western Hellenic subduction zone using teleseismic scattered waves. *Geophysical Journal International*, *178*(2), 775–791. https://doi.org/10.1111/j.1365-246X.2009.04170.x

Thorkelson, D. J. (1996). Subduction of diverging plates and the principles of slab window formation. *Tectonophysics*, *255*(1), 47–63. https://doi.org/10.1016/0040-1951(95)00106-9

Turcotte, D. L., & Schubert, G. (2002). *Geodynamics* (2nd ed.). Cambridge University Press. https://doi.org/10.1017/CBO9780511807442

Vargas, C. A., & Mann, P. (2013). Tearing and Breaking Off of Subducted Slabs as the Result of Collision of the Panama Arc-Indenter with Northwestern South America. *Bulletin of the Seismological Society of America*, *103*(3), 2025–2046. https://doi.org/10.1785/0120120328

Xu, Y., Wang, Q., Tang, G., Wang, J., Li, H., Zhou, J., et al. (2020). The origin of arc basalts: New advances and remaining questions. *Science China Earth Sciences*, *63*(12), 1969–1991. https://doi.org/10.1007/s11430-020-9675-y

Yang, X., & Gao, H. (2020). Segmentation of the Aleutian-Alaska Subduction Zone Revealed by Full-Wave Ambient Noise Tomography: Implications for the Along-Strike Variation of Volcanism. *Journal of Geophysical Research: Solid Earth*, *125*(11), e2020JB019677. https://doi.org/10.1029/2020JB019677

Figure 1.

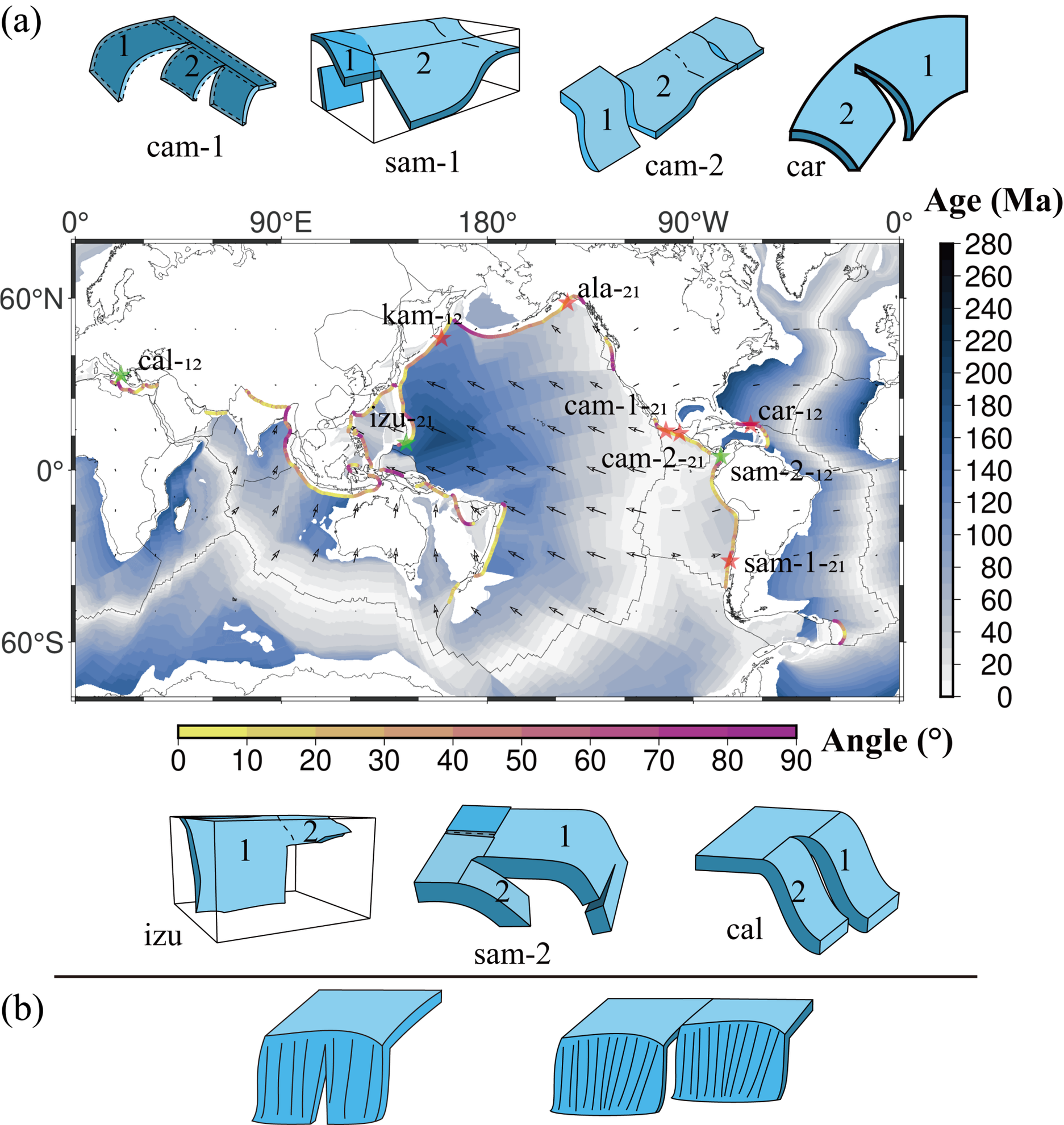
(a)
cam-1
sam-1
cam-2
car
Age (Ma)
0°
90°E
180°
90°W
0°
60°N
0°
60°S
ala-21
kam-12
cal-12
izu-21
cam-1-21
car-12
cam-2-21
sam-2-12
sam-1-21
280
260
240
220
200
180
160
140
120
100
80
60
40
20
0
0
10
20
30
40
50
60
70
80
90
Angle (°)
izu
sam-2
cal
(b)

Figure 2.

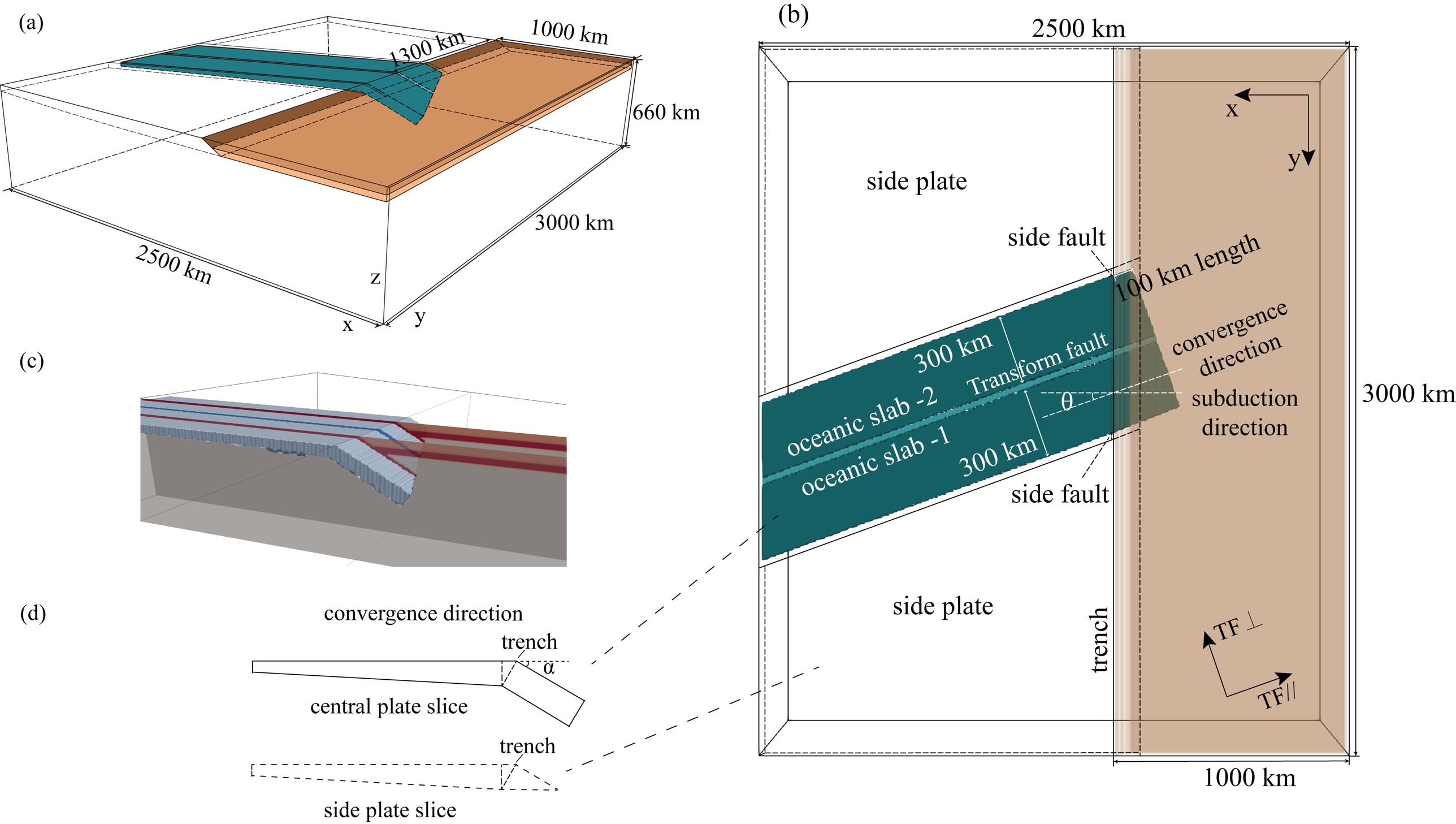
(a)
1300 km
1000 km
660 km
3000 km
2500 km
z
x
y
(b)
2500 km
x
y
side plate
side fault
100 km length
300 km
Transform fault
convergence direction
θ
subduction direction
oceanic slab -2
oceanic slab -1
300 km
side fault
3000 km
side plate
trench
TF ⊥
TF ||
1000 km
(c)
(d)
convergence direction
trench
α
central plate slice
trench
side plate slice

Figure 3.

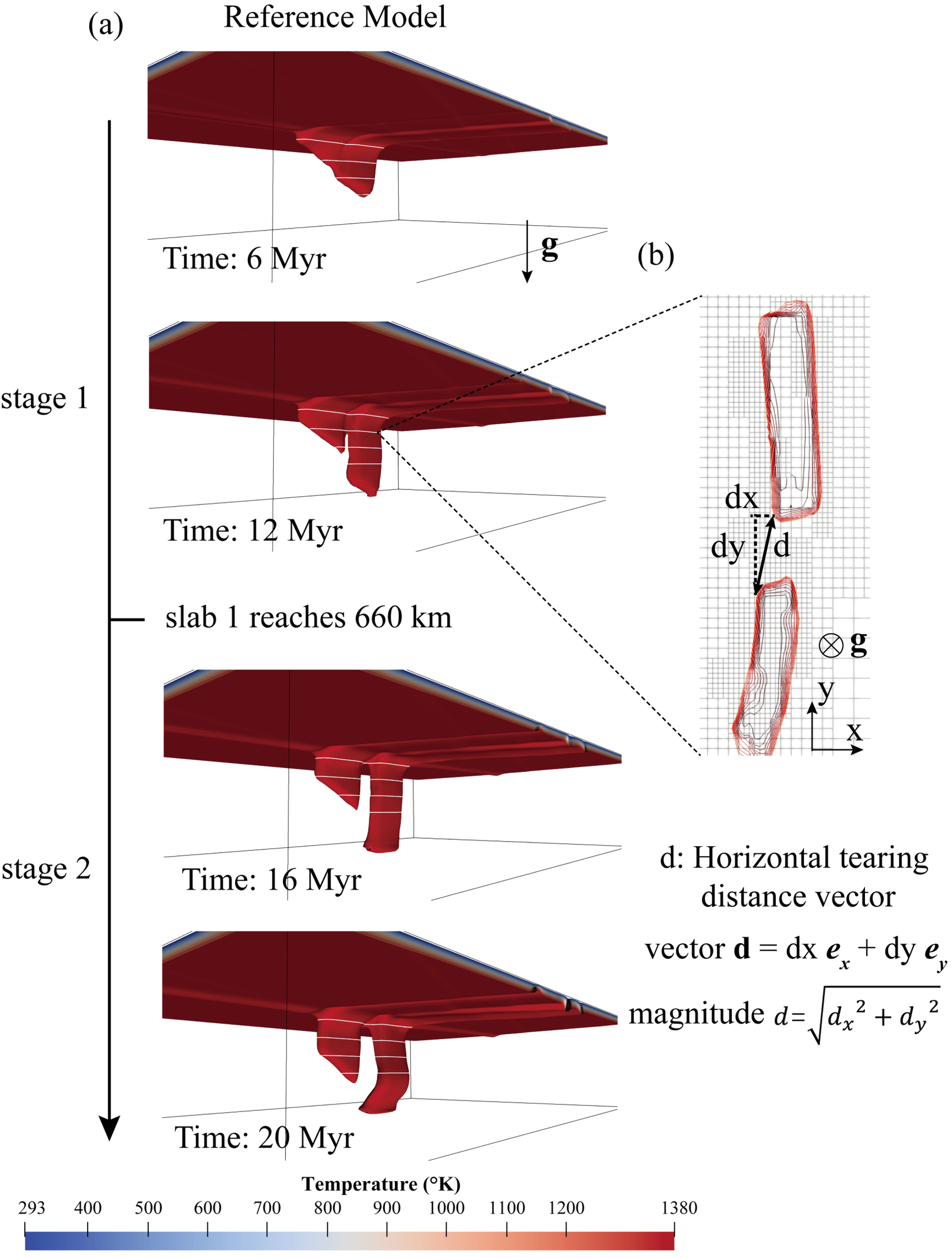
(a)
Reference Model
Time: 6 Myr
g
(b)
stage 1
Time: 12 Myr
dx
dy
d
slab 1 reaches 660 km
g
y
x
stage 2
Time: 16 Myr
d: Horizontal tearing distance vector
vector d = dx e_x + dy e_y
magnitude $d = \sqrt{d_x^2 + d_y^2}$
Time: 20 Myr
Temperature (°K)
293 400 500 600 700 800 900 1000 1100 1200 1380

Figure 4.

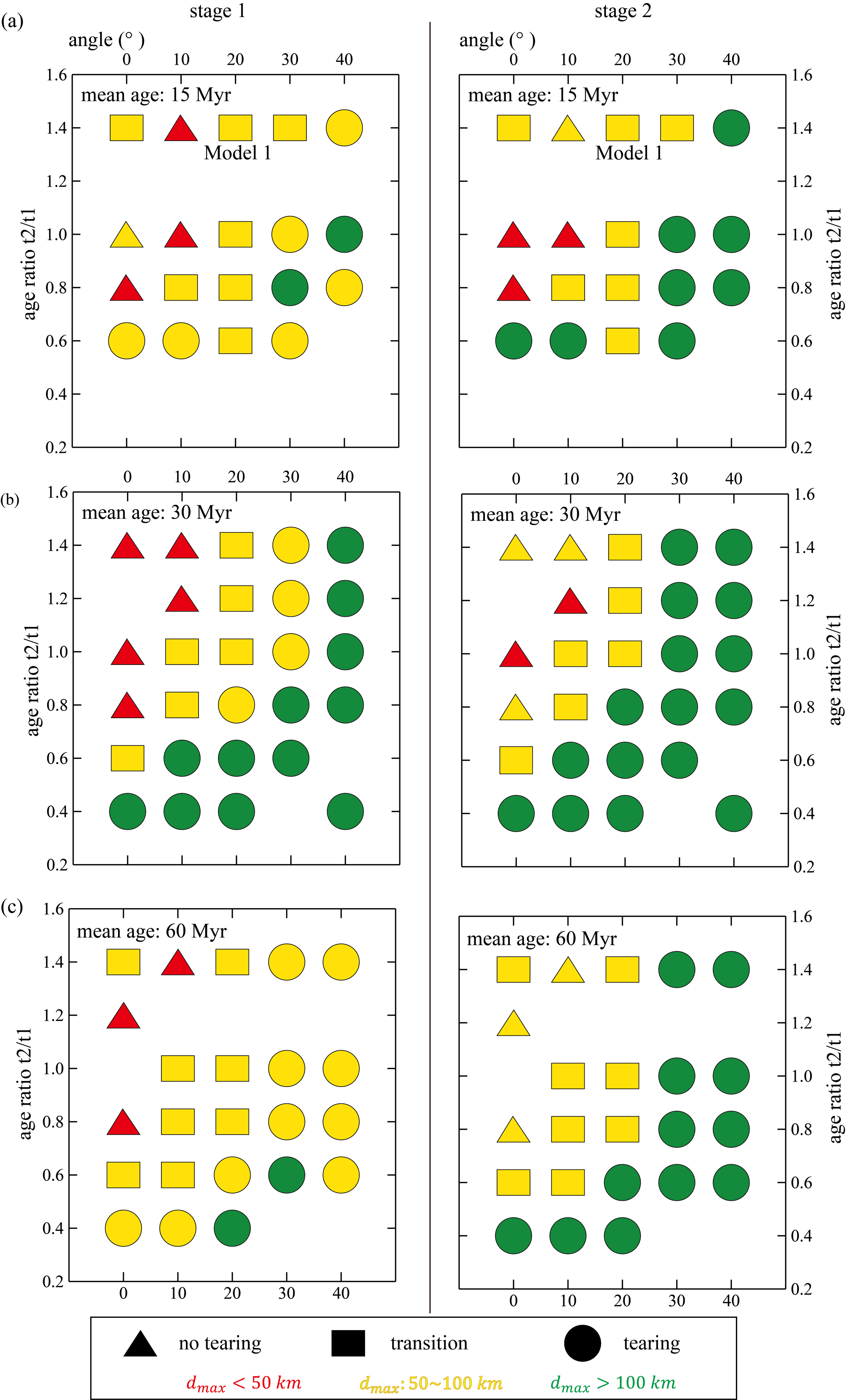
(a)
stage 1
stage 2
angle (°)
0
10
20
30
40
mean age: 15 Myr
Model 1
age ratio t2/t1
1.6
1.4
1.2
1.0
0.8
0.6
0.4
0.2
(b)
mean age: 30 Myr
(c)
mean age: 60 Myr
no tearing
transition
tearing
$d_{max} < 50\ km$
d_{max}: 50~100 km
$d_{max} > 100\ km$

Figure 5.

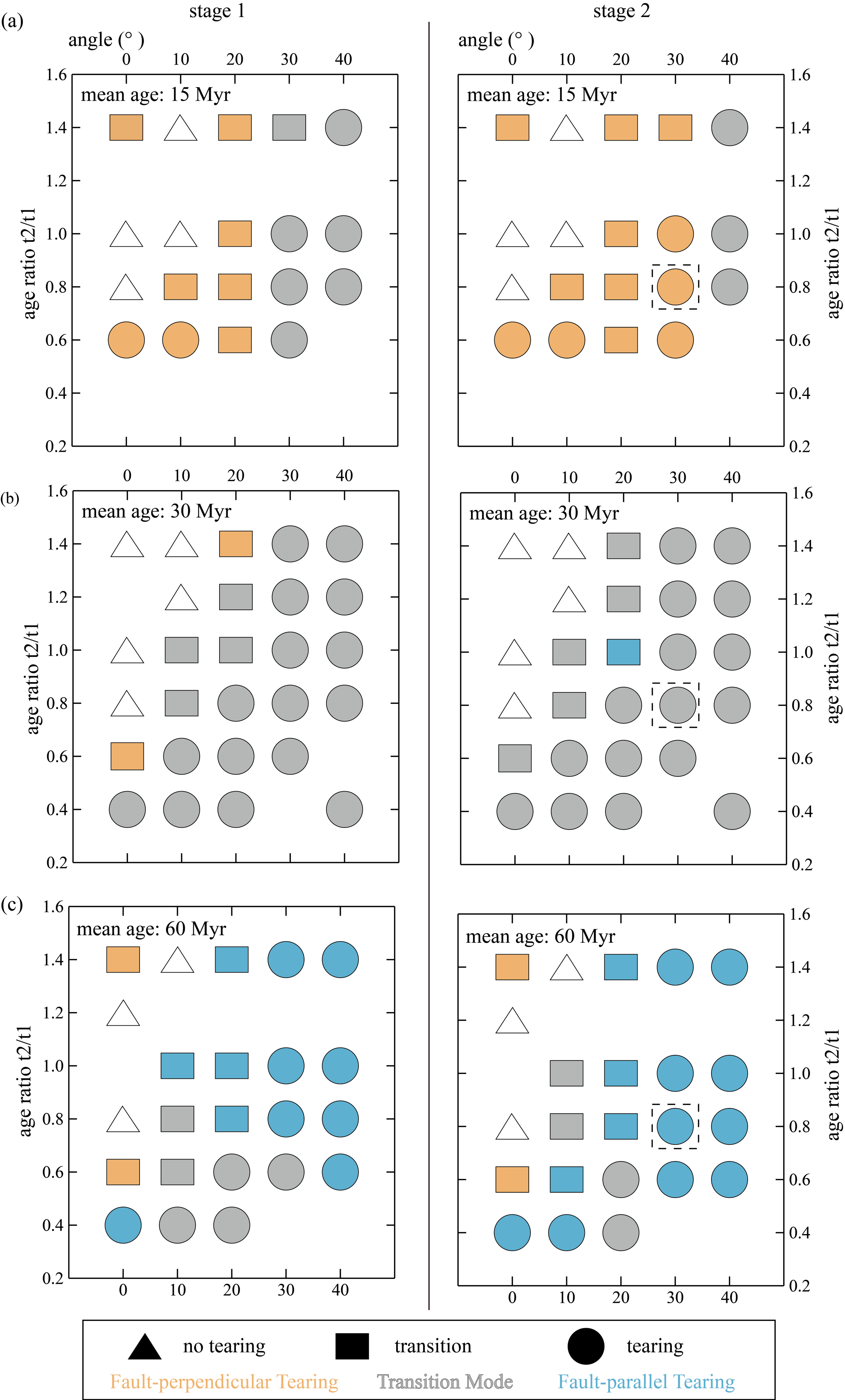
(a)
stage 1
stage 2
angle (°)
0
10
20
30
40
mean age: 15 Myr
(b)
mean age: 30 Myr
(c)
mean age: 60 Myr
age ratio t2/t1
0.2
0.4
0.6
0.8
1.0
1.2
1.4
1.6
no tearing
transition
tearing
Fault-perpendicular Tearing
Transition Mode
Fault-parallel Tearing

Figure 6.

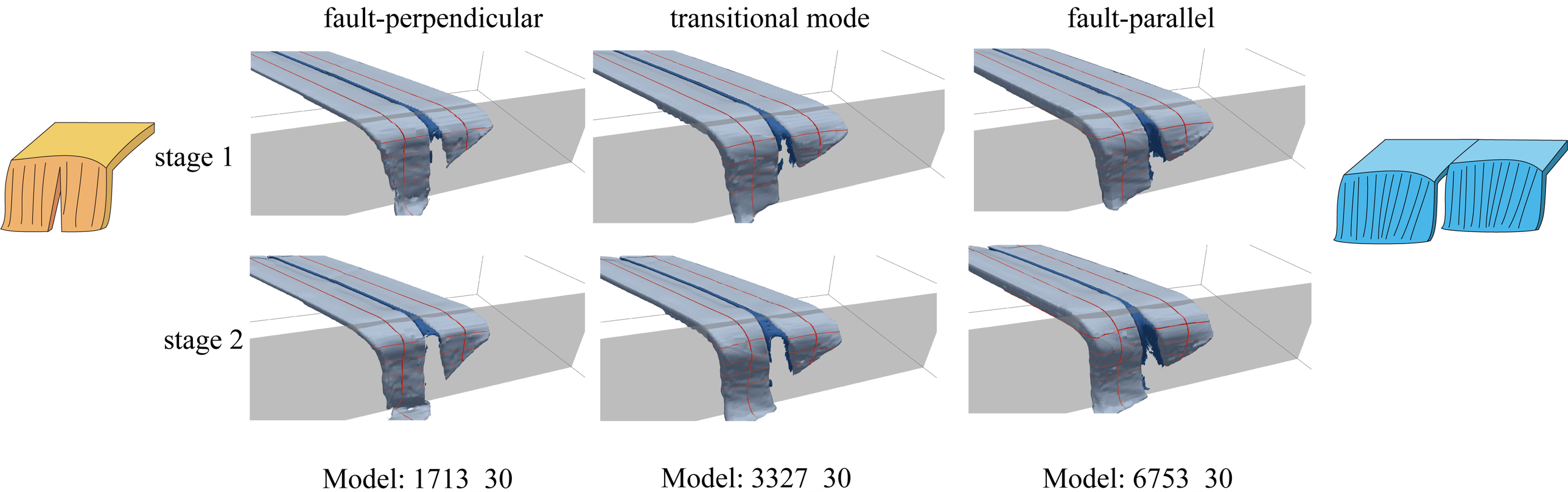
fault-perpendicular
transitional mode
fault-parallel
stage 1
stage 2
Model: 1713_30
Model: 3327_30
Model: 6753_30

Figure 7.

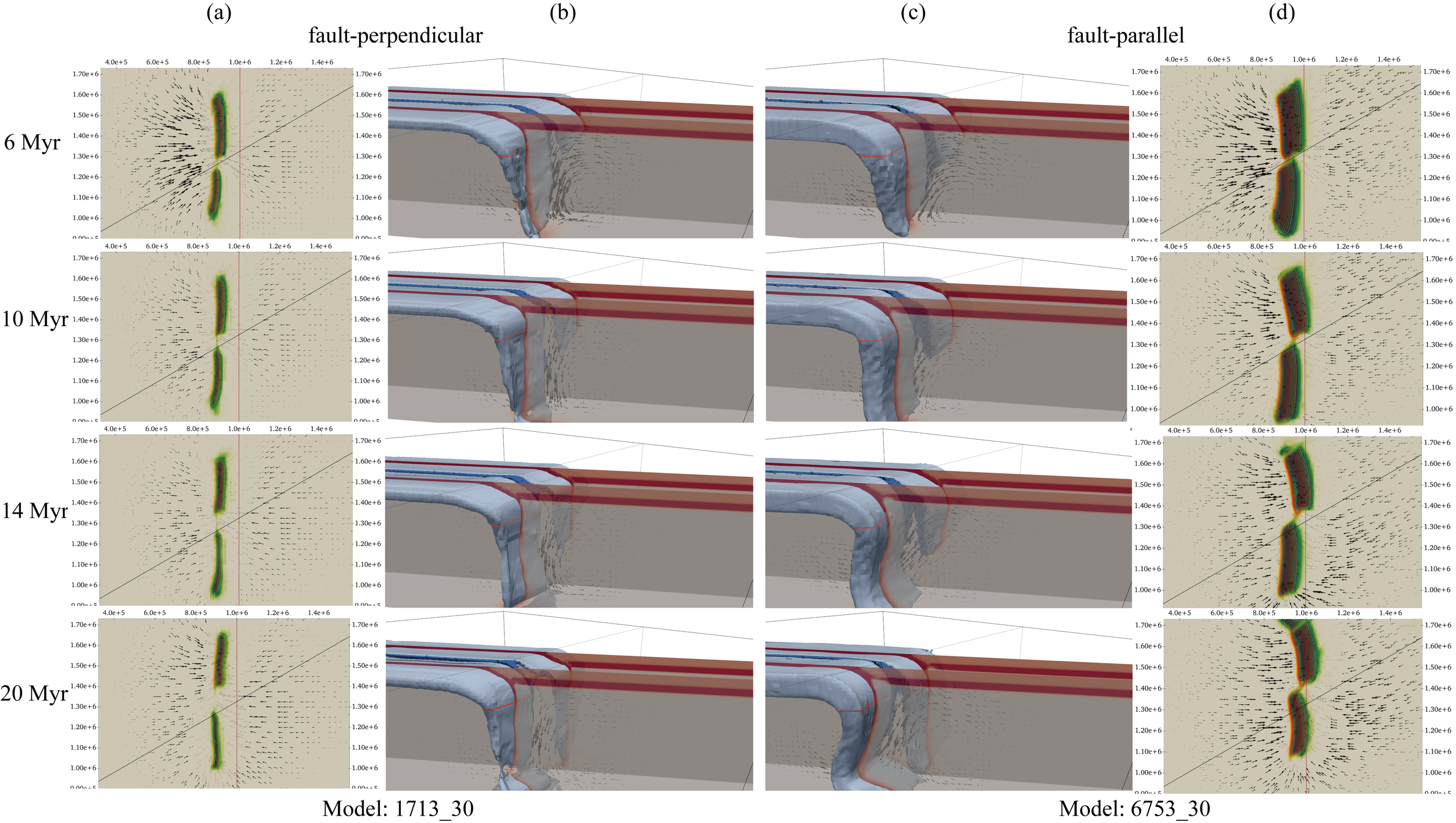
(a)
(b)
(c)
(d)
fault-perpendicular
fault-parallel
6 Myr
10 Myr
14 Myr
20 Myr
Model: 1713_30
Model: 6753_30

Figure 8.

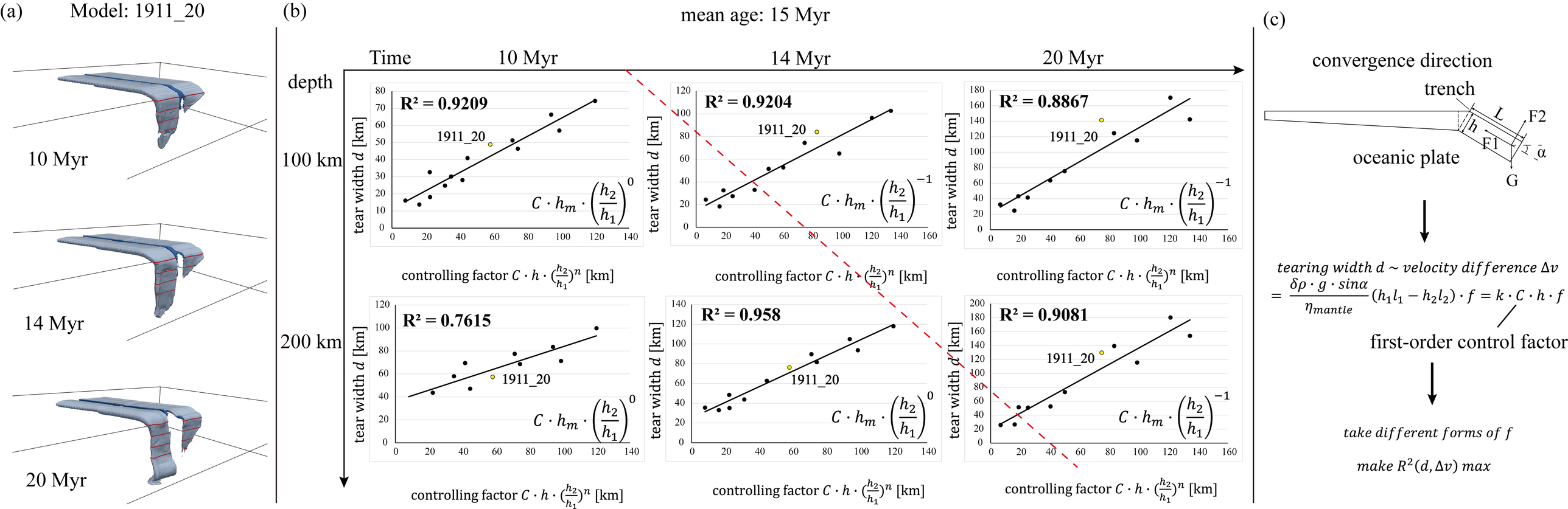
(a)
Model: 1911_20
10 Myr
14 Myr
20 Myr
(b)
mean age: 15 Myr
Time
10 Myr
14 Myr
20 Myr
depth
100 km
200 km
R² = 0.9209
R² = 0.9204
R² = 0.8867
R² = 0.7615
R² = 0.958
R² = 0.9081
1911_20
tear width d [km]
controlling factor $C \cdot h \cdot (\frac{h_2}{h_1})^n$ [km]
$C \cdot h_m \cdot \left(\frac{h_2}{h_1}\right)^0$
$C \cdot h_m \cdot \left(\frac{h_2}{h_1}\right)^{-1}$
(c)
convergence direction
trench
L
h
F2
F1
α
oceanic plate
G
tearing width d ~ velocity difference Δv
$= \frac{\delta\rho \cdot g \cdot \sin\alpha}{\eta_{mantle}}(h_1 l_1 - h_2 l_2) \cdot f = k \cdot C \cdot h \cdot f$
first-order control factor
take different forms of f
make $R^2(d, \Delta v)$ max

Figure 9.

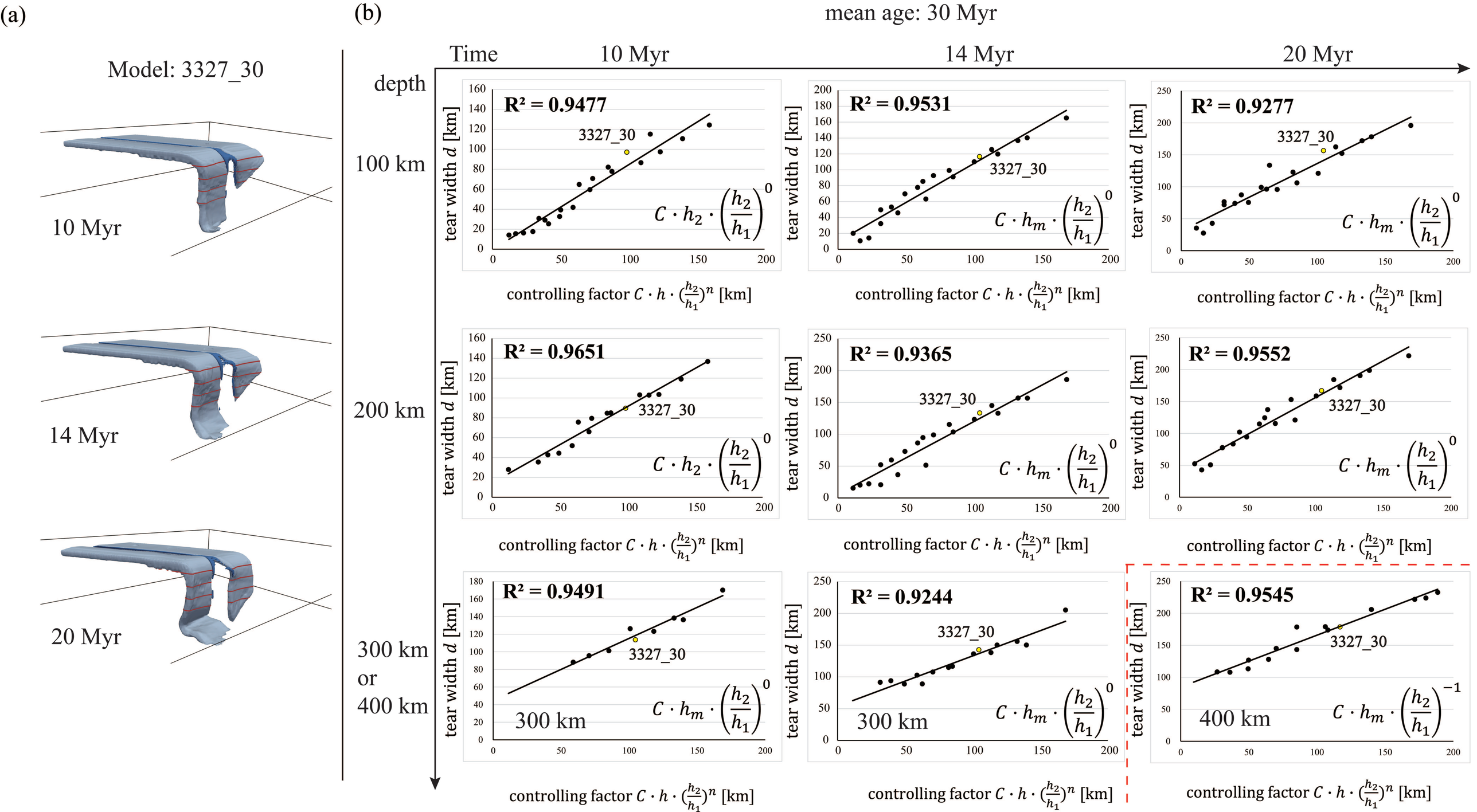
(a)
Model: 3327_30
10 Myr
14 Myr
20 Myr
(b)
mean age: 30 Myr
Time
10 Myr
14 Myr
20 Myr
depth
100 km
200 km
300 km
or
400 km
R² = 0.9477
R² = 0.9531
R² = 0.9277
R² = 0.9651
R² = 0.9365
R² = 0.9552
R² = 0.9491
R² = 0.9244
R² = 0.9545
3327_30
300 km
400 km
tear width d [km]
controlling factor C · h · (h2/h1)^n [km]

Figure 10.

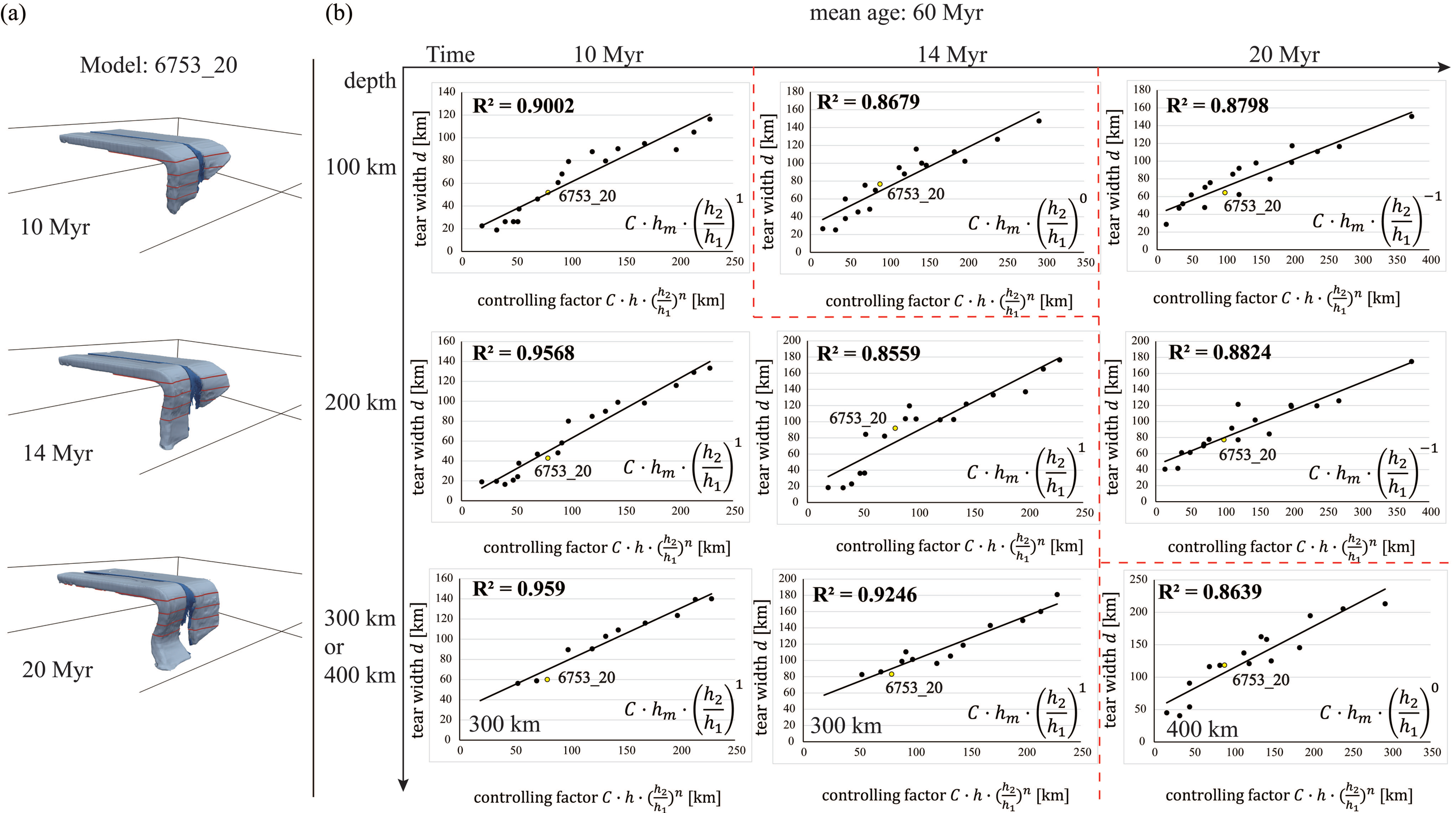
(a)
Model: 6753_20
10 Myr
14 Myr
20 Myr
(b)
mean age: 60 Myr
Time
10 Myr
14 Myr
20 Myr
depth
100 km
200 km
300 km
or
400 km
R² = 0.9002
R² = 0.8679
R² = 0.8798
R² = 0.9568
R² = 0.8559
R² = 0.8824
R² = 0.959
R² = 0.9246
R² = 0.8639
6753_20
300 km
400 km
tear width d [km]
controlling factor C · h · (h2/h1)^n [km]

Figure 11.

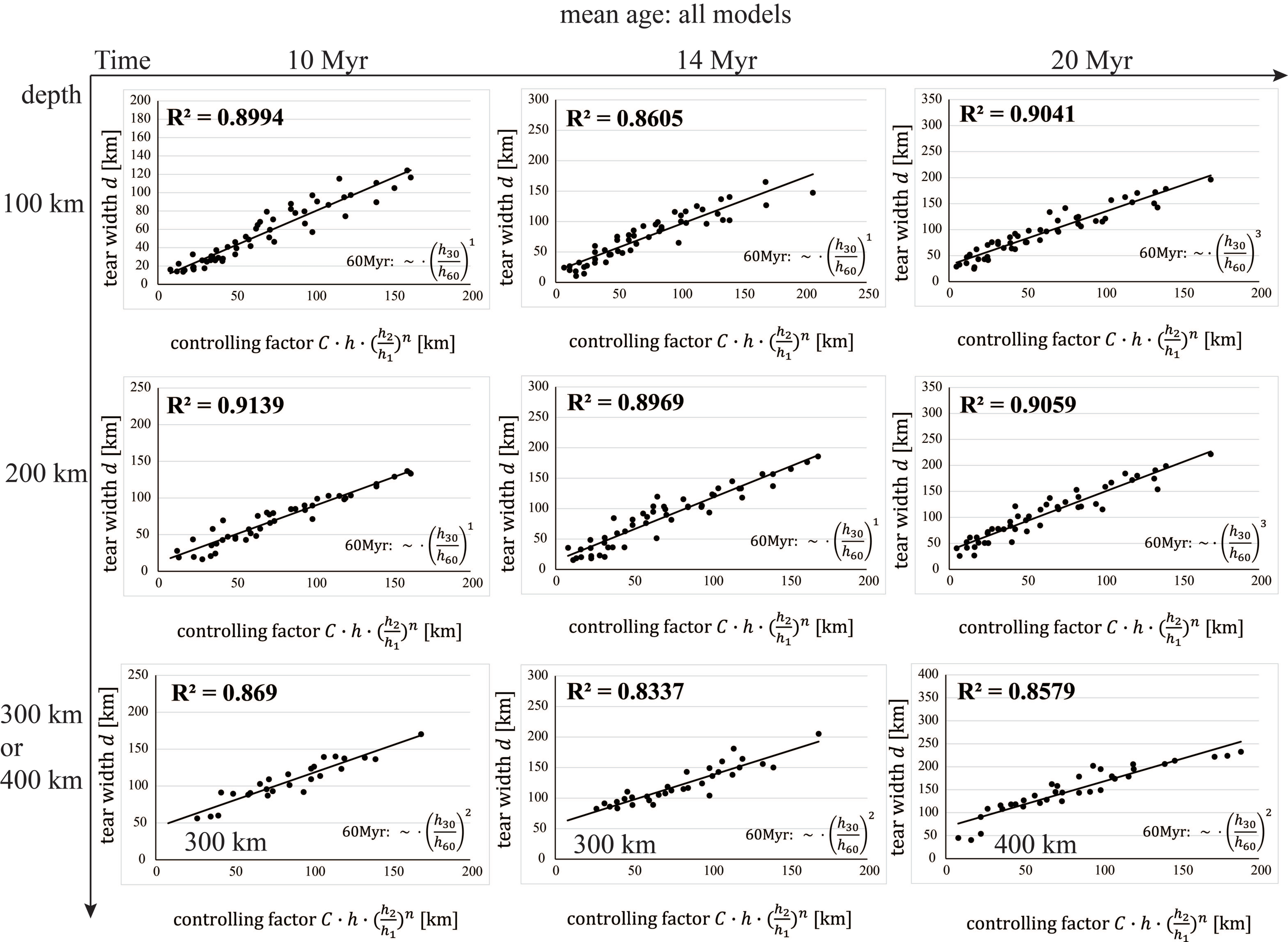
mean age: all models
Time
10 Myr
14 Myr
20 Myr
depth
100 km
200 km
300 km
or
400 km
R² = 0.8994
R² = 0.8605
R² = 0.9041
R² = 0.9139
R² = 0.8969
R² = 0.9059
R² = 0.869
R² = 0.8337
R² = 0.8579
300 km
400 km
tear width d [km]
controlling factor $C \cdot h \cdot (\frac{h_2}{h_1})^n$ [km]
60Myr: $\sim \cdot \left(\frac{h_{30}}{h_{60}}\right)^1$
60Myr: $\sim \cdot \left(\frac{h_{30}}{h_{60}}\right)^3$
60Myr: $\sim \cdot \left(\frac{h_{30}}{h_{60}}\right)^2$

Figure 12.

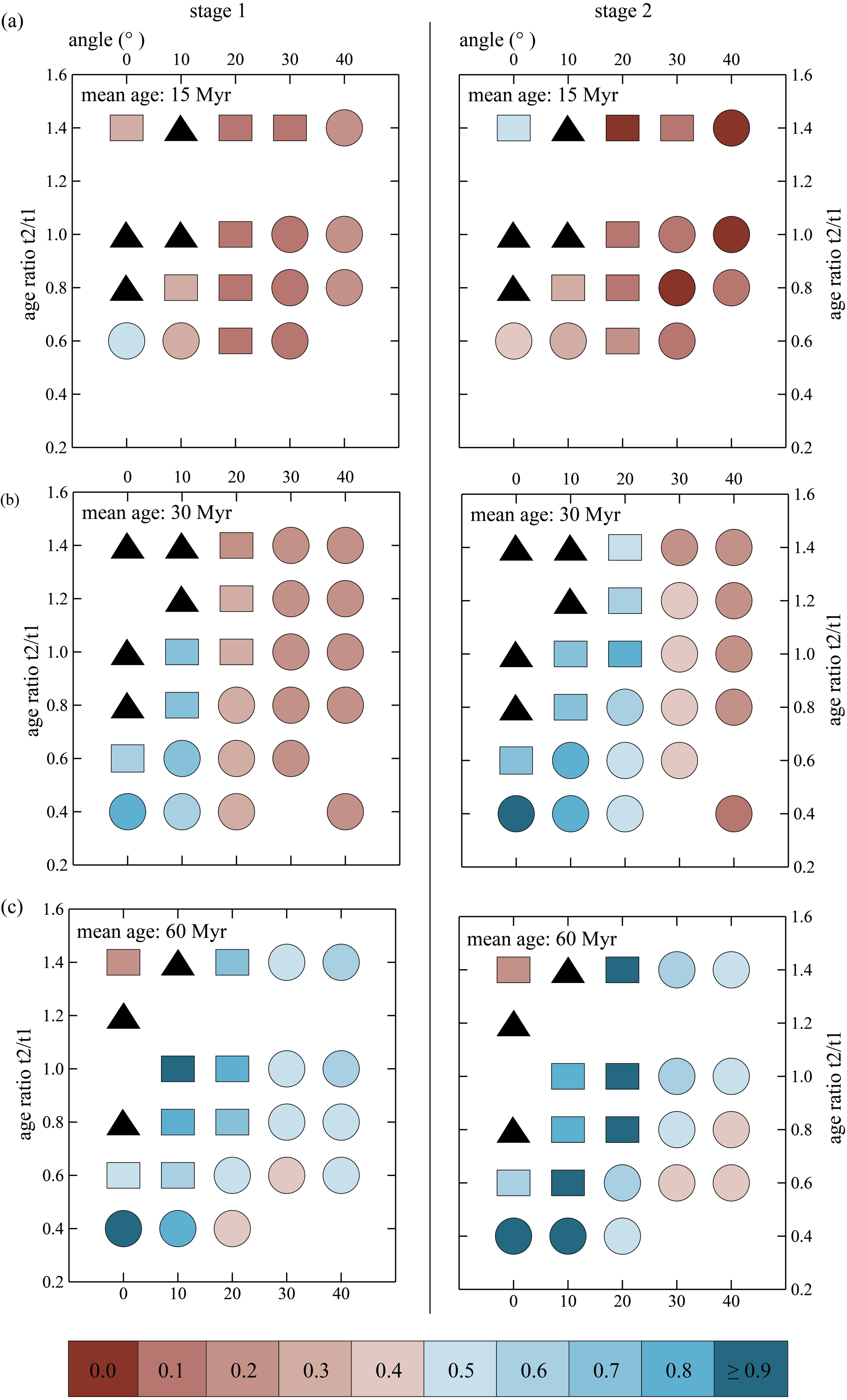
(a)
stage 1
stage 2
angle (°)
0
10
20
30
40
mean age: 15 Myr
(b)
mean age: 30 Myr
(c)
mean age: 60 Myr
age ratio t2/t1
1.6
1.4
1.2
1.0
0.8
0.6
0.4
0.2
0.0
0.1
0.2
0.3
0.4
0.5
0.6
0.7
0.8
≥ 0.9
trench-based tearing pattern (|dx/dy|)
x: trench-perpendicular, y: trench-parallel

Figure 13.

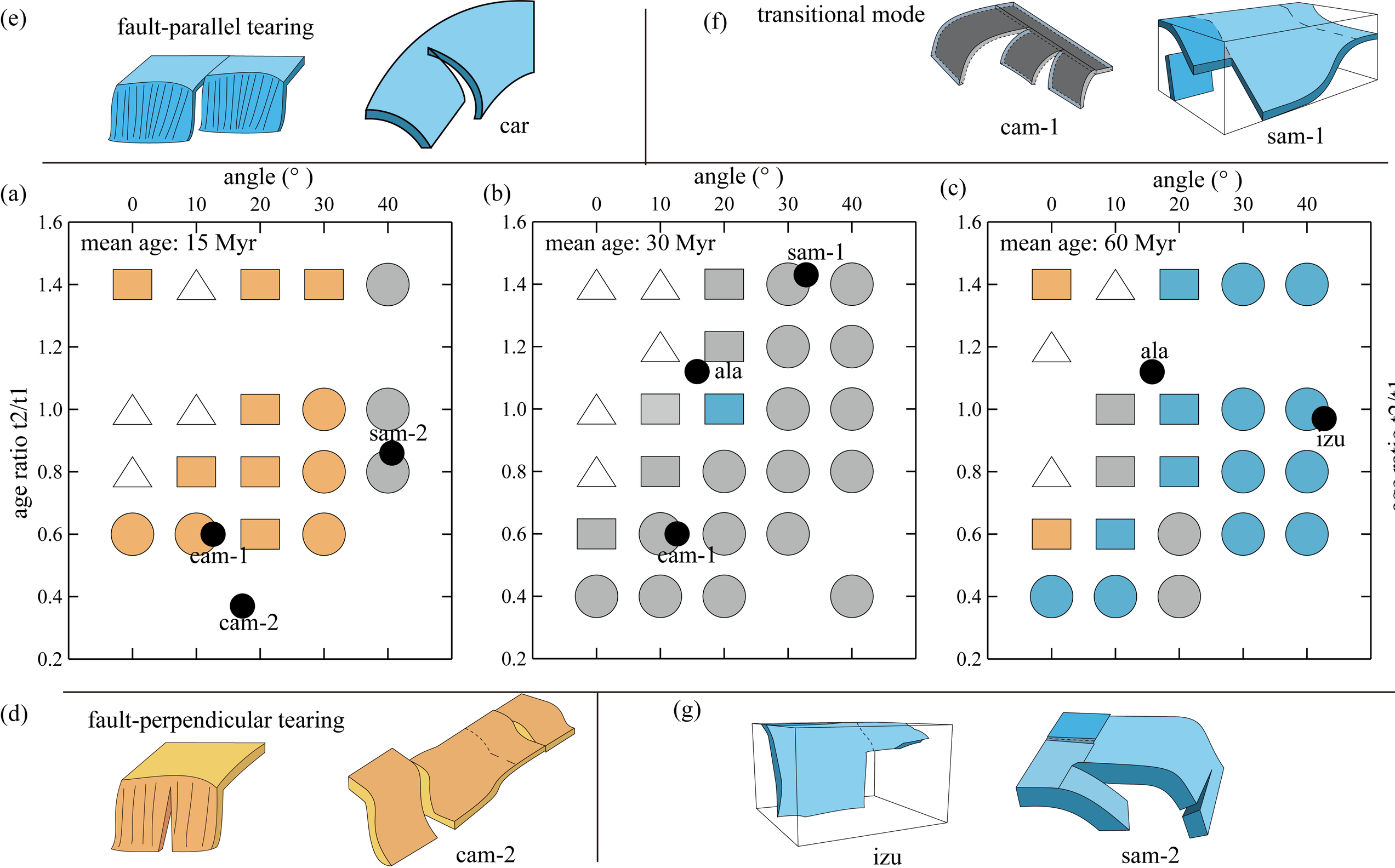
(e)
fault-parallel tearing
car
(f)
transitional mode
cam-1
sam-1
(a)
angle (°)
0
10
20
30
40
mean age: 15 Myr
sam-2
cam-1
cam-2
(b)
mean age: 30 Myr
sam-1
ala
cam-1
(c)
mean age: 60 Myr
ala
izu
age ratio t2/t1
1.6
1.4
1.2
1.0
0.8
0.6
0.4
0.2
(d)
fault-perpendicular tearing
cam-2
(g)
izu
sam-2

Dynamics of oceanic slab tearing during transform-fault horizontally-oblique subduction: Insights from 3D numerical modeling

Jie Xin[1], Huai Zhang[1,4,5,*], Felipe Orellana-Rovirosa[2], Zhong-Hai Li[1], Liang Liu[3], Yi-Gang Xu[3], Zhen Zhang[1], Yaolin Shi[1]

[1]Key Laboratory of Computational Geodynamics, College of Earth and Planetary Sciences, University of Chinese Academy of Sciences, Beijing 100049, China

[2]Department of Ocean Science and Engineering, Southern University of Science and Technology, Shenzhen 518055, China

[3]State Key Laboratory of Isotope Geochemistry, Guangzhou Institute of Geochemistry, Chinese Academy of Sciences, Guangzhou 510640, China

[4]Beijing Yanshan Earth Critical Zone National Research Station, University of Chinese Academy of Sciences, Beijing 101408, China

[5]Southern Marine Science and Engineering Guangdong Laboratory (Zhuhai), Guangdong Zhuhai 519080, China

Key Points:

- 3-D numerical models are conducted to study the vertical tearing mechanism of the transform-faulted oceanic slabs during oblique subduction.
- The horizontal obliqueness and slab transform age difference play dominant roles in determining the style of vertical slab tearing.
- Correlations between slabs' computed tearing width and scaling-theory forms of subduction-velocity difference, are useful and strong.

Abstract

Oceanic-plates vertical tearing is seismically-identified in the present-day Earth. This type of plate tearing is frequently reported in horizontally-oblique subduction zones where transform-faulted oceanic plates are subducting (or subducted). However, the mechanisms behind vertical slab tearing are still poorly understood, thus we utilize 3D time-dependent Stokes' flow thermo-mechanical models to further study this problem. We find that (i) the age offset of transform fault and (ii) the horizontal obliqueness of subduction fundamentally control the tearing behavior of two generic, materially-homogeneous oceanic slabs separated by a low-viscosity zone. The overriding-continental plate bends one slab first, which combined with the age-thickness difference between slabs, causes the differential sinking of them. Based on the modeling results, well-developed slabs vertical tearing would happen when the oblique angle of subduction is ⩾30° or the age ratio of the secondly-bent to firstly-bent slab being ~<0.6. Quantifying the horizontal distance-vector between sinking slabs, we find that subduction at medium-low horizontal-obliqueness angles (≤30°) of young lithosphere (slabs-average ~15 Myr) tends to produce fault-perpendicular tearing. Contrastingly, old-age slabs (average ≥ 30 Myr) with medium-large obliqueness angles (~>20°) tend to produce fault-parallel tearing, related to differential slab-hinge retreat or rollback. Correlations between slabs' (i) computed tearing horizontal-width and (ii) scaling-theory forms of their subduction-velocity differences, are reasonable (0.76-0.97). Our numerically-predicted scenarios are reasonably consistent with plate-tear imaging results from at least 4 natural subduction zones. Our modeling also suggests that continual along-trench variation in subduction dip angle may be related to a special case of oblique subduction.

Keywords: Oceanic slabs vertical tearing, horizontally-oblique subduction, transform-fault offset, 3D numerical models, Stokes' flow.

Plain Language Summary

Oceanic tectonic plates can tear-off through time as they plunge and sink into the Earth's mantle and are especially favored when plates have preexisting fault-weak zones. Two primary conditions promote oceanic tectonic slabs' tearing: (1) Obliqueness of a plate's horizontal velocity with respect to the overriding-plate coastline and trench, as the latter will enforce bending of one side of the slab first causing differences in deformation; (2) Differences in slab-age between two sides of a displaced fault-zone that created an offset in plate age and thickness. To understand these processes, we present 3D numerical models that simulate tectonic evolution and deformations, and we compare model results with analytical studies as well as with natural observations from seismic imaging. Age differences across fault-zones combined with subduction horizontal obliqueness control the generation and development of vertical tearing. Furthermore, two geometrical patterns of vertical tearing are largely consistent with observations. Our findings suggest that along-trench changes in the steep angle between the slab and surface (dip angle) may be related to the early stages of oblique subduction. Observing the age contrast across faults and the horizontal obliqueness of plates' motion allows predictions of the tearing pattern, evolution, and local mantle flow.

1. Introduction

Oceanic lithosphere tearing (or break-off) is a general phenomenon on present-day Earth. When occurring, the resulting slab window allows hot mantle materials to pass through, resulting in anomalous thermal and chemical conditions in convergent-margin environments (Gianni & Luján, 2021; Thorkelson, 1996). If slab tearing occurs at shallow depths (Freeburn et al., 2017; Király et al., 2020), the asthenospheric upwelling causes significant geological and geophysical responses, including complex mantle flow in subduction zones (Bolton et al., 2022; R. Govers & Wortel, 2005; Rosenbaum et al., 2008), anomalous thermal and mechanical structures of the overlying plate (Georgieva et al., 2016; Guillaume et al., 2010; Jolivet et al., 2015; Roche et al., 2018), as well as active arc and back-arc magmatism (Gianni & Luján, 2021; K. Liu et al., 2020; Xu et al., 2020).

Plate tearing can be categorized into horizontal and vertical tearing patterns (Rosenbaum et al., 2008). The horizontal tearing normally occurs along a sub-horizontal plane, in which the lower segment of the slab detaches from the upper and then sinks into the mantle. In this case, the negative buoyancy of the subducted slab contributes to the slab break-off (tearing) process (Duretz et al., 2011; Gerya, 2022; Hildebrand et al., 2018; Kufner et al., 2017; L. Liu et al., 2021). On the other hand, it is generally considered difficult for a coherent subducting slab to tear along sub-vertical planes perpendicular to the trench (Cui & Li, 2022) due to the lack of major force gradients in the along-strike direction. However, according to studies of seismic tomography, vertical slab tearing (sub-vertically-oriented anelastic (brittle-visco-plastic) tears, that may be propagating in the subducted-subducting portions of oceanic slabs) seems to have developed in many subduction zones of present-day Earth (Figure 1), including the Mariana's subduction zone (M. S. Miller et al., 2004; Meghan S. Miller et al., 2006), the Calabria subduction zone (Jolivet et al., 2021; Suckale et al., 2009), the Aegean and Anatolia regions (Rob Govers & Fichtner, 2016; Jolivet et al., 2015), the Central America subduction zone (Carciumaru et al., 2020; Dougherty & Clayton, 2014; Stubailo et al., 2012; Thorkelson, 1996), the South American subduction zone (Pesicek et al., 2012; Rosenbaum et al., 2008; Vargas & Mann, 2013), the Caribbean

subduction zone (Meighan et al., 2013), and the Kamchatka subduction zone (Levin et al., 2002).

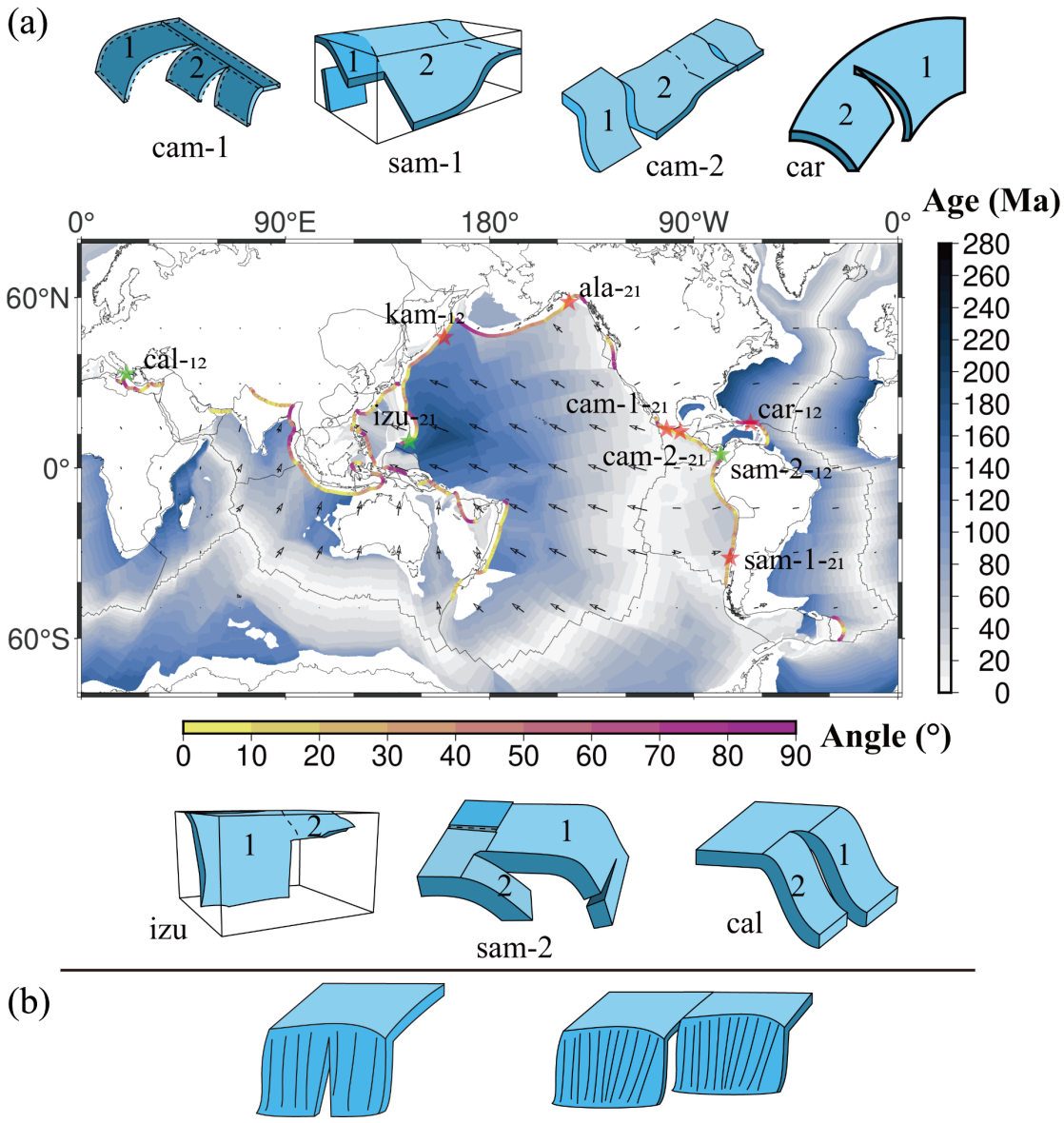

Figure 1. Global distribution of vertical plate tearing in the present-day oceanic subduction zones. (a) The stars on the map and the cartoons above or below show each case's position and deep structure. Red stars represent tearing involving transform-fault subduction, and green stars involve other factors (e.g., ocean-continent transform zone, ridge subduction). The cartoons are shown for '**ala**' and '**kam**' due to the lack of relevant data. The references for these subduction zones are: Central America (**cam-2**): Carciumaru et al., 2020; Dougherty and Clayton, 2014; Kamchatka (**kam**): Levin et al., 2002; Caribbean (**car**): Meighan et al., 2013; Izu-Bonin (**izu**): Miller et al., 2006; South America (**sam-1**): Pesicek et al., 2012; Central America (**cam-1**): Stubailo et al., 2012; Calabria (**cal**): Suckale et al., 2009; South America (**sam-2**): Vargas and Mann, 2013; Alaska (**ala**): Yang and Gao, 2020. The identifications of slab-1 and slab-2 are defined as follows: slab-1 is the slab that would arrive and contact the

trench earlier, whereas slab-2 would do it later. The vertical color bar represents the age of the oceanic lithosphere, and the horizontal color bar is the magnitude of the angle between horizontal plate velocity and the direction perpendicular to the trench. The angle sign is coded-indicated by the numbers after the second hyphen, the first number corresponds to the left-side slab when standing above the subduction zone and looking toward the continent, and the second indicates the right-side slab. The arrows indicate the plate velocity in the hot spot reference frame (Becker et al., 2015). The data on the subduction zone, seafloor age, and color bar are referred to (Hayes et al., 2018), (Müller et al., 2008), and (Crameri, 2021), respectively. (b) Cartoons illustrate the two typical slab vertical tearing patterns (Rosenbaum et al., 2008).

Slab quasi-vertically-oriented tears (and frequently sub-vertically propagating) within the mantle generally require along-strike physical variations (such as gradients in morphology, forces, material properties, etc.), with several mechanisms being proposed: non-uniform rollback due to lateral temperature and age differences in subducting plates or step faulting at the edges of active margins (Burkett & Billen, 2010; R. Govers & Wortel, 2005), opposite rotation of slab segments (Gianni et al., 2019), oceanic/continental plate transition along-trench (Li et al., 2013; Magni et al., 2014; Pusok et al., 2018), subduction of spreading ridges (Burkett & Billen, 2010), and perhaps finally, variable orientations of passive margins (Fernández-García et al., 2019). Therefore, various factors can affect the specific subduction mode, with slabs undergoing translation, rotation, and deformation during the sinking, with tearing being an extreme case of slab deformation involving topological changes. Due to this complexity, in this study, we would narrow our focus to the scenarios where the oblique subduction of transform-faulted slabs develops.

As proposed in previous studies, due to the contrasting seafloor ages (and mechanical properties) across a transform fault, the vertical tearing of transform-faulted oceanic plate likely happens (Burkett & Billen, 2010). In addition, we consider the horizontal obliqueness of the subduction direction with respect to the trench as playing a key role in combination with the transform-fault age contrasts.

In this study, by systematically conducting 3D time-dependent numerical modeling to investigate the effects of the two factors for vertical oceanic-plate tearing, we will summarize the key conditions for different observed patterns for vertical slab (Figure 1

and Table 1) tearing and use a scaling method to reveal the controlling variables behind them.

We hope this work will improve our understanding of these “abstract” systems, but also our understanding of real-Earth systems that comprise geological/physical ingredients of this kind; and to help us for example, when attempting to infer the pre-subduction obliqueness angle of a subducted plate that may lack hotspot-track constraints, and also to improve the accuracy of plate reconstructions.

Table 1. Parameters of the natural subduction zones with slab tearing [a].

Symbol (subduction zone)	Name of the fracture zone [b]	Oblique convergence angle	Age of Slab-1 (t_1, Ma)	Age of Slab-2 (t_2, Ma)
cam-1 (Central America)	Tehuantepec	12.6°	23.6	14.3
cam-2 (Central America)	Orozco	17.2°	12.7	4.7
sam-1 (South America)	Mocha	32.8°	24.6	35.3
sam-2 (South America)	——[b]	40.6°	12.7	10.9
Izu (Izu-Bonin)	——[b]	42.7°	156.0	150.8
cal (Calabria)	Kephalonia [b]	22.9°	247.2	245.3
car (Caribbean)	——	70.2°	88.7	115.4
ala (Alaska)	Between the Pacific plate and the Yakutat plate	15.8°	34.0	38.2
kam (Kamchatka-Kuril)	——	22.7°	111.9	110.2

[a] The slabs convergence angle and lithospheric ages use the averaged values within 300 km of both sides of the corresponding symbol sites on the map (Figure 1). [b] Other types of subduction tectonic environments are distinguished by green stars (Figure 1), e.g., ocean-continent transform zone, ridge subduction.

2. Model setup

We use the finite-element software ASPECT (version 2.3.0) to solve the incompressible Stokes' viscous flow equations (1-2) coupled with thermal advection-diffusion equation (3) velocity $\boldsymbol{u}$, pressure p, temperature T (Bangerth et al., 2021; Glerum et al., 2018). Equation (4) describes the evolution of additional (compositional) fields transported along with the velocity field $\boldsymbol{u}$, without diffusion. For the Stokes' flow equation, we employ the Taylor-Hood spatial element.

$$-\nabla \cdot \left[2\eta\left(\varepsilon(\boldsymbol{u})\right)\right] + \nabla p = \rho \boldsymbol{g} \tag{1}$$

$$\nabla \cdot \boldsymbol{u} = 0 \tag{2}$$

$$\rho C_p \left(\frac{\partial T}{\partial t} + \boldsymbol{u} \cdot \nabla T\right) - \nabla \cdot k \nabla T = 0 \tag{3}$$

$$\frac{\partial c_i}{\partial t} + \boldsymbol{u} \cdot \nabla c_i = 0 \tag{4}$$

where c_i is the i-th compositional field that defines and tracks subsets of distinct chemical compositions and properties, $\varepsilon(u) = \frac{1}{2}(\nabla u + \nabla u^T)$ is the linear strain rate, η, ρ, C_p and k are the fluid's shear viscosity, mass-density, specific isobaric heat capacity and thermal conductivity, respectively; and **g** is the gravitational acceleration.

A 3D Cartesian model box with spatial dimensions of 2500 km×3000 km×660 km is used. Figure 2 shows the initial model configuration demonstrated in composition, including a partially-subducted oceanic lithosphere: two slabs separated by a weak transform fault-zone in the middle, a continental lithosphere as the overriding plate, and two side plates (Figure 2a). Although these denominations may conflict with previous studies, this will be, for the sake of cleanliness, our formal language-terminology from this point onward in this article: our model has one single oceanic plate or lithosphere, separated in two slabs by the transform-fault zone.

The width of the weak transform fault-zone is 30 km, and its thickness is consistent with that of the thicker lithosphere on both sides. A low-viscosity oceanic crust defines the uppermost part of the subducting lithosphere (slabs), and act as a weak contact zone with the overriding continental plate. The initial vertical dip angle of the subducting slabs is fixed at 30°. The subducting oceanic plate is decoupled from the side plates by

applying two side faults, as shown in Figure 2b. In contrast to the central plate, which is 10 km from the left boundary and undergoes free subduction, no subducting slab is prescribed for the side plates (Figure 2d).

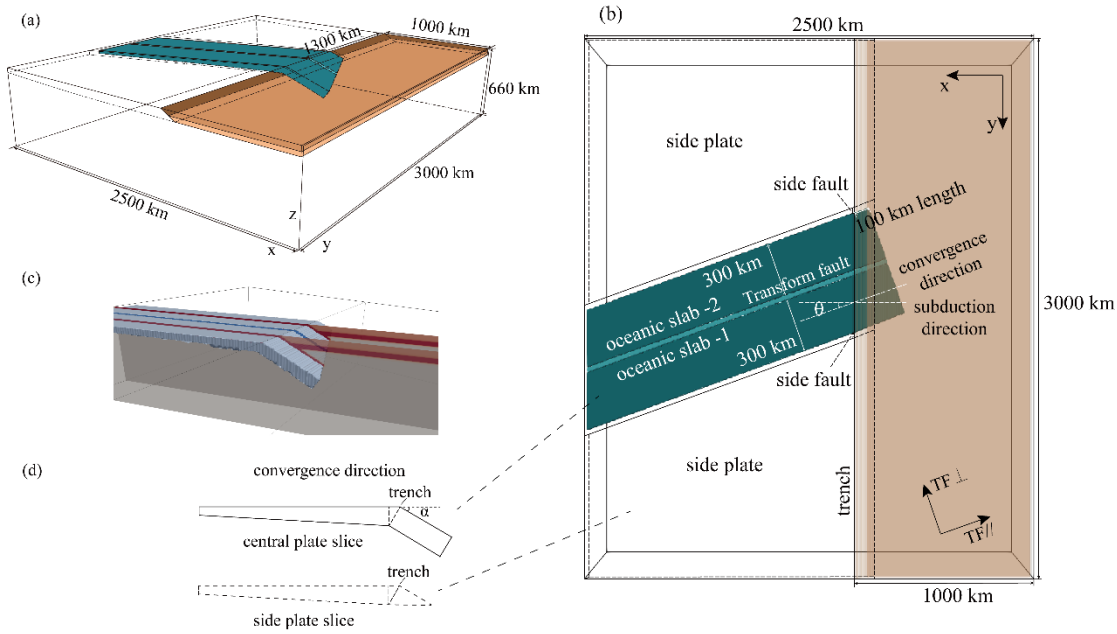

Figure 2. Initial condition model setup. (a) 3D oblique view of the model structure with the subducting (cyan) and overriding (brown) plates. (b) View from above. The oceanic lithosphere's weak central region (transform fault zone) is 30 km wide and separates the plate in two distinct slabs. The two fundamental coordinate systems are shown, with trench -perpendicular (X) and -parallel (Y) axes, and transform-fault -parallel (TF//) and -perpendicular (TF ⊥) axes. (c) The initial composition of the oceanic lithosphere (blue) and vertical slices of density (red). (d) The vertical cross-sections on the lateral edges of subducting lithosphere and adjacent plate slice lithosphere. The initial dip angle of the subducting slab is α =30° (vertical angle, same value for all the models). The horizontal angle θ parameterizes the horizontally-oblique subduction. The length of the shortest subducted slab segment is 100 km (in slab-2) and increases gradually to the other side (slab-1).

The half-space cooling model is used to calculate the oceanic plate's initial-condition thermal-age thickness as $h \approx 2.32\sqrt{\kappa t}$ ($h_{max} = 100km$) (Turcotte & Schubert, 2002), where k is thermal diffusivity, and t is seafloor age. In this sense, the thickness ratio between slabs 1 and 2, *i.e.*, h_1/h_2, is dynamically similar to the square root of the ratio of lithospheric ages $\sqrt{t_1/t_2}$. The ocean plate's initial (unsubducted) maximum thickness is limited to 100 km, consistent with thermo-rheological observations (Schubert et al.,

2001). The model-box's top and bottom boundary temperatures are fixed at 293 °K and 1775 °K (calculated using the mantle adiabatic thermal gradient), respectively.

Our representation assumes the oceanic-plate as a numerical compositional field, with two distinct variable-thickness domains, layers or slabs whose initial-condition upper and lower surfaces (and thicknesses) are defined by two isothermal surfaces of the half-space cooling model (whose maximum depth depends on the horizontal transform-fault-parallel coordinate as previously indicated). The slabs' density and viscosity are assumed to remain constant (this is a major simplification: these model-variables do not depend on pressure, temperature, or strain rate) with well-established values (Table 2), thermal expansion coefficient is assumed null and thermal conductivity is fixed. This simplification is only a first-order approximation which allows faster computations. In the mantle domain, an adiabatic temperature profile is applied as initial condition.

Our model slabs can change their thickness as they evolve in time, but solely by virtue of divergence-free flow advection and deformation (they can thicken/thin if their perpendicular area decreases/increases), a dynamical consequence of 3D-time-dependent velocity field. The thermal field spatio-temporally evolves and its coldest regions fairly approximate the compositional slabs (especially at early times given slow-enough thermal diffusion), and this provides additional supporting information on the system (later on used in two of our figures).

The velocity field boundary conditions (at all times) are of tangential flow boundary, i.e. free-slip (zero shear stress) and no-flow-through (zero normal velocity), on all the model-box surface boundaries except for that at the bottom: the lower boundary is fixed (3D zero velocity vector) and intended to simulate the effect of the 660 km phase-transition interface.

Finally, the computational grid is adaptively refined five times until its smaller cell reaches a minimum size of 6.51 km×6.25 km×6.88 km, and the coarsest cell size is 8 times larger. The maximum number of cells is ~3×10^5 and the number of unknowns is ~8×10^7. Usually, it takes 24 to 48 hours for each model, running with 220 computing

cores, to simulate a geological time of about 30 Myr.

Table 2. Material properties of the numerical models [a].

Compositional units	Density($kg \cdot m^{-3}$) [b]	Viscosity(Pa·s)
Underlying upper mantle	3300	1.4×10^{20}
Oceanic crust	3390	2.8×10^{20}
Oceanic lithospheric mantle	3390	1.4×10^{23}
Continental crust	2800	1.4×10^{24}
Continental lithospheric mantle	3390	1.4×10^{23}
Transform-fault zone	3390	7.0×10^{20}
Side faults	3390	7.0×10^{20}
Crust of side plates	3350	2.8×10^{20}
Lithospheric mantle of side plates	3390	1.4×10^{23}

[a] Other parameter values: Reference temperature = 293 °K; heat capacity = 1250 J/kg/°K; thermal conductivity = 4 W/m/°K; thermal expansion coefficient = 0.

[b] The value of density implicitly includes the thermal-effect dependence.

3. Results

A total of 69 experiments/simulations are conducted with different relevant combinations of oceanic lithosphere's (i) horizontal-obliqueness angles and (ii) slabs age offset. To quantify the size of the tear width, we visualized and post-processed the output data in ParaView, specifically by selecting horizontal slices of the oceanic lithosphere at various times and depths and measuring the horizontal vector distance between the two slabs (Figure 3).

3.1. Tested conditions for vertical slab tearing

In our simulations, the slabs' tearing process can be separated, before and after, by the event of slab 1 reaching the 660 km depth (as mapped by the oceanic-lithosphere compositional field (in Aspect software) value >0.5 within 15 km from such depth). In particular, for our reference model (t_1=33 Myr, t_2=27 Myr, θ=20°; abbreviated as

3327_20), we show snapshots of its evolution in Figure 3a by isolating temperatures ≤1380 °K, so the sinking slabs appear bounded by isothermal surfaces (with the hotter ambient mantle made invisible).

Using ASPECT-software compositional fields, for all the simulations, we isolate the slabs from the embedding ambient mantle (as for the reference simulation in Figure 3b), and then we measure the tear horizontal-widths at different depths in both time-stages (as in Figure 3b).

As can be seen from the white contour lines (depths: 100-200-300-400 km) in Figure 3a, vertical tearing can occur at deep locations (>200 km depth). As the subduction progresses, the finite-width tear gradually (after 12 Myr) expands and vertically-propagates to the shallow part (~100 km). After slab 1's tip arrives at the box bottom, its sinking velocity decreases, contributing to the increase in tearing width (Figure 3) at intermediate depths. After identifying the 660 km-depth contact event of slab 1, we select two sampling times: 2 Myr before and 2 Myr after the event. At each one of those times, we take the maximum value of tearing width d_{max} over the different depths for the subsequent determination of the tearing conditions (as in Figure 3b). Figure 4 displays the tearing judgments/decision array of the full set of numerical experiments.

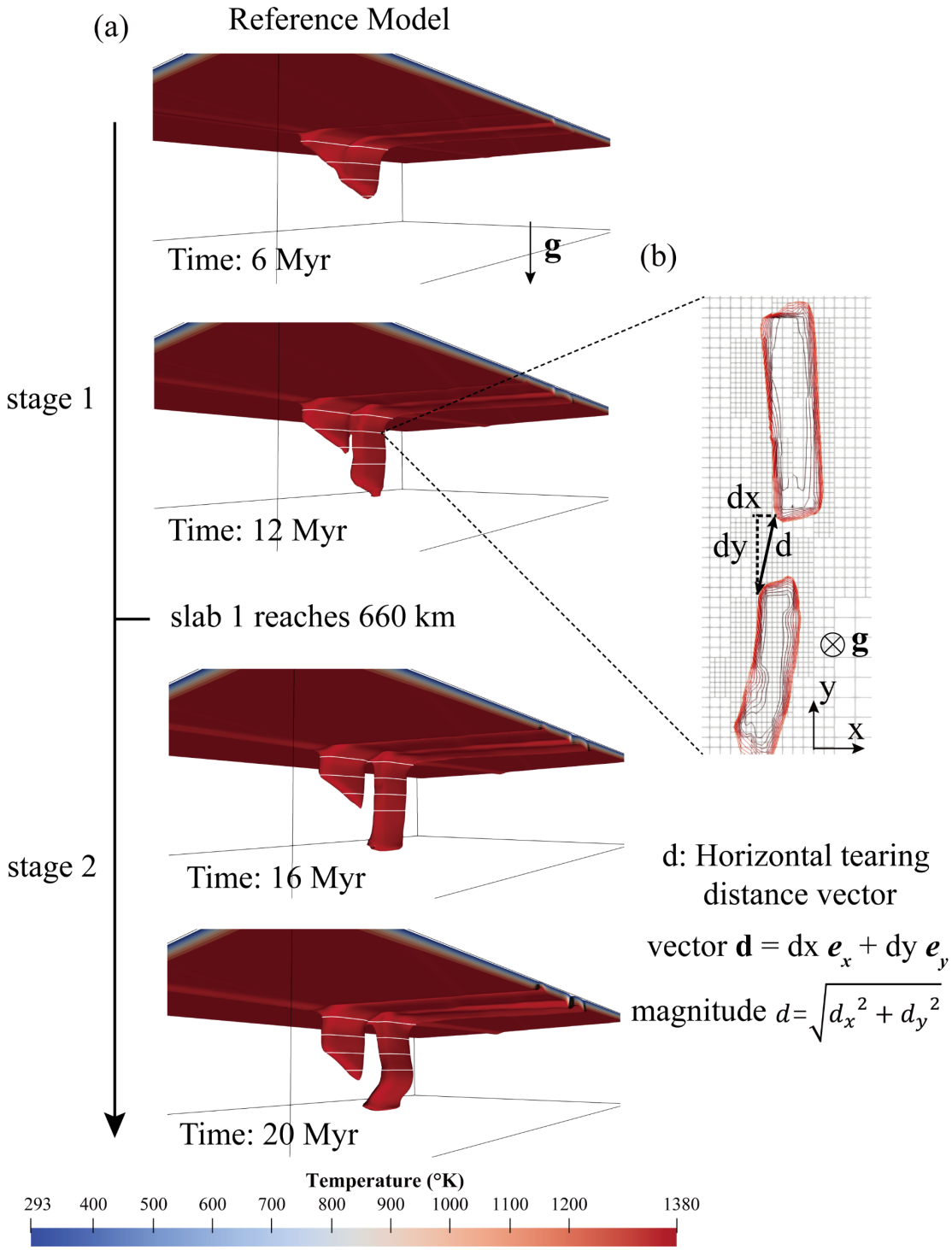

Figure 3. (a) Oblique view: Reference model evolution shown by isolating temperatures ≤1380 °K (so the slabs are visible approximately as an isothermal surface, and at shallow depths a thermal gradient is visible). Model parameters: oceanic-lithosphere slab ages t_1 = 33 Ma, t_2 = 27 Ma; horizontal obliqueness θ=20°. **(b) View from above**: Definition and quantification of slabs tearing at different depths (100-200-300-400 km), with the variable "d" being the time-dependent horizontal vector distance (of magnitude 'width') of slabs' tearing window. The vector-components ratio "dx/dy" and the oblique-convergence angle θ are used to characterize

the slabs' tearing patterns as explained in subsection 3.2 and 4.3.

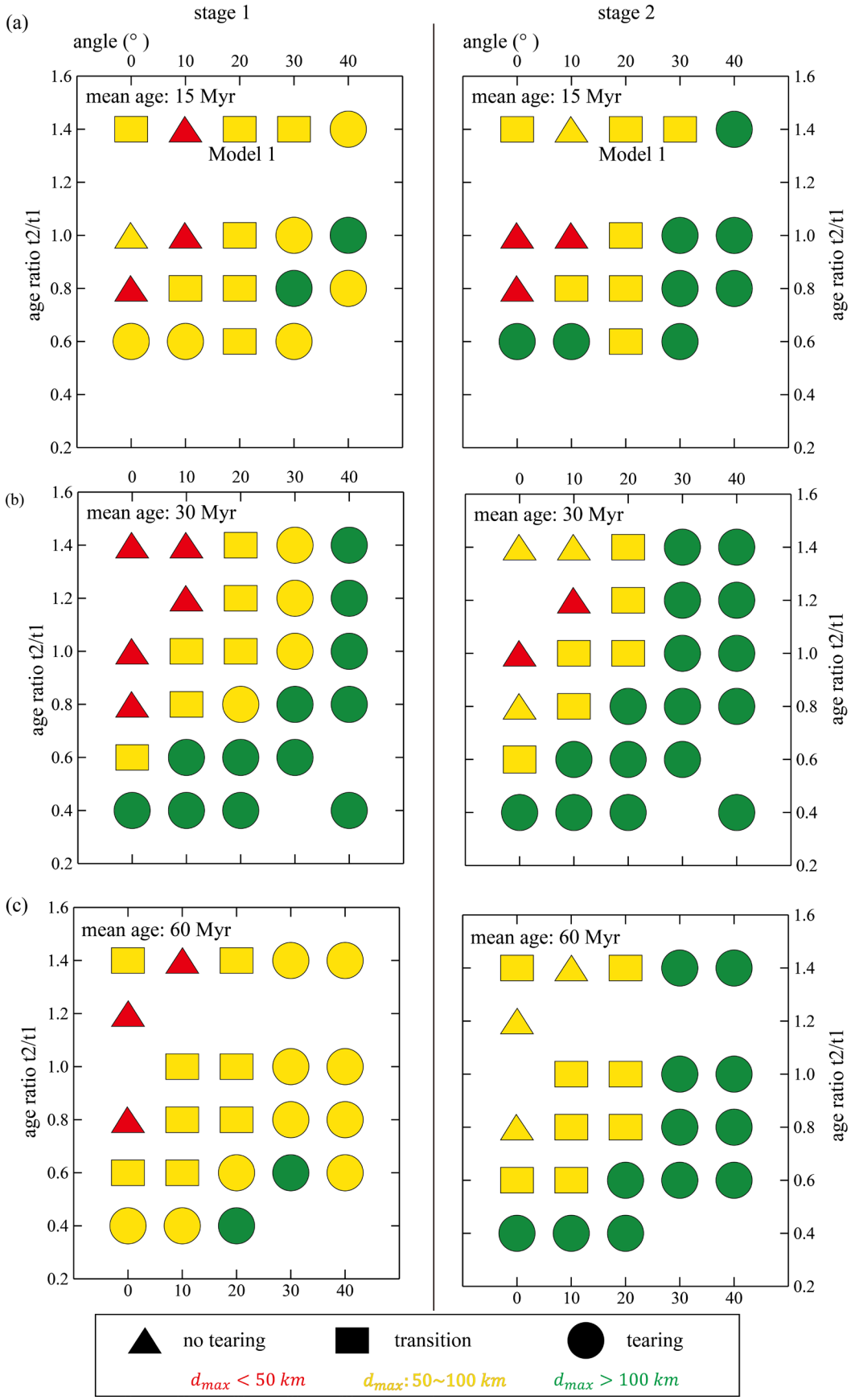

Figure 4. Check-box diagrams for the models' tested conditions. *Angle* means the horizontal obliqueness angle in the systems. The arithmetic-mean lithospheric age of slabs 1 and 2, $((t_1+t_2)/2)$, is 15 Myr (a), 30 Myr (b), and 60 Myr (c), respectively, defining the rows of the array plot. A slab reaching the 660 km-depth event defines the columns of the array plot: stage 1 (before) and stage 2 (after). The category of slab-tearing discrimination: Colors indicate the geometric state of slab tearing at each particular time-stage (at 1 (left) and at 2 (right)), as Red: maximum tearing width d_{max}<50 km, yellow: d_{max}: 50-100 km, green: d_{max}>100 km. Symbol shapes indicate the situation integrated through both time-stages: If at any of the two stages the tearing width is <50 km, the model is classified as "no tearing" (triangles), and if >100 km the model is "tearing" (circles), while cases in between are transitional modes (rectangles). These symbol shapes are necessary for the subsequent figures of this article.

Each one of the three major rows on the diagram in Figure 4 summarizes the results of simulations with the same arithmetic-mean age $\frac{t_1+t_2}{2}$ of the plates separated by the transform fault. To classify each simulation, we use relative age ratio rather than age difference as a way to avoid discussing parameters that deviate far from nature, i.e., $t_1 - t_2 = t_1\left(1 - \frac{t_2}{t_1}\right)$, For the same age ratio, a younger mean age suggests a smaller absolute age difference. For any given mean age, significant oceanic-plate tearing is favored by a large obliqueness angle and/or by older slab-1 age relative to slab-2. Most models fail to tear without horizontal obliqueness of the subduction (angle θ=0°) except for medium-aged plates with substantial age differences.

In particular, due to thin slabs, Model 1 (1318_20) in the low mean absolute age group (15 Myr) exhibits lateral break-off, increasing tearing width. At 60 Myr-30° and 60 Myr-40°, the tearing width does not increase beyond a certain extent before slab 1 reaches the bottom, so its tearing width is small during stage 1. In cross-sectional comparison, we find that the tearing area is larger in stage 2 than in stage 1, especially the 60 Myr group changes from yellow to green color code. In the vertical comparison, we found that the tear area increases and then decreases with increasing mean age, which will be further analyzed in the subsequent discussion.

In conclusion, our simulations suggest that for any values of obliquity, the subducting plates tear for age ratios less than 0.6, meaning that an older-thicker slab-1 entering the

trench first, then sinking first and faster, progressively tears off from slab-2. Furthermore, regardless of the transform-fault age ratios, all the plates tear at horizontal obliqueness greater than 30°. This latter behavior is certainly an effect of the contact surface forces exerted by the overriding (continental) plate on forcing the bending of an obliquely-subducting slab-1 first and then later on slab-2. The larger the horizontal-obliqueness angle, the larger the difference between the slabs' subducted areas (especially during the early stages of the process) and the more intensive and extensive the strain of the weak fault zone between the slabs. Finally, as crucial reference cases, we must note the case when the horizontal-obliqueness $\theta = 0°$ and simultaneously slabs' age-ratio=1, meaning two identical slabs separated by a weak zone and converging perpendicular to the trench. Those simulations show tearing displacements that when existing and being measurable at all, have values $d_{max} < 50$-75 km, meaning that tearing almost does not occur (symbolized as triangles, in red and yellow in Figure 4).

3.2. Patterns of vertical slab tearing

In this study, we consider the horizontal distance vector of tearing displacement between the slabs: $d = d_x\,\mathbf{e_x} + d_y\,\mathbf{e_y}$, measured at depth in their vertical portions inside the ambient mantle.

The maximum tearing width (displacement magnitude) over different depths of the subducting plate (depths: 100-200-300-400 km) is used to indicate whether tearing occurs (summarized in Figure 4). In addition, the ratio of the tearing vector components in the transform-fault-based system (given an obliqueness angle θ, see Figures 2 and 3 for definitions) is employed to characterize the tearing patterns. We project the tearing distance-vector components d_x and d_y (referred to trench perpendicular-and-parallel coordinates, respectively) onto the initial horizontally-oblique-convergence direction and its normal direction (i.e., onto the coordinate system defined by the transform-fault direction and its perpendicular), respectively, to obtain the fault-parallel $d_{fault//}$ and fault-perpendicular- $d_{fault\perp}$ tearing components. We obtain:

$$\frac{d_{fault//}}{d_{fault\perp}} = \frac{d_x cos\theta + d_y sin\theta}{-d_x sin\theta + d_y cos\theta} = \frac{\frac{d_x}{d_y} + tan\theta}{1 - \frac{d_x}{d_y} tan\theta} \quad (5).$$

When $|\frac{d_{fault//}}{d_{fault\perp}}|$ >1.3, the tearing pattern is defined as fault-parallel tearing (related to slabs' differential hinge retreat or rollback) (Figure 5). In contrast with $|\frac{d_{fault//}}{d_{fault\perp}}|$ <0.7, the pattern is defined as fault-perpendicular tearing, in which the along-slabs-hinge-axis tearing dominates. A transitional-intermediate mode is defined as between (0.7-1.3).

Specifically, at each desired time, we take the average (arithmetic mean) value of the aforementioned ratio at the different depths and consider that average for the subsequent determination of the tearing pattern (Figure 3b and Figure 5).

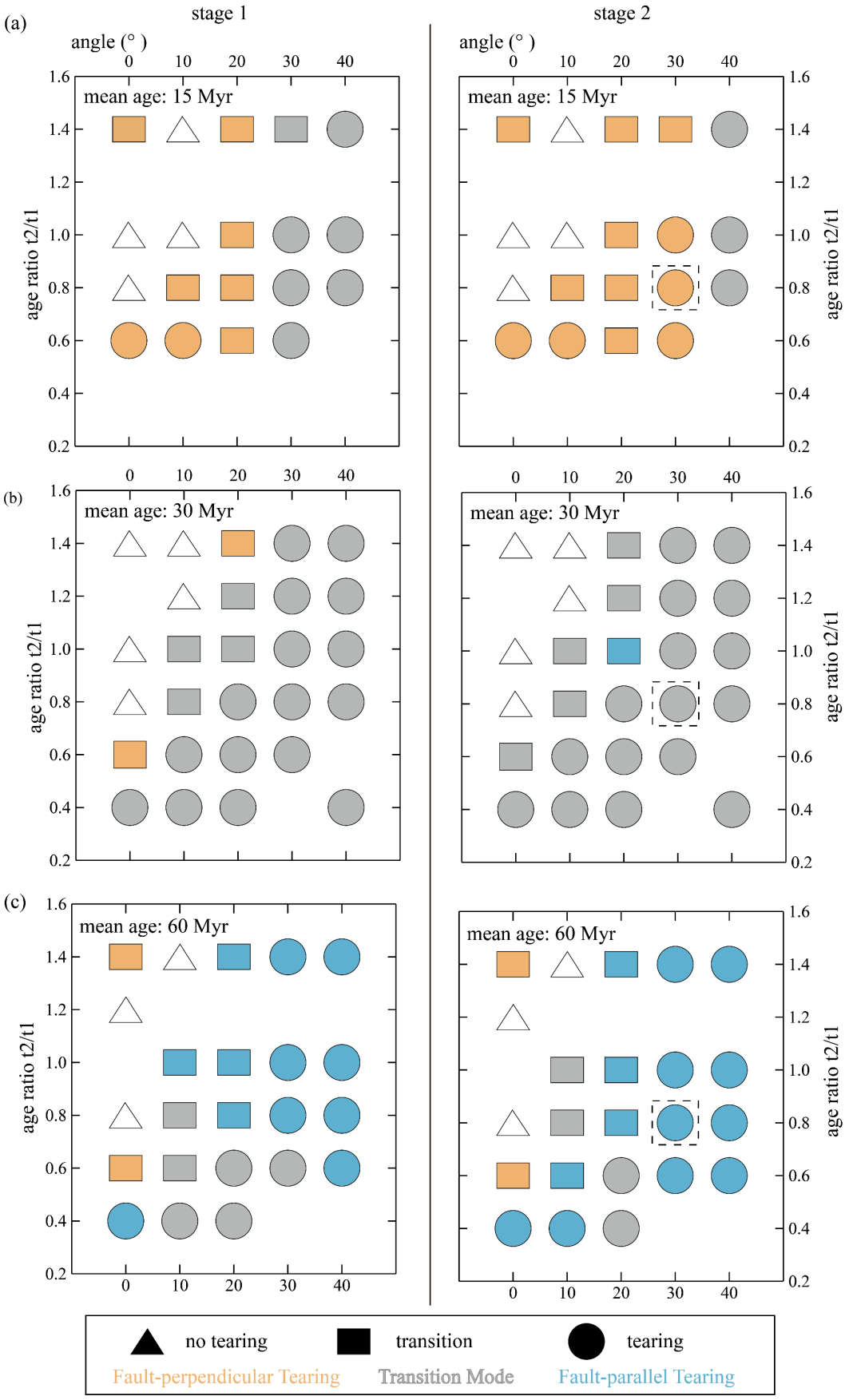

Figure 5. Check-box diagrams for the tearing patterns on time-stages 1 (left) and 2 (right). *Angle* means the horizontal-obliqueness angle. The arithmetic-mean lithospheric age of slabs 1

and 2, ($(t_1+t_2)/2$), is 15 Myr (a), 30 Myr (b), and 60 Myr (c), respectively. The category of slabs tearing pattern, depending on the ratio "$|d_{fault//}/d_{fault\perp}|$". Orange: If $|d_{fault//}/d_{fault\perp}| < 0.7$, the pattern is defined as fault-perpendicular tearing. Blue: In contrast with $|d_{fault//}/d_{fault\perp}| >$ 1.3, the pattern is defined as fault-parallel tearing. Gray: A transition-hybrid mode is 0.7-1.3. The definition of symbol shapes is the same as in Figure 4. Each age-group stage-2 simulations enclosed by dashed-line squares are used in figures 6 and 7.

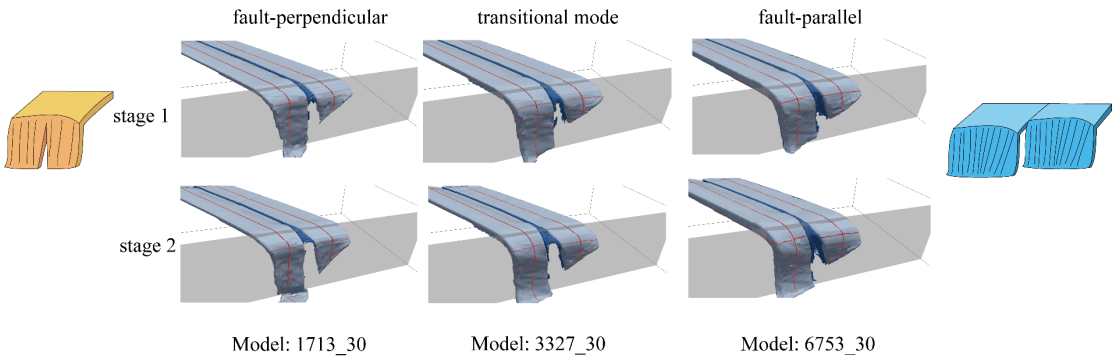

Figure 6. Example models illustrating the three different slab tearing patterns (determined by the ratio of tearing horizontal-displacement components). End-member cartoons are provided for illustration. These three particular example simulations (signaled by dashed squares in Figures 5a,b,c), while differing only in their slabs' mean age, all have age ratios of about ~0.8 and obliqueness-angle θ=30°.

Plate-motion horizontal obliquity influences the fault-parallel and also the transverse/fault-perpendicular direction of forces and resulting tearing displacements. However, it seems dominant only in young slabs, such as the region less than 40° in the 15 Myr group in Figure 5. On the other hand, large absolute age differences generally result in large sinking velocity differences that project in the convergence direction, such as the region θ ~> 20° and t_2/t_1 ~< 0.6 (bottom left corner) in the 60 Myr group in Figure 5.

As shown by Figure 6, considering older slabs at the initial condition, with mean ages from 15 to 30 to 60 Myr, fault-perpendicular tearing patterns tend to disappear (occurring only in some cases), meaning that it is mostly a young-age tearing behavior. On the other hand, fault-parallel manifests commonly-extensively only for old slabs with a mean age of 60 Myr, with only one exception at a mean age of 30 Myr.

Figure 7 shows the evolution of the typical models of the two tearing patterns,

simulation 1713_30 for fault-perpendicular tearing and simulation 6753_30 for fault-parallel tearing. The larger mean age/thickness enhances the differential retreat of the two slabs in the convergence direction, causing the vertical tearing (while inside the mantle) pattern to be dominated by fault-parallel tearing (Figures 7 a,d). In fact, at old slab ages (such as 60 Myr), the same age ratios as in the other age groups are attained with larger absolute-age differences, and these latter ones imply larger absolute sinking-and-subduction velocity differences (see subsection 4.1). Therefore, old-age slabs tend to favor differential slabs' retreat and fault-parallel tearing (Figure 5). Additionally, the distance from the trench to the 90° slab-dip angle position, called the bending length l_b, varies between the two differentially-retreating slabs and with time evolution, and this will be further analyzed in the subsequent discussion section (Figures 7 b,c).

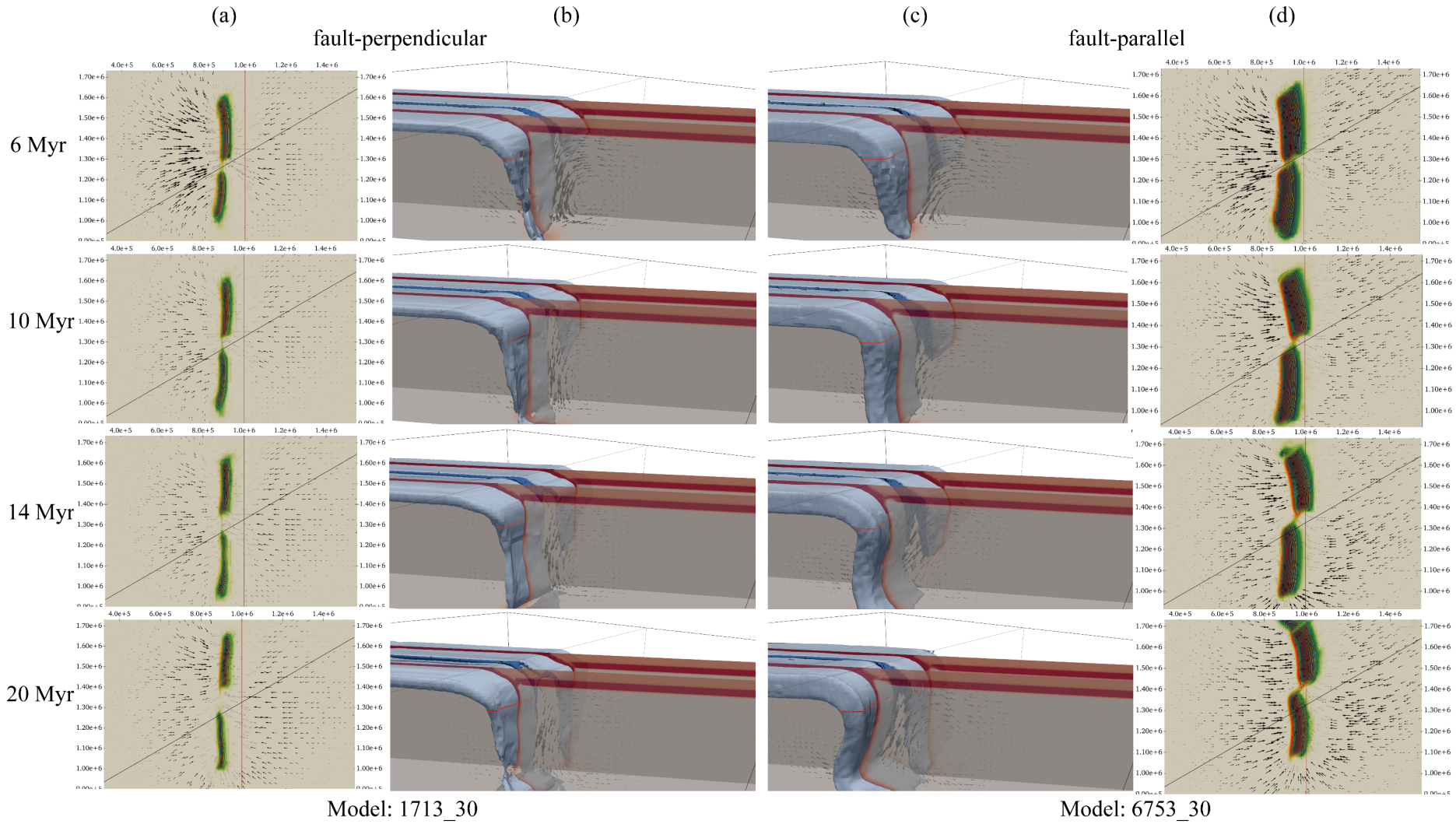
(a)
(b)
(c)
(d)
fault-perpendicular
fault-parallel
6 Myr
10 Myr
14 Myr
20 Myr
Model: 1713_30
Model: 6753_30

Figure 7. Evolution of the two case simulations that exemplify the two tearing patterns, singled out and indicated by dashed-line squares in Figure 5. Panels (a) and (d): View from above, thermal contour (yellow, the legend is the same as Figure 3) and viscosity (green) structure (Table 2) at 150 km depth. Small black arrows: ambient-mantle velocity vector field. Black oblique line: All-time slabs' prescribed horizontal convergence direction. The red line at fixed abscissa x: initial trench-line position. Panels (b) and (c): Oblique views, oceanic lithosphere (light blue) and transform fault (dark blue) as compositional fields. Additionally, 2D vertical slices of the overriding-continental plate's mass-density field are shown (plum-red colors and density values specified in Table 2).

4. Discussions

4.1. Analytical study of the slab tearing dynamics

In order to understand how the various controlling factors operate in our simulations and to enhance the verifiability of the model results, we utilize scaling similarity theory and available analytical-numerical studies.

We hypothesize that the horizontal width (d) of the tearing window is correlated to the difference in subduction velocity Δv between the two slabs separated by a transform fault. In a 2D subduction model, the oceanic slab is primarily subjected to (i) downward-buoyancy force $\delta\rho \cdot \mathbf{g} \cdot h \cdot l$ per unit length (with $\delta\rho$ density anomaly, $\mathbf{g}$ gravity acceleration, h the oceanic plate thickness, and l the slab tip-length along convergence direction), (ii) surrounding mantle resistance F_1 along the tangential direction of the slab $\eta_{\text{mantle}} \cdot v$ (where v is the plate speed, η_{mantle} the ambient-mantle viscosity), and (iii) unbending resistance F_2 perpendicular to the slab $\eta_{\text{plate}} \cdot v \cdot h^3/l_b^3$, where η_{plate} is the oceanic-plate viscosity, l_b is the bending length from the slab tip to the unbending place behind the hinge point (similar to the previous description of Figure 7 (Li & Ribe, 2012; Ribe, 2001) (Figure 8c). Then we take the one-slab tangential velocity $v_{2D} = \frac{\delta\rho \cdot g}{\eta_{mantle}} sin\alpha \cdot h \cdot l$ (in an idealized, terminal steady-state scenario where the slab, driven by the downward-buoyancy force, is 'gliding' inside the viscous mantle) along the slab subduction direction, as the major component that defines the tangential velocity difference Δv between slabs, yielding

$$\Delta v = \frac{\delta\rho \cdot g * sin\alpha}{\eta_{mantle}} (h_1 l_1 - h_2 l_2) \tag{6}$$

where α is the subduction dip (vertical) angle.

We assume that at the initial-condition of the subduction zone, in each one of the two slabs subducted portions (Figure 2), their thicknesses h_1 and h_2 remain constant. Then in this initial configuration and due to horizontal obliqueness, the initial slabs subducted-length l varies along the trench direction (y-direction) following $l(y, \theta) = \frac{c + y \cdot tan\theta}{cos\alpha}$, with $l_{min} = \frac{c}{cos\alpha}, l_{max} = \frac{c + 2w \cdot tan\theta}{cos\alpha}$, where c is fixed at 100 km (Figure 2b). Then we get $v_{3D} = \int_0^w v dy / \int_0^w 1 dy$, as the spatial-average velocity of the entire slab tip, with

w the horizontal span of the slab along the trench axis.

So, $v_{3D,1} = \frac{\delta\rho \cdot g sin\alpha}{\eta_{mantle}} \int_{w}^{2w} h_1 l(y) dy / \int_{w}^{2w} 1 dy$, $v_{3D,2} = \frac{\delta\rho \cdot g sin\alpha}{\eta_{mantle}} \int_{0}^{w} h_2 l(y) dy / \int_{0}^{w} 1 dy$.

Then, the simple-theoretical spatial-average velocity difference between slabs is obtained as $\Delta v_{3D} = v_{3D,1} - v_{3D,2} = \frac{\delta\rho \cdot g sin\alpha}{\eta_{mantle}} \cdot \frac{1}{2cos\alpha} \cdot [2c(h_1 - h_2) + (3h_1 - h_2) w \tan\theta] = \frac{\delta\rho \cdot g \cdot b \cdot tan\alpha}{2\eta_{mantle}} \cdot \left[2\frac{c}{b}\left(\frac{h_1}{h_2} - 1\right) + \left(3\frac{h_1}{h_2} - 1\right)\frac{sin\theta}{(cos\theta)^2}\right] \cdot h_2 \doteq k \cdot C \cdot h$, where $k = \frac{\delta\rho \cdot g \cdot b \cdot tan\alpha}{2\eta_{mantle}}$ (the unit is s^{-1}) is a functional factor composed of several dynamic parameters kept constant in each model simulation for simplicity, $b=w/cos\theta$ is the fixed slab width (Figure 2b), and the functional factor $C = 2\frac{c}{b}\left(\sqrt{\frac{t_1}{t_2}} - 1\right) + \left(3\sqrt{\frac{t_1}{t_2}} - 1\right)\frac{sin\theta}{(cos\theta)^2}$ considers the geometrical parameters reflecting the horizontally-oblique subduction effects, with the ratios of the square root of time representing ratios of thermal-age thicknesses, as $h \approx 2.32\sqrt{\kappa t}$ gives each oceanic slab thickness h versus its seafloor age t.

Following the logic of the unbending-resistance form $\eta_{plate} \cdot v \cdot h^3 / l_b^3$, in order to find the correlation between the model-output computed tearing distance d and the theoretical underlying controlling factors for the velocity difference Δv, we consider an additional multiplying variable factor f in the former simple-theoretical expression. f is a dimensionless parameter representing additional effects on Δv, such as unbending resistance along the slab-normal direction, differences between the two slabs' bending-sinking lengths and thicknesses, viscosity and width of the weak zone (transform fault), etc.; all of which depend on time as the sinking process evolves.

Therefore the original dimensional expression $k \cdot C \cdot h$ is expanded, upgraded and refined to $k \cdot C \cdot h \cdot f$. In this way, the dimensionless parameter f should accommodate for the aforementioned additional effects, and we use trial expressions of the form $f \approx \left(\frac{h_2}{h_1}\right)^n \frac{l_{b_1}}{l_{b_2}}$ to represent and account for them.

We used a set of fixed times (10 Myr, 14 Myr, 20 Myr) and depth range (100-400 km) to compare and correlate the tearing horizontal-width d with the spatial-average velocity difference Δv between slabs (brought by analytical scaling theory), and the results are shown in Figures 8-11. The figures are plotted for respective absolute mean ages of plates at {15, 30, 60} Myr and all of them together.

Upon constructing the correlations shown in Figures 8-11 and Table 3, we have removed four simulations from the data set, specifically simulations 1318_30, 1318_40, 1515_20, and 1515_30. This was done because these particular young "ultra-thin" slabs broke off during the subduction process, so we cannot precisely measure the tearing width in these models. Simulation 4317_40 can greatly increase the correlation coefficient in a way we distrust, so we also discarded it.

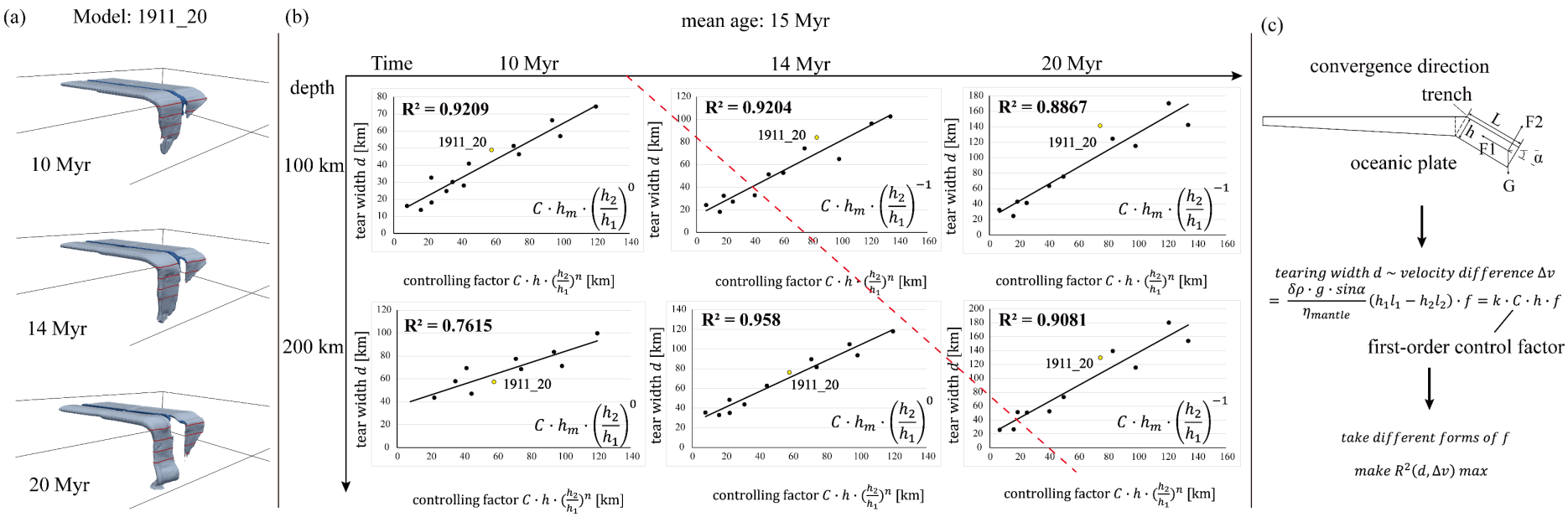

Figure 8. (a) Snapshots of model 1911_20 (slabs reference ages t_1=19 Myr, t_2=11 Myr, mean age 15 Myr, and subduction obliqueness θ=20°) at 10, 14, and 20 Myr of simulated time, showing the evolution of the oceanic lithosphere and the transform fault-zone tearing. The thin red curves on slabs are selected paths for geometry and tearing assessment computation (at 100, 200, 300, and 400 km depths). (b) The six different panels display trials on the functional forms of the slabs' velocity difference ($\Delta v/k = C{\cdot}h{\cdot}f$) depending on evolution time (large horizontal axis) and depth (large vertical axis), and their correlation with the slabs' horizontal tearing width (d). The correlation coefficient between tearing horizontal width (small vertical axis) and velocity difference controlling factor (small horizontal axis) is shown on each panel's top-left corner. The control parameters are consistent within each one of the areas delimited by the red dashed slash. (c) The major forces analysis on the tip part of a two-dimensional subducting slab with slab thickness h, initial slab length l, and subduction dip angle α. These plots illustrate the search for the maximum correlation coefficient between the slabs' tear horizontal width and the slabs-segments velocity difference by trying different functional forms of the latter.

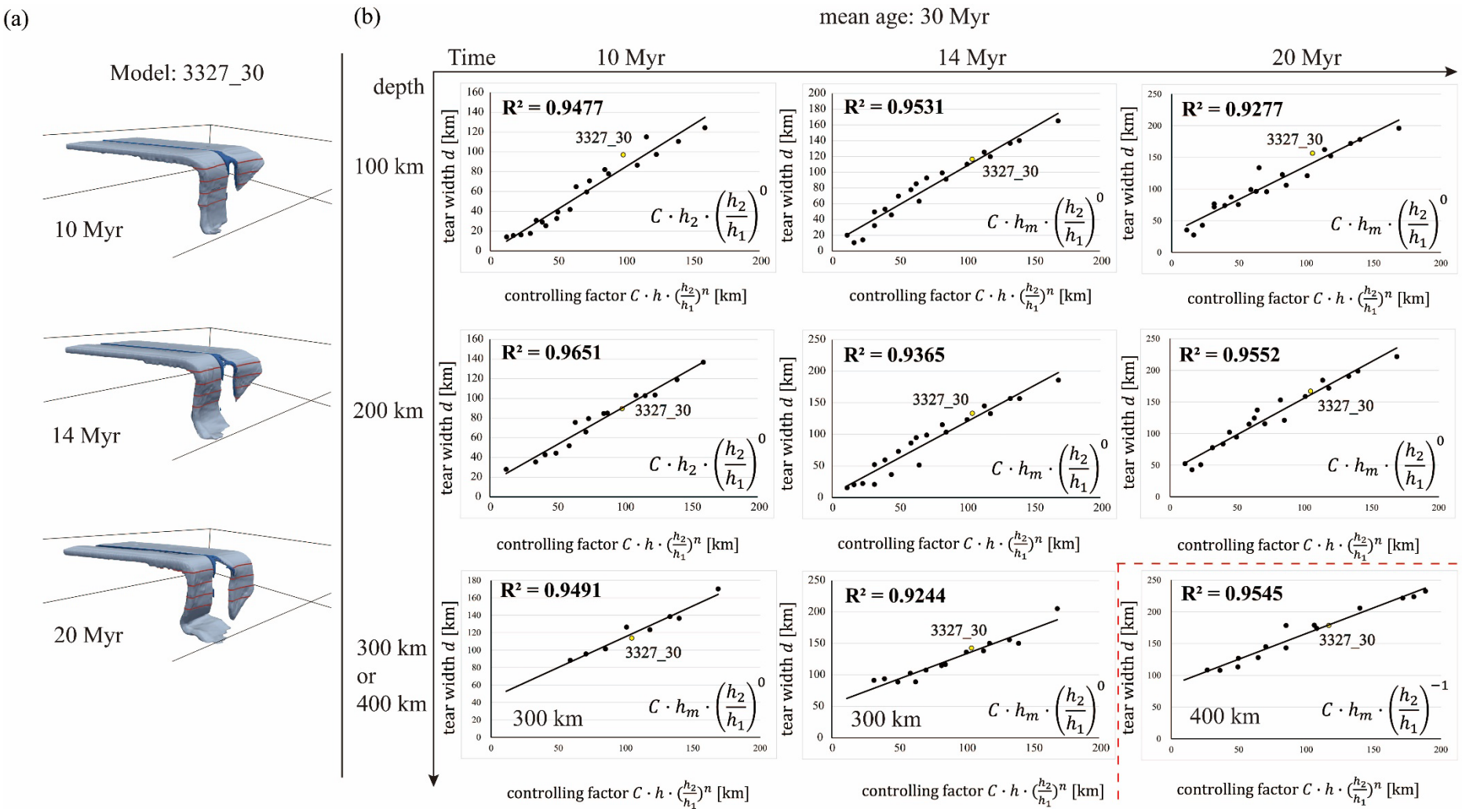

Figure 9. (a) Snapshots of particular model 3327_30 (slabs reference ages t_1=33 Myr, t_2=27 Myr, mean age 30 Myr, and subduction obliqueness θ=30°) at 10,

14, and 20 Myr, showing the evolution of the oceanic lithosphere tearing. The thin red curves on slabs are selected slices for geometry and tearing assessment computation (at 100, 200, 300, and 400 km depth). (b) The nine different panels display the correlation between slabs tearing horizontal width (d) and the integrated controlling factor ($\Delta v/k = C \cdot h \cdot f$). Correlation coefficients (R^2) are shown on the top-left corner of each panel. The control parameters are consistent within each one of the areas delimited by the red dashed line.

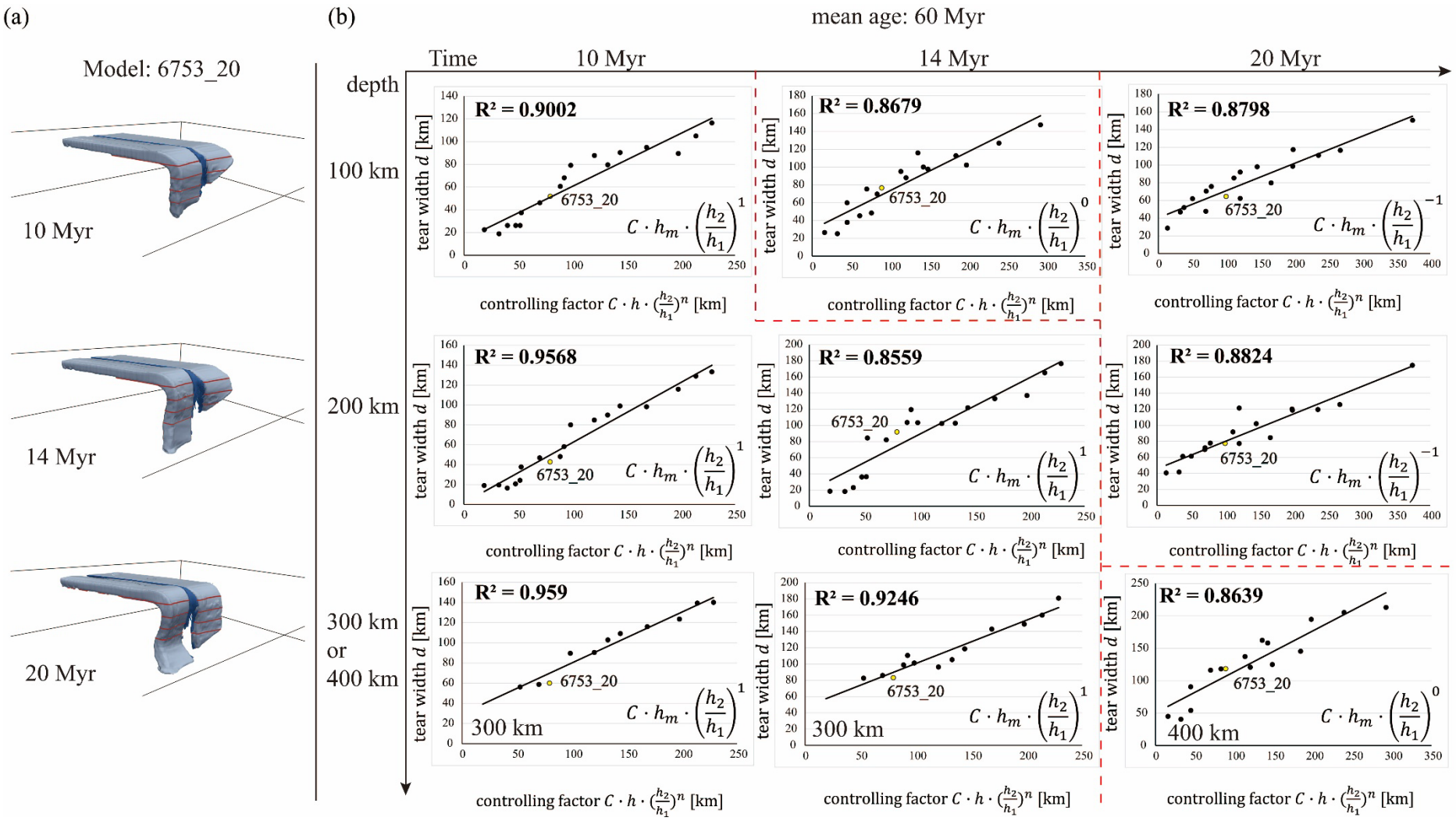
(a)
Model: 6753_20
10 Myr
14 Myr
20 Myr
(b)
mean age: 60 Myr
Time
10 Myr
14 Myr
20 Myr
depth
100 km
200 km
300 km
or
400 km
R² = 0.9002
R² = 0.8679
R² = 0.8798
R² = 0.9568
R² = 0.8559
R² = 0.8824
R² = 0.959
R² = 0.9246
R² = 0.8639
6753_20
300 km
400 km
tear width d [km]
controlling factor C · h · (h2/h1)^n [km]

Figure 10. (a) Snapshots of particular model 6753_20 (slabs reference ages t_1=67 Myr, t_2=53 Myr, mean age 60 Myr, and subduction obliqueness θ =20°) at 10, 14, and 20 Myr, showing the evolution of the oceanic lithosphere tearing. The red curves on slabs are selected slices for geometry and tearing assessment computation. (b) The nine different panels display the correlation between slabs tearing horizontal width (d) and the integrated controlling factor ($\Delta v/k = C \cdot h \cdot f$). Correlation coefficients (R^2) are shown on the top-left corner of each panel. The control parameters are consistent within each one of the areas delimited by the red dashed lines.

After a detailed analysis of our numerical experiments (Figures 8-10), we find that the tearing horizontal width d is sensibly and roughly proportional to the slabs' velocity difference. Our hypothesis is reasonably confirmed. If we consider the "full" scaling form for the velocity difference $\Delta v = k \cdot C \cdot h \cdot (h_2/h_1)^n$, the correlation coefficient R^2 is in the range of 0.76~0.97 (see Table 3) considering all depths and times, age groups and simulation cases. For comparison, if employing the much simpler "incomplete" scaling form $\Delta v = k \cdot C$, the range of R^2 is 0.69~0.96 for the same simulations cases as in the previous trial (see Table 3). Therefore, regarding the similarity between the two correlation-values intervals, it is inferred that the first-order governing factor is the oblique convergence given by the characteristic parameter $C=C(\theta)$, as defined in Equation 6.

Table 3. Correlation between the slabs tearing horizontal width d and the "full" scaling form for the velocity difference ($\Delta v = k \cdot C \cdot h \cdot f$) at different times and depths. In parentheses: Correlation between d and the "incomplete" scaling form ($\Delta v = k \cdot C$). The range of {min, arithmetic mean, max} values of correlations R^2 for the "full" and "incomplete" scaling forms are {0.76, 0.91, 0.97} and {0.69, 0.84, 0.96}, respectively.

R^2 (d, Δv) Mean age:15 Myr	10 Myr	14 Myr	20 Myr
100 km	0.92 (0.92)	0.92 (0.84)	0.89 (0.80)
200 km	0.76 (0.76)	0.96 (0.96)	0.91 (0.83)
300 km	——	——	——
400 km	——	——	——
R^2 (d, Δv) Mean age:30 Myr	10 Myr	14 Myr	20 Myr
100 km	0.95 (0.93)	0.95 (0.95)	0.93 (0.93)
200 km	0.97 (0.91)	0.94 (0.94)	0.96 (0.96)
300 km	0.95 (0.95)	0.92 (0.92)	——
400 km	——	——	0.95 (0.88)
R^2 (d, Δv) Mean age:60 Myr	10 Myr	14 Myr	20 Myr
100 km	0.90 (0.81)	0.87 (0.87)	0.88 (0.82)
200 km	0.96 (0.84)	0.86 (0.81)	0.88 (0.88)
300 km	0.96 (0.86)	0.92 (0.86)	——
400 km	——	——	0.86 (0.87)
R^2 (d, Δv) All simulations	10 Myr	14 Myr	20 Myr
100 km	0.90 (0.76)	0.86 (0.77)	0.90 (0.69)
200 km	0.91 (0.79)	0.90 (0.80)	0.91 (0.69)

300 km	0.87 (0.71)	0.83 (0.74)	——
400 km	——	——	0.86 (0.76)

In particular, if we divide each group of time-depth diagrams along the diagonal line (Figures 8-10), the parameter changes can roughly reflect the tearing width evolution in different segments of the ocean plate. Most parameters remain consistent within each one of the areas delineated by the red slash, reflecting the previous deformation history inherited by the slab during most of the subduction. The variation of parameters in various intervals from the lower left to the upper right depicts the variation of governing factors with subduction, which is dependent on $(h_2/h_1)^n$, like n = 0→-1 in the 15 Myr-age group and n = 1→0→-1 in the 60 Myr-age group (Figures 8b, 10b), and n = 0→-1 at 300-400 km depth in the 30 Myr-age group (Figure 9b).

This overall reduced evolution represents the effect of unbending resistance F_2 in various plate segments. The oceanic lithosphere subducted length l of slab-2 is obviously smaller than that of slab-1 during the early stages of subduction (well before the two slabs are dipping sub-vertically). The smaller l in slab-2, the stronger the unbending resistance and the apparently “stiffer” the slab. Accordingly, "stiffer" slab-2 affects the change of tearing width when $h=h_2$, $n=1$. The overall subduction dip angle (including that of slab-1) increases as slab-2 subducts, and the effects of F_2 grow weaker at this point with $h=h_{mean}$ and $n=0$. Later on, with continued slabs sinking, there is the singular event of slab-1 reaching 660 km depth: slab-1 is subjected to a force at the bottom that resists bending. At this point, the velocity-difference Δv turns to be controlled by slab-1, with the exponent transitioning to $n=-1$. As for the variation of the specific value of n in different age groups (15, 30, 60 Myr), we believe it is f that is also correlated with l_{b1}/l_{b2}. The changes in bending length compensate for some of the changes in slabs’ thickness ratio.

Finally, it can be seen that the controlling parameters change in the slabs deepest regions (400 km) on stage 2 (20 Myr) (Figure 9b, 10b). We think it is slab-1 here that is bent at the bottom of the model, that is associated with the folding pattern in the 30

Myr-age group and the trench retreating pattern in the 60 Myr-age group (Figure 9a, 10a) (Li & Ribe, 2012).

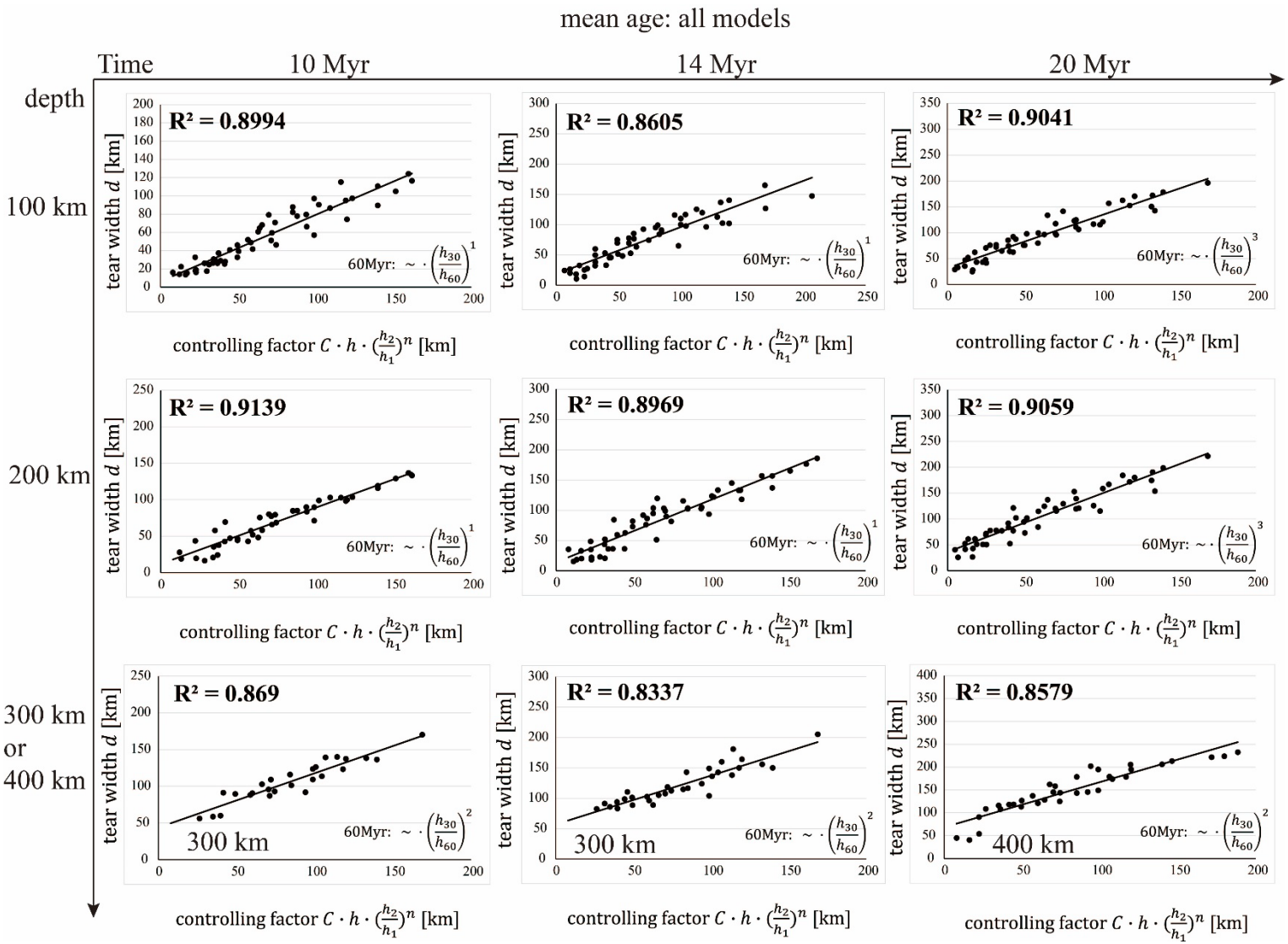
mean age: all models
Time
10 Myr
14 Myr
20 Myr
depth
100 km
200 km
300 km
or
400 km
R² = 0.8994
R² = 0.8605
R² = 0.9041
R² = 0.9139
R² = 0.8969
R² = 0.9059
R² = 0.869
R² = 0.8337
R² = 0.8579
300 km
400 km
60Myr: ~ · (h30/h60)^1
60Myr: ~ · (h30/h60)^3
60Myr: ~ · (h30/h60)^2
tear width d [km]
controlling factor C · h · (h2/h1)^n [km]

Figure 11. The nine panels display the correlation between slabs tearing width (d) and the integrated controlling factor ($\Delta v/k = C \cdot h \cdot f$) for all models. The correlation coefficients (R^2) are shown in the top left corner of each panel. We find that an additional multiplication factor $(h_{30}/h_{60})^p$ must be applied in the 60 Myr mean-age simulations for the $dv=k \cdot C \cdot h \cdot f$ function-group to capture a certain influence of slabs thickness differences on tearing width, and in this way they fit in reasonably with the other age groups.

The comparison among the models with different mean slab ages indicates that the older slabs of 60 Myr generally have a narrower tearing window than the mid-age slabs with mean ages of 30 Myr (Figures 4, 11).

Certainly, an additional multiplication factor $(h_{30}/h_{60})^p$ must be applied in the 60 Myr mean-age simulations to fit in with the other age groups at similar correlation levels (Figure 11). At old-plate ages (mean 60 Myr), the full scaling form $\Delta v = k \cdot C \cdot h \cdot f$ (with $f = (h_2/h_1)^n$) yields values that are too big (because h is big). Therefore, an additional post-factor <1 is needed to fit the observed values of d through the range of Δv values of the different simulations and to get similar correlation levels to those of the other age groups.

Beyond this, we believe that the smaller values of tearing width in the 60 Myr than in the 30 Myr age group may be related to the difference in bending length (to measure the effect of bending length (l_{b1}/l_{b2}), we use the average slab-thickness ratio $(h_{30}/h_{60})^p$, which can be compared quantitatively) involving viscous dissipation, with older-thicker slabs offering higher viscous resistance to bending and retarding the development of the bending-length increase. The sequence of slabs-1,2 changing from small to large bending length is different when plate age-thicknesses are large (Figure 6). The apparently rheologically weaker slab-1 changes "earlier" in the plate-thickness sinking-velocity parameter space than slab-2, increasing the tearing width from 15 Myr-age groups to 30 Myr-age groups and then decreasing (just to some extent) from 30 Myr-age groups to 60 Myr-age groups. This effect is more apparent in the later phases of subduction and at larger depths, as shown by the change of p in Figure 11. This feature is also shown in the shift of the age ratio cut-off with absolute age in Figure 4.

In summary, vertical oceanic-plate tearing is controlled by two dominant factors, (i) the subduction horizontal obliqueness: the larger the obliqueness angle, the larger the difference in the subducted area of the two slabs, the higher the likelihood for slabs tearing; (ii) the difference between the ages of the two slabs: tearing across/along the transform-fault zone is favored by older, heavier, thicker slab-1 relative to slab-2, as this configuration plays constructively with the obliqueness. The plate unbending

resistance effect varies among the individual slabs thicknesses and also among the different subduction zones (in real Earth), but seems to only play a secondary role in tearing generation and development.

4.2 On transform-fault-perpendicular tearing

In subsection 3.2 we showed that tearing horizontal-displacement-components ratio, when expressed in the transform-fault-based coordinate frame can take diverse values far-from yet about 1. If dominated by fault-parallel component, we recall that slabs differential roll-back and differential hinge retreat is a relatively normal phenomenon in geosciences. Contrastingly, if dominated by fault-perpendicular component the slabs may be slightly separating inside the asthenosphere, parallel to their transversal/hinge axes. We will shed light on this hitherto yet-to-be-understood phenomenon.

We already provided kinematical (visual displays of geometry versus time) evidence that this transform-fault-perpendicular tearing displacement can dominate the tearing, and that it manifests only for horizontal-obliqueness $\theta \leq 30°$ and more frequently in young slabs (section 3.2, Figure 5). We shall now show some supporting dynamical evidence for this tearing behavior.

Let's consider X' as the fault-parallel axis and Y' the fault-perpendicular axis. Appendix figure S1 displays the viscous horizontal shear stress on the slabs surface for simulation 1713_30 (lithospheric ages t_1 = 17 Ma, t_2 =13 Ma; horizontal obliqueness θ = 30°) which exemplifies transform-fault-perpendicular tearing. The viscous horizontal shear stress $\sigma_{y'x'}$ is shown at 6 and 12 Myr of computed geological time. Given the horizontal-obliqueness angle θ = 30°, the relative motion between the slabs and the overriding continental plate, particularly the tangential/trench-parallel component, influences the local stress field on the surface of these bodies: the surface viscous friction imprinted by the relative motion dictates the shear stress. The effects of this shearing may not be equal on the two slabs regarding their different ages and subducted volumes versus time, and the interaction with the overriding plate may even be unsteady in time, resulting in an increasing separation between the slabs.

Appendix figure S2 (in its left column) shows the viscous horizontal normal deviatoric stress on a 2D vertical slice along the transform-fault-zone central-axis for simulation 1713_30 exemplifying transform-fault-perpendicular tearing. The stress $\sigma_{y'y'}$ is shown at {4, 6, 8, 10, 12, 14} Myr of computed geological time. The normal deviatoric stress $\sigma_{y'y'}$ (left-side panel) inside the transform-fault-zone is extensive in-and-around the subduction hinge (bent), and slightly compressive where the slabs are close to each other far from the trench in the horizontal portions; and this stress pattern changes only slightly during this particular subduction process. With time, the fault-zone extensive stresses slightly oscillate in magnitude, meanwhile and incrementally, the slabs separate horizontally inside the ambient mantle (right-side panel).

4.3 On the trench-based alternative tearing patterns

In this study we opted to express the tearing horizontal-displacement vector in reference frames defined by the transform-fault-based system in each simulation, case by case depending on the horizontal-obliqueness angle. An interesting alternative is to use a universal (for all the simulations) reference frame, the one that defines the model-box: we shall now express the tearing in the 'universal' trench-based system, with axes X (trench-perpendicular) and Y (trench-parallel) as in Figure 2. This is important as the overriding continental plate with its fixed trench, is a common single entity which all the different simulated systems have and interact with.

In this 'universal' reference frame, the tearing displacement (dx,dy) is used to directly compute the magnitude of the tearing horizontal-components ratio |dx/dy| to characterize the tearing patterns. The values of this ratio tend to be <1 due to the horizontal obliqueness: when the angle θ>0° the "dy" component tends to be non-zero in most cases, but "dx" can be about zero in several cases. When the ratio is <0.5 trench-parallel tearing dominates thoroughly and more than half of the simulations are represented, and when >1 the pattern is trench-perpendicular-dominated but only 1 (in stage 1) and 4 (in stage 2) out of 69 cases were found.

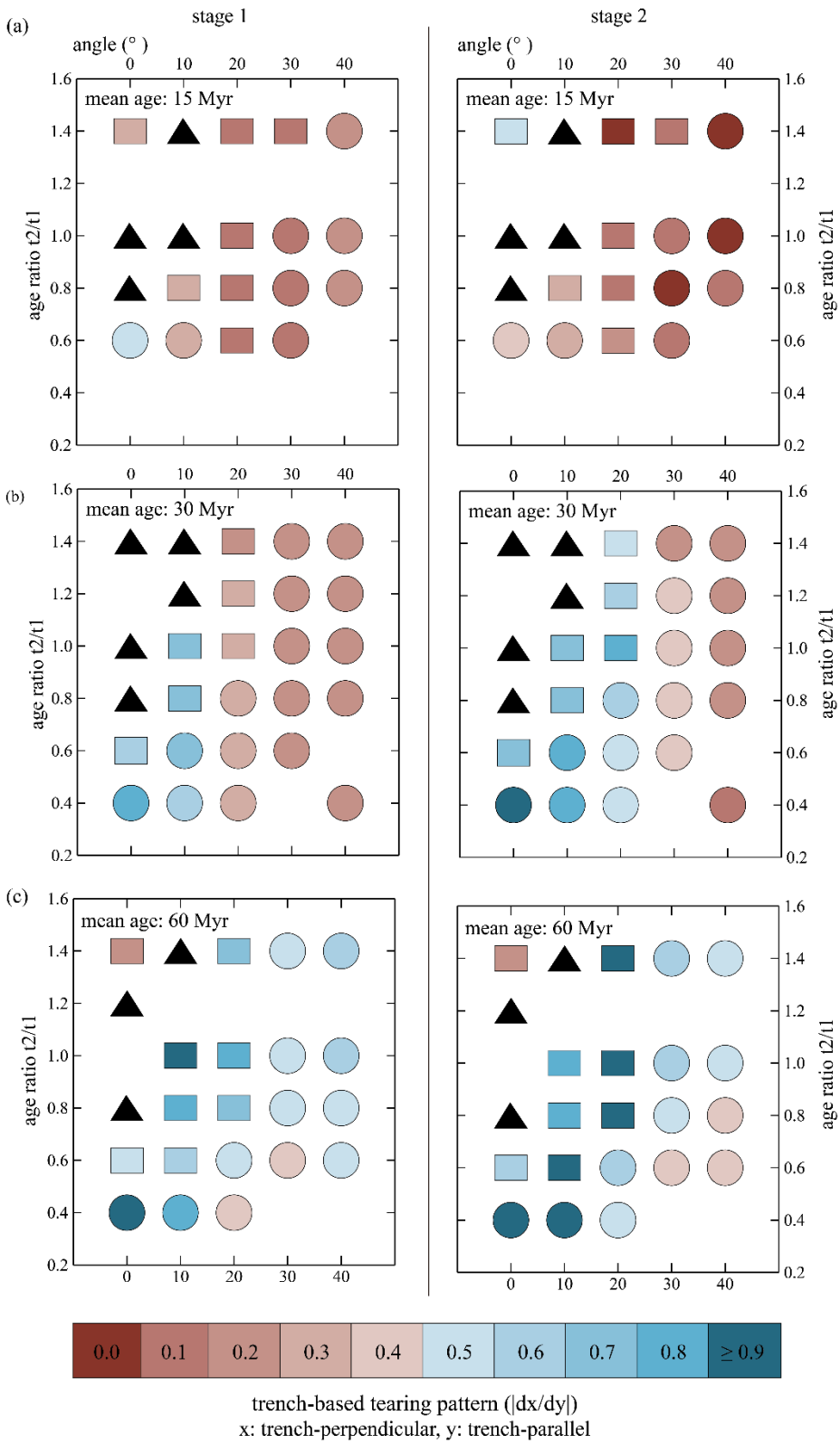

Figure 12. Check-box diagrams for trench-based tearing patterns on time-stages 1 (left) and 2 (right). *Angle* means the slabs' horizontal-obliqueness angle. The arithmetic-mean lithospheric age of plates 1 and 2, $((t_1+t_2)/2)$, is 15 Myr (a), 30 Myr (b), and 60 Myr (c), respectively. The category of slab trench-based tearing pattern, depending on the ratio "$|d_x/d_y|$". Red-color tones: $|d_x/d_y| < 0.5$, contrasting with Blue-color tones: $|d_x/d_y| \geqslant 0.5$.

The trench-based coordinate frame is as shown in Figure 2: X axis (trench-perpendicular), Y axis (trench-parallel). The definition of symbol shapes is the same as in Figure 4. Black triangles are the no-tearing simulations.

Particularly, when the subduction horizontal-obliqueness is zero, the two coordinate-frames coincide, and fault-perpendicular equals trench-parallel. Indeed, observing Figures 5 and 12, we can confirm that for angle θ=0° all the simulations colored in orange in Figure 5 have a ratio<0.7 colored correspondingly in Figure 12, and the only simulation colored blue (ratio >1.3) in Figure 5 is correspondingly colored as >0.9 in Figure 12. For obliqueness θ>0°, the relationship between the patterns from the two coordinate-frames-descriptions is non-trivial, specifically it is non-linear and given by trigonometric projections.

The overall tearing patterns in the trench-based system are the following:

(i) Trench-parallel tearing is mostly a young-slabs at high horizontal-obliqueness phenomenon: There is a clear dominance of ratio values <0.5 (strong trench-parallel tearing displacement) for young-intermediate (15-30 Myr) ages, and being more prevalent for high obliqueness angles but virtually independent of transform-fault age ratios. Aside from this, for young slabs this pattern accentuates with temporal evolution, more prevalent and intense in stage 2 after one slab reaches the bottom; and only slightly more prevalent in late stage for the 60 Myr age group; however, the opposite occurs for mid-age slabs (pattern is more prevalent at early stage).

(ii) The trench-perpendicular tearing-displacement component, being relatively smaller in general, becomes significant only for intermediate-old (30-60 Myr) ages and mostly low horizontal-obliqueness (for the transform-fault-parallel tearing to project effectively on that axis). The components-ratio becomes comparable or larger than unit (ratio ≳1) only in a few simulations (Figure 12). Also, trench-perpendicular tearing component becomes (excepting for two simulations) more important (prevalent and intense) in late times in stage 2, as an effect of one slab reaching the bottom and blocking the motion for some time.

The evident dominance and prevalence of trench-parallel tearing (ratios<0.5), being

common for young slabs' mean ages and high obliqueness angles, is interpreted as: Young ages signify smaller sinking-velocity differences (constructively-combined with older slab-2 preventing excessive vertical separation, in the 15 Myr group only) combined with high obliqueness angles that signify higher trench-parallel relative velocities between slabs and trench, thus higher viscous trench-parallel shear stress on the contact. These conditions, of low vertical velocity-displacement difference between slabs, with high tangential forces on them, may favor the dominance of trench-parallel tearing. On the other hand, the manifestation of trench-perpendicular tearing is more complex, as it not only depends on the time stage, but perhaps on an obvious trade-off: similar constructive-tearing results for low age-ratio (relatively older slab-1) and high obliqueness angle, which can result in non-uniform (differential) rollback and smaller (delayed) bending-length of "apparently stiffer" plate 2, respectively. Finally, as seen in figure 12, the overall temporal change of patterns between stages 1 and 2 is due to one slab reaching the bottom, and the consequential difference in sinking-subducting style that ensues, which affects the slabs tearing displacement.

4.4. Geological application

As shown in Figure 13, examples of slab tearing of natural subduction zones are projected onto our model phase diagrams. Some cases (such as "Central America subduction zone (cam-1)" and "Alaska subduction zone (ala)") occur simultaneously in two mean-age groups, given our sparse and imprecise sampling of this variable. Except for the "Alaska (ala)" point, all the natural cases fall in our model-predicted regime where tearing occurs. The misfit of the "Alaska (ala)" case may be due to a secondary plate with different seafloor ages (Yang & Gao, 2020). Furthermore, because the horizontal-obliqueness angle of "Caribbean (car)" subduction is ≥60°, we have not carried out corresponding simulations considering the numerical stability problems they face. According to our analysis, the Aleutian slab window's low-velocity zone emplaced on a high oblique-convergence angle may undergo tearing due to slab-1 bending enforced by the overriding plate (Bai et al., 2020).

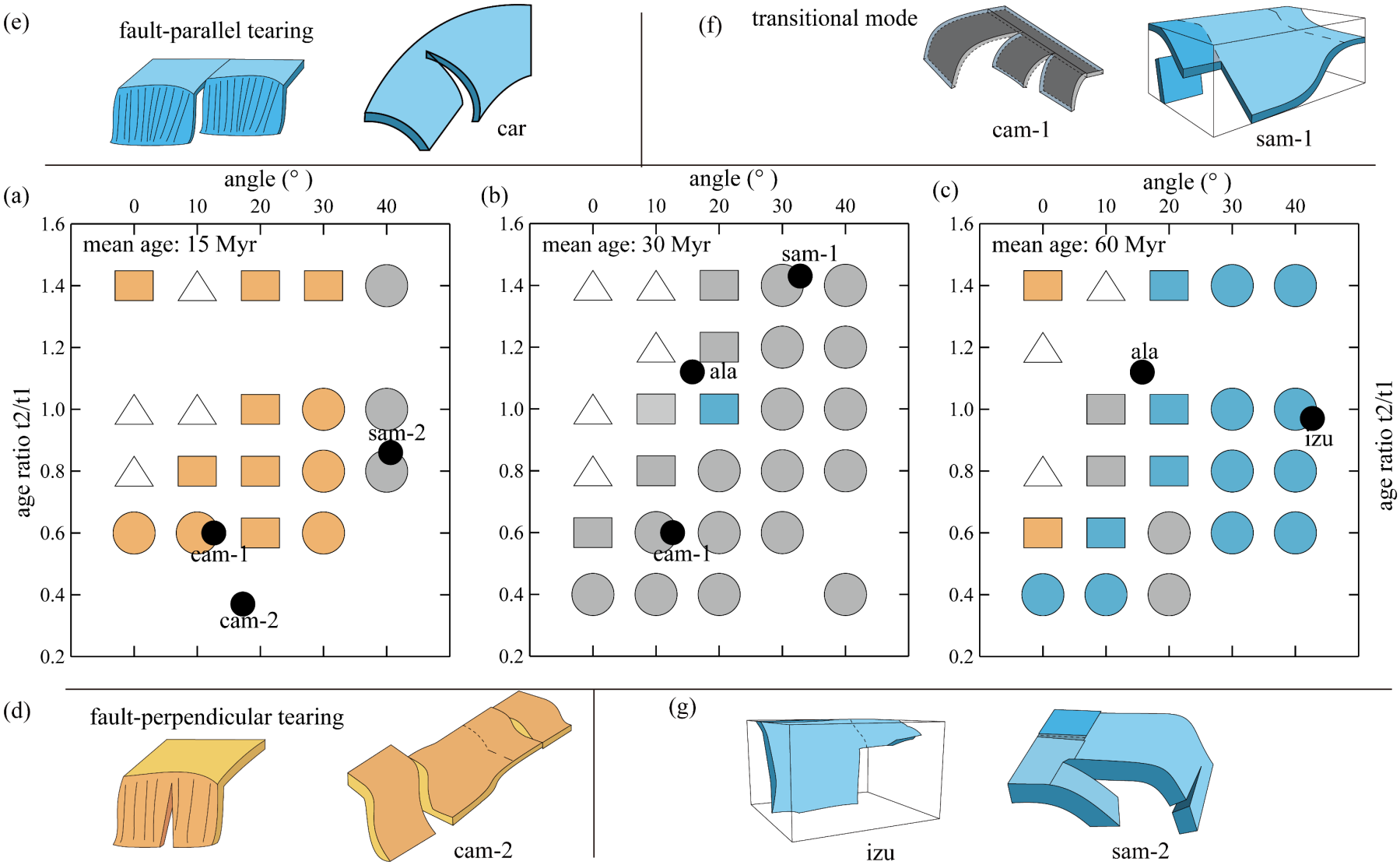
(e)
fault-parallel tearing
car
(f)
transitional mode
cam-1
sam-1
(a)
angle (°)
0
10
20
30
40
mean age: 15 Myr
sam-2
cam-1
cam-2
(b)
mean age: 30 Myr
sam-1
ala
cam-1
(c)
mean age: 60 Myr
ala
izu
age ratio t2/t1
1.6
1.4
1.2
1.0
0.8
0.6
0.4
0.2
(d)
fault-perpendicular tearing
cam-2
(g)
izu
sam-2

Figure 13. Comparisons between our numerical-model predictions on time-stage 2 (phase diagrams color-coded for tearing pattern and shape-coded for overall tearing occurrence) and natural subduction-zones observations (small black circles) along with their simplified observation-based interpreted structures (cartoons). The "Alaska **(ala)**" natural case falling in the predicted no-tearing zone may be affected by a secondary, so far unobserved, slab tear. In contrast, the "South America **(sam-1 and sam-2)** differential retreat" case with a fault-parallel pattern may be affected by a lateral break-off in the younger slab but also lack more detailed local observations. Colored diagram: the same as in Figure 5.

We measured the tear widths observed in the literature. We projected the tearing widths onto the convergence (transform-fault-parallel) direction and its perpendicular direction, which were used to determine the corresponding vertical tearing patterns (Caribbean (car):(Meighan et al., 2013); South America (sam-1):(Pesicek et al., 2012); Central America (cam-1): (Stubailo et al., 2012); Central America (cam-2):(Carciumaru et al., 2020)) (Figure S3). Colored cartoons represent the tearing patterns in nature, and the tearing patterns predicted by the model are represented by colors in the phase diagram (Figure 13).

We find that fault-perpendicular tearing manifests in "Central America (cam-2)", the transitional node manifests in "Central America (cam-1)", and fault-parallel tearing manifests in "Caribbean (car)" and "Izu-Bonin (izu)."

The simulations do not fit the real "South America (sam-1 and sam-2)" tearing pattern, most likely due to the real plate being too thin and experiencing break-off during subduction, as shown in Figure 1 and Table 1, which increases the tearing width in the along-fault direction. According to our understanding, the vertical tearing pattern of "Kamchatka (kam)" is most likely fault-parallel tearing.

In order to investigate whether our model can be applied to other types of subduction, such as "Calabria (cal)" involving ocean-continental transition zone, "Izu-Bonin (izu)" and "South America (sam-2)" involving ridge subduction, we performed six comparative experiments of oblique subduction with/without ocean-continental transition and oblique subduction with/without a ridge (Figure S4, S5). We find that a less-dense continental crust, as expected, causes flat subduction of the slab on that side, thus causing our transform-faulted oceanic slabs model to be inapplicable to the subduction of continental material. For a ridge subduction case, as long as a weak zone exists in front of the ridge, the presence of this latter does not change the vertical tearing results/pattern of the forward slab, indicating that our model can be potentially applied to cases where a weak zone exists in front of the ridge (Figure S6). In addition, we find that when the oceanic ridge is at the front edge of the plate, and the weak zone is behind, its oblique subduction results in a pattern similar to the tearing pattern of the opposite

rotation of slab segments (Gianni et al., 2019) (Figure S6). Details of oblique subduction of a ridge need to be studied further in dedicated future studies.

We also carried out additional simulations altering the viscosity of the weak transform-fault zone and found that a high-enough fault-zone viscosity can (in some cases) preclude and inhibit tearing. However, we must note that when slab-2 is not entirely subducted during the early stages of subduction evolution, the variable slab length l along the trench generates transverse non-uniform slab "stiffness" (Li & Ribe, 2012). In these cases, the deformation results in a continuous variation in subduction dip angle (Figure S7), like the imaging on the right side of "South America (sam-1)" (Figure 1).

4.3. Model limitations

Our model is simplified by having constant (yet adequate) density, viscosity, and thermal properties values. This was chosen to isolate the first-order controls on the slab tearing during transform-fault subduction. This simplification, also applied in order to facilitate the quantitative scaling analysis, may lead to some inaccuracies related to the following:

(1) The age difference between the two sides of the transform fault should lead to additional lateral variations in the oceanic plate's physical properties (e.g., viscosities).

(2) The viscosity and density should vary continuously with depth (pressure and temperature), particularly through and between lithospheric and asthenospheric mantle regions.

(3) Additional complexities and effects on the sinking-tearing plate, i.e., more specific and refined forms of the post-factor function f, were not tried.

(4) The obliqueness angle and age-ratio in the natural cases may have changed through time. Therefore, their values during the early stages of subduction (Myr ago) may differ from those observed at the present day.

All the aforementioned neglected factors/processes can influence the slabs' tearing vector (magnitude and direction) at all stages during subduction. However, we believe that the first-order controlling mechanisms are adequately represented in our study.

5. Conclusions

Subduction horizontal obliqueness and slabs' transform-fault age-offset play dominant first-order roles in the development and evolution of slabs tearing during the subduction of such complex systems. The viscous unbending resistance varies among the two subducting slabs during the subduction process, and also varies among different subduction zones, yet it seems to only have a secondary role in slab tearing.

When the subduction horizontal-obliqueness angle is ≥30° or the age ratio of slab-2 to slab-1 is less than 0.6, fast and well-developed oceanic plate vertical tearing occurs and develops inside the mantle without any other requirements. In contrast, no tearing occurs for small obliqueness angles (<20°) if slab-2 is approximately older and thicker (age ratio >0.6-0.8).

The vector nature of slab tearing can occur/be decomposed in two patterns or modes when referred to the convergence direction or transform-fault orientation: fault-parallel and fault-perpendicular tearing. Fault-perpendicular tearing manifests mostly (not solely) in young-age slabs and for medium-low subduction horizontal-obliqueness angles (≤30°) and somewhat more favorably for low-age ratios (slab-1 being older). Fault-parallel tearing (related to differential slabs-hinge retreat or rollback) is relatively well-known and manifests almost solely for old-age slabs (60 Myr-mean-age group) and mostly for medium-high obliqueness (~>20°) angles but almost independently of age ratios.

Transform-fault-perpendicular tearing of subducting slabs' is here kinematically identified fairly/slightly above numerical errors and model uncertainties, and classified in a parametric way using the tearing horizontal-distance vector. Dynamically speaking, some of our simulations suggest that this tearing mode is accompanied by viscous horizontal normal deviatoric stresses of extension across the weak fault-zone, in-and-around the hinge (subduction bent) region, with some slight variations in time; all of this concomitant to the slabs' increasing horizontal separation inside the ambient mantle. Future research is needed to better understand this particular tearing behavior, but hereby we have provided a first step in that direction.

Compared to the several transform-fault-based systems in our simulations, the universal trench-based reference frame is defined by a single common entity (overriding plate), and when the slabs' horizontal-obliqueness angle is 0° (normal subduction) the two reference frames coincide. Trench-parallel tearing is frequent and dominant for young slabs, and may be caused by low vertical-velocity difference between slabs, and moving at high horizontal-obliqueness angles (~>20°) causing high tangential shear stress at the trench. Trench-perpendicular tearing is relatively infrequent and likely an old-age phenomenon (~>30 Myr), favored by mid-low obliqueness angles, and closely related to non-uniform slabs rollback.

Our modeling suggests that the continual spatial variation in dip angle along the trench observed in real-Earth subduction zones could be potentially related to the initial evolution of subducting slabs under horizontally-oblique convergence. Further beyond, knowing the age combination across a transform fault (ratio and average) and the horizontal obliqueness of an oceanic subduction scenario would, with a framework like the one here presented, allow a prediction of the tearing occurrence, potential pattern, and the likely evolution of the subducting slabs, and perhaps of the associated locally-perturbed mantle flow.

Acknowledgments

We appreciate Dr. Yimin Jin's great help in troubleshooting-running the ASPECT software. We appreciate comments on the article from anonymous reviewers. We thank National Supercomputing Center in Chengdu, China, for the support during the parallel computing lengthy tasks. This research is supported by the National Science Foundation of China (U2239205, 41725017) and the National Key R&D Program of the Ministry of Science and Technology of China (2020YFA0713401). It is also partially supported by the National Key Scientific and Technological Infrastructure project "Earth System Science Numerical Simulator Facility" (EarthLab).

The original datasets are published as a Zenodo data package (https://zenodo.org/record/7898295#.ZFSf6XZByUk). The numerical software ASPECT (version 2.3.0) is from

https://github.com/geodynamics/aspect/releases/tag/v2.3.0, and the visualization software ParaView is https://www.paraview.org/. Figure 1 is plotted with GMT https://www.generic-mapping-tools.org/, and the original data on the subduction zone, seafloor age, plate velocity, and color bar is referred to (Hayes et al., 2018)(Müller et al., 2008)(Becker et al., 2015)(Crameri, 2021), respectively.

References

Bai, Y., Zhang, D., Dong, D., Wu, S., & Wang, Z. (2020). Aleutian island arc magma production rates and primary controlling factors. *Marine Geology*, *430*, 106346. https://doi.org/10.1016/j.margeo.2020.106346

Bangerth, W., Dannberg, J., Fraters, M., Gassmoeller, R., Glerum, A., Heister, T., & Naliboff, J. (2021). *ASPECT v2.3.0*. Zenodo. https://doi.org/10.5281/zenodo.5131909

Becker, T. W., Schaeffer, A. J., Lebedev, S., & Conrad, C. P. (2015). Toward a generalized plate motion reference frame. *Geophysical Research Letters*, *42*(9), 3188–3196. https://doi.org/10.1002/2015GL063695

Bolton, A. R., Schutt, D. L., Aster, R. C., Audet, P., Schaeffer, A. J., Estève, C., et al. (2022). Evidence for asthenospheric flow rotation in northwest Canada: insights from shear wave splitting. *Geophysical Journal International*, *228*(3), 1780–1792. https://doi.org/10.1093/gji/ggab396

Bonnardot, M.-A., Régnier, M., Christova, C., Ruellan, E., & Tric, E. (2009). Seismological evidence for a slab detachment in the Tonga subduction zone. *Tectonophysics*, *464*(1), 84–99. https://doi.org/10.1016/j.tecto.2008.10.011

Burkett, E. R., & Billen, M. I. (2010). Three-dimensionality of slab detachment due to ridge-trench collision: Laterally simultaneous boudinage versus tear propagation. *Geochemistry, Geophysics, Geosystems*, *11*(11). https://doi.org/10.1029/2010GC003286

Carciumaru, D., Ortega, R., Castellanos, J. C., & Huesca-Pérez, E. (2020). Crustal Characteristics in the Subduction Zone of Mexico: Implication of the Tectonostratigraphic Terranes on Slab Tearing. *Seismological Research Letters*,

91(3), 1781–1793. https://doi.org/10.1785/0220190117

Crameri, F. (2021). *Scientific colour maps*. Zenodo. https://doi.org/10.5281/zenodo.5501399

Cui, Q., & Li, Z.-H. (2022). Along-Strike Variation of Convergence Rate and Pre-Existing Weakness Contribute to Indian Slab Tearing Beneath Tibetan Plateau. *Geophysical Research Letters*, *49*(4), e2022GL098019. https://doi.org/10.1029/2022GL098019

Dougherty, S. L., & Clayton, R. W. (2014). Seismicity and structure in central Mexico: Evidence for a possible slab tear in the South Cocos plate. *Journal of Geophysical Research: Solid Earth*, *119*(4), 3424–3447. https://doi.org/10.1002/2013JB010883

Duretz, T., Gerya, T. V., & May, D. A. (2011). Numerical modelling of spontaneous slab breakoff and subsequent topographic response. *Tectonophysics*, *502*(1), 244–256. https://doi.org/10.1016/j.tecto.2010.05.024

Fernández-García, C., Guillaume, B., & Brun, J.-P. (2019). 3D slab breakoff in laboratory experiments. *Tectonophysics*, *773*, 228223. https://doi.org/10.1016/j.tecto.2019.228223

Freeburn, R., Bouilhol, P., Maunder, B., Magni, V., & van Hunen, J. (2017). Numerical models of the magmatic processes induced by slab breakoff. *Earth and Planetary Science Letters*, *478*, 203–213. https://doi.org/10.1016/j.epsl.2017.09.008

Georgieva, V., Melnick, D., Schildgen, T. F., Ehlers, T. A., Lagabrielle, Y., Enkelmann, E., & Strecker, M. R. (2016). Tectonic control on rock uplift, exhumation, and topography above an oceanic ridge collision: Southern Patagonian Andes (47°S), Chile. *Tectonics*, *35*(6), 1317–1341. https://doi.org/10.1002/2016TC004120

Gerya, T. (2022). Numerical modeling of subduction: State of the art and future directions. *Geosphere*, *18*(2), 503–561. https://doi.org/10.1130/GES02416.1

Gianni, G. M., & Luján, S. P. (2021). Geodynamic controls on magmatic arc migration and quiescence. *Earth-Science Reviews*, *218*, 103676. https://doi.org/10.1016/j.earscirev.2021.103676

Gianni, G. M., Navarrete, C., & Spagnotto, S. (2019). Surface and mantle records reveal an ancient slab tear beneath Gondwana. *Scientific Reports*, *9*(1), 19774. https://doi.org/10.1038/s41598-019-56335-9

Glerum, A., Thieulot, C., Fraters, M., Blom, C., & Spakman, W. (2018). Nonlinear viscoplasticity in ASPECT: benchmarking and applications to subduction. *Solid Earth*, *9*(2), 267–294. https://doi.org/10.5194/se-9-267-2018

Govers, R., & Wortel, M. J. R. (2005). Lithosphere tearing at STEP faults: response to edges of subduction zones. *Earth and Planetary Science Letters*, *236*(1), 505–523. https://doi.org/10.1016/j.epsl.2005.03.022

Govers, Rob, & Fichtner, A. (2016). Signature of slab fragmentation beneath Anatolia from full-waveform tomography. *Earth and Planetary Science Letters*, *450*, 10–19. https://doi.org/10.1016/j.epsl.2016.06.014

Guillaume, B., Moroni, M., Funiciello, F., Martinod, J., & Faccenna, C. (2010). Mantle flow and dynamic topography associated with slab window opening: Insights from laboratory models. *Tectonophysics*, *496*(1), 83–98. https://doi.org/10.1016/j.tecto.2010.10.014

Hayes, G. P., Moore, G. L., Portner, D. E., Hearne, M., Flamme, H., Furtney, M., & Smoczyk, G. M. (2018). Slab2, a comprehensive subduction zone geometry model. *Science*. https://doi.org/10.1126/science.aat4723

Hildebrand, R. S., Whalen, J. B., & Bowring, S. A. (2018). Resolving the crustal composition paradox by 3.8 billion years of slab failure magmatism and collisional recycling of continental crust. *Tectonophysics*, *734–735*, 69–88. https://doi.org/10.1016/j.tecto.2018.04.001

Jolivet, L., Menant, A., Sternai, P., Rabillard, A., Arbaret, L., Augier, R., et al. (2015). The geological signature of a slab tear below the Aegean. *Tectonophysics*, *659*, 166–182. https://doi.org/10.1016/j.tecto.2015.08.004

Jolivet, L., Menant, A., Roche, V., Pourhiet, L. L., Maillard, A., Augier, R., et al. (2021). Transfer zones in Mediterranean back-arc regions and tear faults. *BSGF - Earth Sciences Bulletin*, *192*, 11. https://doi.org/10.1051/bsgf/2021006

Király, Á., Portner, D. E., Haynie, K. L., Chilson-Parks, B. H., Ghosh, T., Jadamec, M.,

et al. (2020). The effect of slab gaps on subduction dynamics and mantle upwelling. *Tectonophysics*, *785*, 228458. https://doi.org/10.1016/j.tecto.2020.228458

Kufner, S.-K., Schurr, B., Haberland, C., Zhang, Y., Saul, J., Ischuk, A., & Oimahmadov, I. (2017). Zooming into the Hindu Kush slab break-off: A rare glimpse on the terminal stage of subduction. *Earth and Planetary Science Letters*, *461*, 127–140. https://doi.org/10.1016/j.epsl.2016.12.043

Levin, V., Shapiro, N., Park, J., & Ritzwoller, M. (2002). Seismic evidence for catastrophic slab loss beneath Kamchatka. *Nature*, *418*(6899), 763–767. https://doi.org/10.1038/nature00973

Li, Z.-H., & Ribe, N. M. (2012). Dynamics of free subduction from 3-D boundary element modeling. *Journal of Geophysical Research: Solid Earth*, *117*(B6). https://doi.org/10.1029/2012JB009165

Li, Z.-H., Xu, Z., Gerya, T., & Burg, J.-P. (2013). Collision of continental corner from 3-D numerical modeling. *Earth and Planetary Science Letters*, *380*, 98–111. https://doi.org/10.1016/j.epsl.2013.08.034

Liu, K., Zhang, J., Xiao, W., Wilde, S. A., & Alexandrov, I. (2020). A review of magmatism and deformation history along the NE Asian margin from ca. 95 to 30 Ma: Transition from the Izanagi to Pacific plate subduction in the early Cenozoic. *Earth-Science Reviews*, *209*, 103317. https://doi.org/10.1016/j.earscirev.2020.103317

Liu, L., Liu, L., & Xu, Y.-G. (2021). Mesozoic intraplate tectonism of East Asia due to flat subduction of a composite terrane slab. *Earth-Science Reviews*, *214*, 103505. https://doi.org/10.1016/j.earscirev.2021.103505

Magni, V., Faccenna, C., van Hunen, J., & Funiciello, F. (2014). How collision triggers backarc extension: Insight into Mediterranean style of extension from 3-D numerical models. *Geology*, *42*(6), 511–514. https://doi.org/10.1130/G35446.1

Meighan, H. E., Pulliam, J., Brink, U. ten, & López-Venegas, A. M. (2013). Seismic evidence for a slab tear at the Puerto Rico Trench. *Journal of Geophysical Research: Solid Earth*, *118*(6), 2915–2923. https://doi.org/10.1002/jgrb.50227

Miller, M. S., Kennett, B. L. N., & Lister, G. S. (2004). Imaging changes in morphology, geometry, and physical properties of the subducting Pacific plate along the Izu–Bonin–Mariana arc. *Earth and Planetary Science Letters*, *224*(3), 363–370. https://doi.org/10.1016/j.epsl.2004.05.018

Miller, Meghan S., Gorbatov, A., & Kennett, B. L. N. (2006). Three-dimensional visualization of a near-vertical slab tear beneath the southern Mariana arc. *Geochemistry, Geophysics, Geosystems*, *7*(6). https://doi.org/10.1029/2005GC001110

Müller, R. D., Sdrolias, M., Gaina, C., & Roest, W. R. (2008). Age, spreading rates, and spreading asymmetry of the world's ocean crust. *Geochemistry, Geophysics, Geosystems*, *9*(4). https://doi.org/10.1029/2007GC001743

Pesicek, J. D., Engdahl, E. R., Thurber, C. H., DeShon, H. R., & Lange, D. (2012). Mantle subducting slab structure in the region of the 2010 M8.8 Maule earthquake (30–40°S), Chile. *Geophysical Journal International*, *191*(1), 317–324. https://doi.org/10.1111/j.1365-246X.2012.05624.x

Pusok, A. E., Kaus, B. J. P., & Popov, A. A. (2018). The effect of rheological approximations in 3-D numerical simulations of subduction and collision. *Tectonophysics*, *746*, 296–311. https://doi.org/10.1016/j.tecto.2018.04.017

Ribe, N. M. (2001). Bending and stretching of thin viscous sheets. *Journal of Fluid Mechanics*, *433*, 135–160. https://doi.org/10.1017/S0022112000003360

Roche, V., Sternai, P., Guillou-Frottier, L., Menant, A., Jolivet, L., Bouchot, V., & Gerya, T. (2018). Emplacement of metamorphic core complexes and associated geothermal systems controlled by slab dynamics. *Earth and Planetary Science Letters*, *498*, 322–333. https://doi.org/10.1016/j.epsl.2018.06.043

Rosenbaum, G., Gasparon, M., Lucente, F. P., Peccerillo, A., & Miller, M. S. (2008). Kinematics of slab tear faults during subduction segmentation and implications for Italian magmatism. *Tectonics*, *27*(2). https://doi.org/10.1029/2007TC002143

Schubert, G., Turcotte, D. L., & Olson, P. (2001). *Mantle Convection in the Earth and Planets* (1st ed.). Cambridge University Press.

https://doi.org/10.1017/CBO9780511612879

Stubailo, I., Beghein, C., & Davis, P. M. (2012). Structure and anisotropy of the Mexico subduction zone based on Rayleigh-wave analysis and implications for the geometry of the Trans-Mexican Volcanic Belt. *Journal of Geophysical Research: Solid Earth*, *117*(B5). https://doi.org/10.1029/2011JB008631

Suckale, J., Rondenay, S., Sachpazi, M., Charalampakis, M., Hosa, A., & Royden, L. H. (2009). High-resolution seismic imaging of the western Hellenic subduction zone using teleseismic scattered waves. *Geophysical Journal International*, *178*(2), 775–791. https://doi.org/10.1111/j.1365-246X.2009.04170.x

Thorkelson, D. J. (1996). Subduction of diverging plates and the principles of slab window formation. *Tectonophysics*, *255*(1), 47–63. https://doi.org/10.1016/0040-1951(95)00106-9

Turcotte, D. L., & Schubert, G. (2002). *Geodynamics* (2nd ed.). Cambridge University Press. https://doi.org/10.1017/CBO9780511807442

Vargas, C. A., & Mann, P. (2013). Tearing and Breaking Off of Subducted Slabs as the Result of Collision of the Panama Arc-Indenter with Northwestern South America. *Bulletin of the Seismological Society of America*, *103*(3), 2025–2046. https://doi.org/10.1785/0120120328

Xu, Y., Wang, Q., Tang, G., Wang, J., Li, H., Zhou, J., et al. (2020). The origin of arc basalts: New advances and remaining questions. *Science China Earth Sciences*, *63*(12), 1969–1991. https://doi.org/10.1007/s11430-020-9675-y

Yang, X., & Gao, H. (2020). Segmentation of the Aleutian-Alaska Subduction Zone Revealed by Full-Wave Ambient Noise Tomography: Implications for the Along-Strike Variation of Volcanism. *Journal of Geophysical Research: Solid Earth*, *125*(11), e2020JB019677. https://doi.org/10.1029/2020JB019677

Dynamics of oceanic slab tearing during transform-fault oblique subduction: Insights from 3D numerical modeling

Supporting Information

Jie Xin[1], Huai Zhang[1,4,5,*], Felipe Orellana-Rovirosa[2], Zhong-Hai Li[1], Liang Liu[3], Yi-Gang Xu[3], Zhen Zhang[1], Yaolin Shi[1]

[1]Key Laboratory of Computational Geodynamics, College of Earth and Planetary Sciences, University of Chinese Academy of Sciences, Beijing 100049, China

[2]Department of Ocean Science and Engineering, Southern University of Science and Technology, Shenzhen 518055, China

[3]State Key Laboratory of Isotope Geochemistry, Guangzhou Institute of Geochemistry, Chinese Academy of Sciences, Guangzhou 510640, China

[4]Beijing Yanshan Earth Critical Zone National Research Station, University of Chinese Academy of Sciences, Beijing 101408, China

[5]Southern Marine Science and Engineering Guangdong Laboratory (Zhuhai), Guangdong Zhuhai 519080, China

1. Additional figures

Figure S1-S2 is the stress distribution about fault-perpendicular tearing in text section 4.2.

Figure S3 shows the measured tearing widths from the literature, which we use to denote the observed tearing patterns from each of the four natural cases associated with transform-fault subduction.

Figure S4 to S6 show the results of three experiments for oblique subduction with/without oceanic ridges/seafloor plateau from two cases, “izu” and “sam-2”, respectively. Figure S4-S5 indicate that our model can be applied to the type of subduction where a weak zone exists in front of the oceanic ridge. The presence of stiffer oceanic ridges does not change the tearing results of the forward segment and may correspond to the phenomenon mentioned in the literature (Miller et al., 2006; Vargas & Mann, 2013).

Figure S6 shows the difference between the oceanic ridge/seafloor plateau located in the anterior and posterior segments of the plate. When it is located in the anterior segment, the model results obtained are similar to the pattern of opposite rotation of slab segments mentioned in the previous literature (Gianni et al., 2019).

Figure S7 shows the results of two sets of models varying the viscosity of the entire transform-fault zone (3327_20, 2535_30). The viscosity of the fault increases from top to bottom, and it is found that when the viscosity is too high, no vertical tearing can be produced. However, the plate morphology is consistent with the continuous lateral variation in subduction dip angle seen in observations, such as the plate morphology

shown in the right area of sam-1.

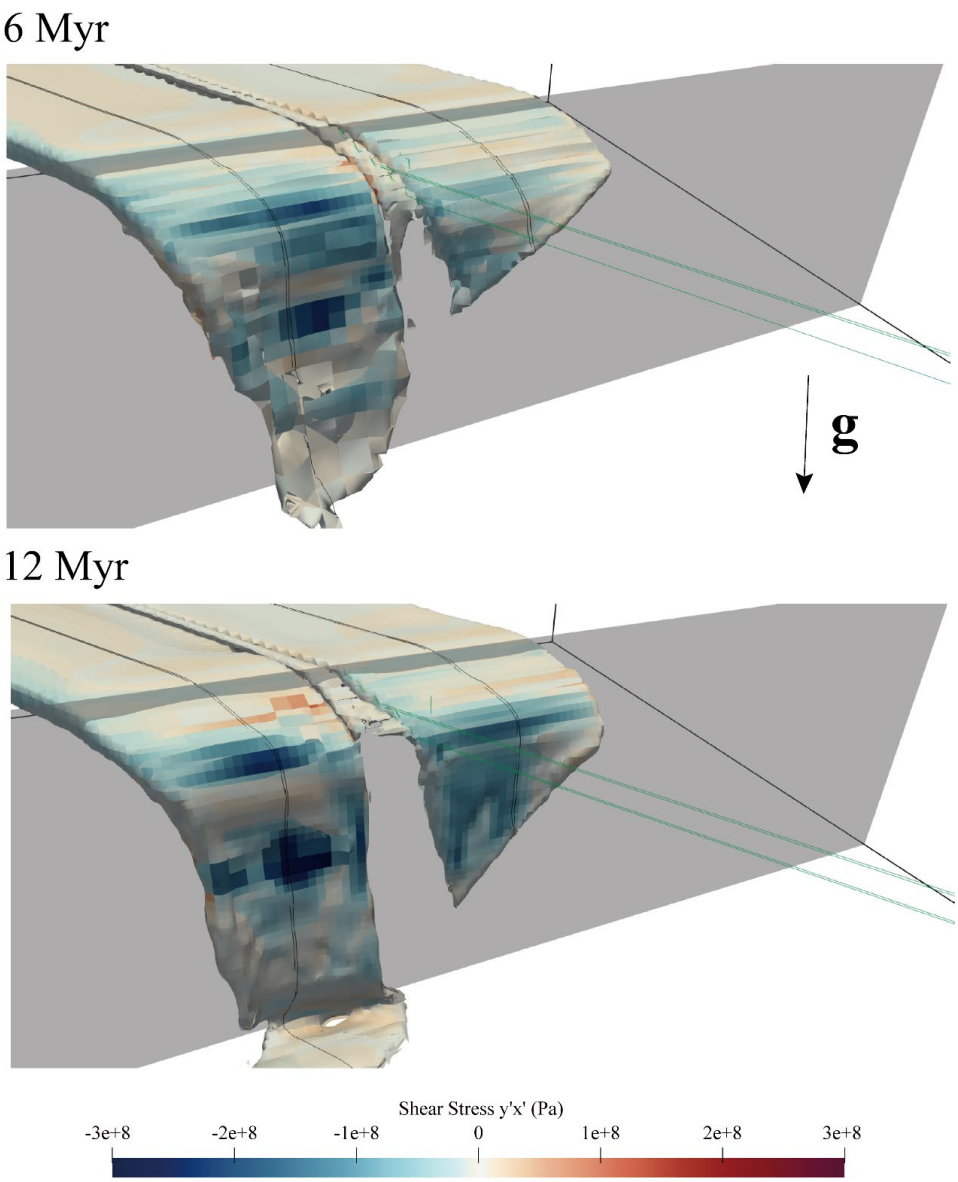

Figure S1. Viscous horizontal shear stress on the slabs' surface for simulation 1713_30 (lithospheric ages t_1 = 17 Ma, t_2 =13 Ma; horizontal obliqueness θ = 30°) which exemplifies transform-fault-perpendicular tearing. The shear stress $\sigma_{y'x'}$ (the x', y' axes are transform-fault -parallel and -perpendicular, respectively) is shown at 6 and 12 Myr of computed geological time. Given the horizontal-obliqueness angle θ=30°, the relative motion between slabs and continental plate dictates the local stress field on the surface of these bodies, in particular the viscous tangential friction.

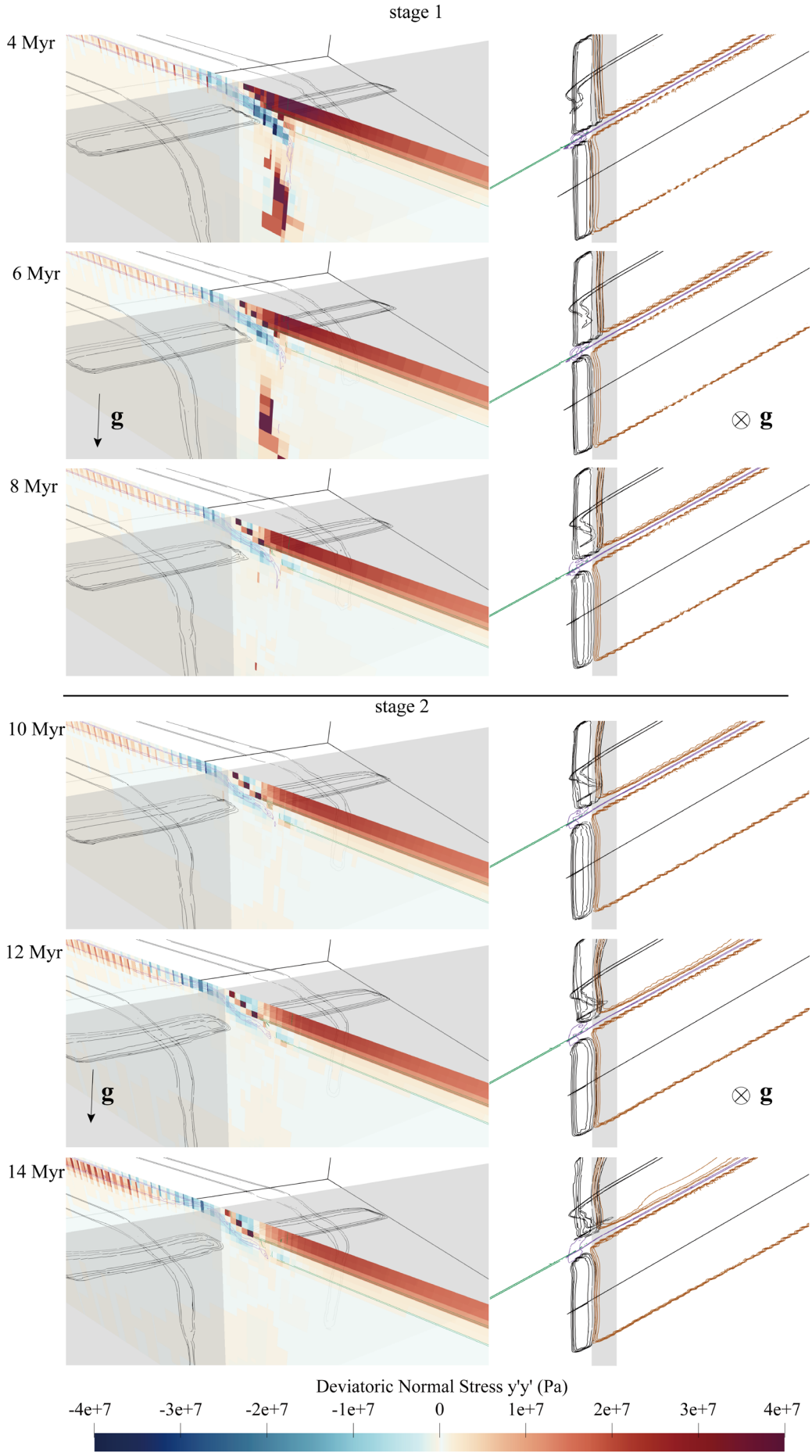
stage 1
4 Myr
6 Myr
g
g
8 Myr
stage 2
10 Myr
12 Myr
g
g
14 Myr
Deviatoric Normal Stress y'y' (Pa)
-4e+7
-3e+7
-2e+7
-1e+7
0
1e+7
2e+7
3e+7
4e+7

Figure S2. Exemplary of transform-fault-perpendicular tearing: simulation 1713_30 evolution snapshots at {4, 6, 8, 10, 12, 14 } Myr of computed time. **(Left-side column panel) Oblique views**: Viscous horizontal deviatoric normal stress ($\sigma_{y'y'}$, with the y' axis the transform-fault-perpendicular) on a 2D vertical slice along the transform-fault-zone axis. Black contours show parallel vertical slices on the two slabs central axes plus a horizontal-slice contour at 60 km depth. **(Right-side column panel) Views from above**: Composition contours at different depths (Brown: 20 km for horizontal portion of slabs; Black: 60 km for subducting portion of slabs). Gray color band: trench position. For both column panels: Transform-fault central axis has been colored purple, but extended (for reference) towards the continent in green color. The normal deviatoric stress $\sigma_{y'y'}$ (left-side panel) inside the transform-fault-zone is extensive in-and-around the subduction hinge (bent), and slightly compressive where the slabs are close to each other in the horizontal portions. With time, the extensive stresses change only slightly (decrease and increase), meanwhile the slabs separate horizontally inside the ambient mantle (right-side panel).

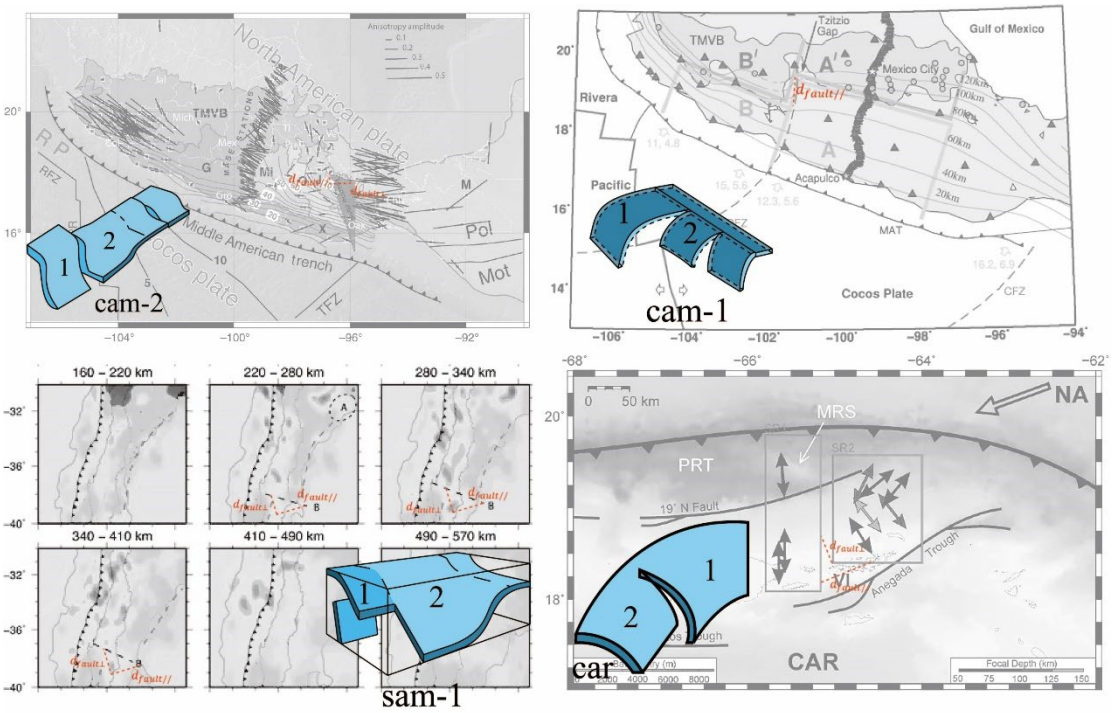

Figure S3. Oceanic plate tearing width from literature. $d_{fault//}$: tearing width along convergence/transform fault direction, $d_{fault\perp}$: tearing width perpendicular to fault direction. Caribbean (car):(Meighan et al., 2013); South America (sam-1):(Pesicek et al., 2012); Central America (cam-1): (Stubailo et al., 2012); Central America (cam-2):(Carciumaru et al., 2020).

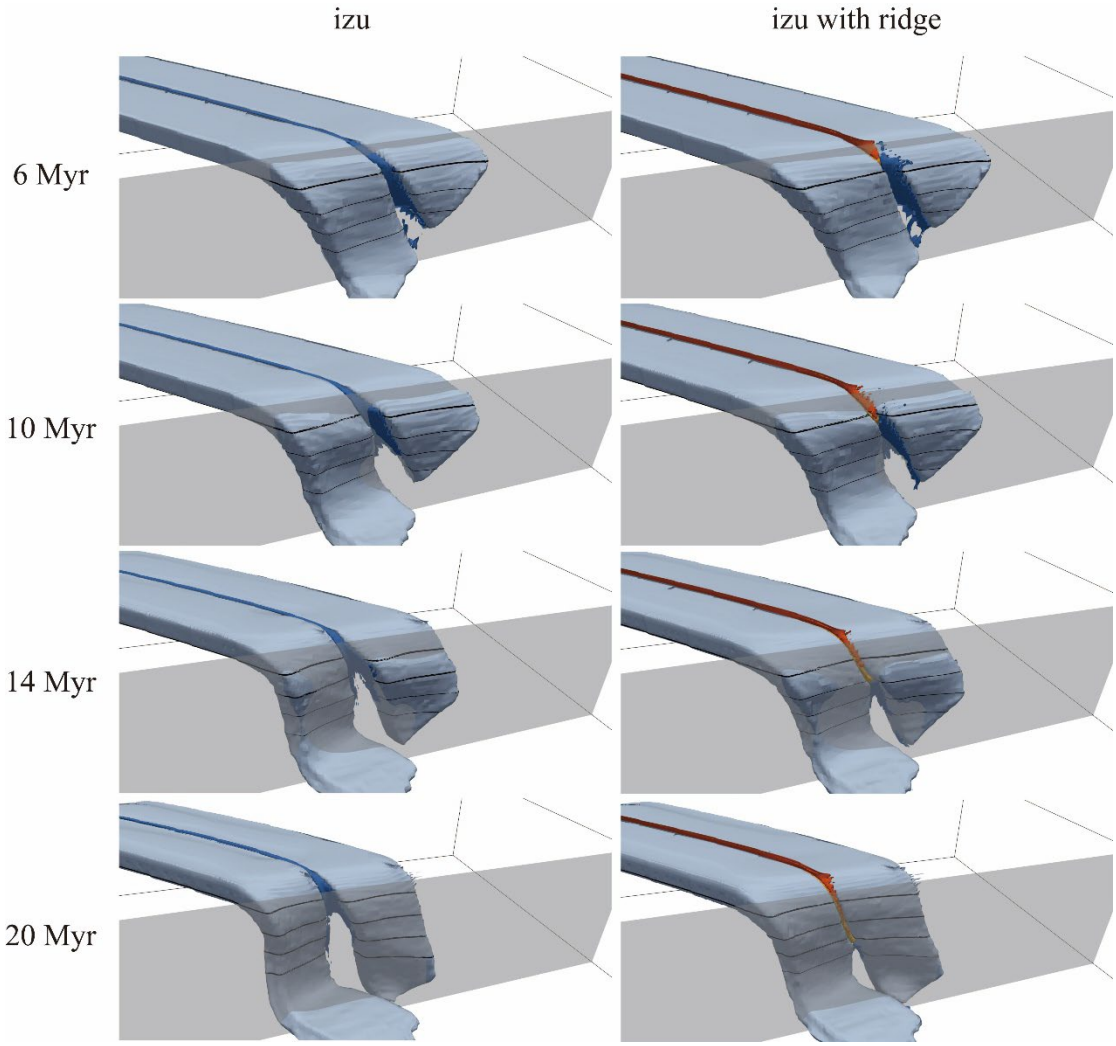

Figure S4. Tearing evolution of izu without a ridge (left) and with a ridge (right). Light blue: oceanic lithosphere, dark blue: weak zone (transform-fault), red: ridge crust, yellow: ridge mantle.

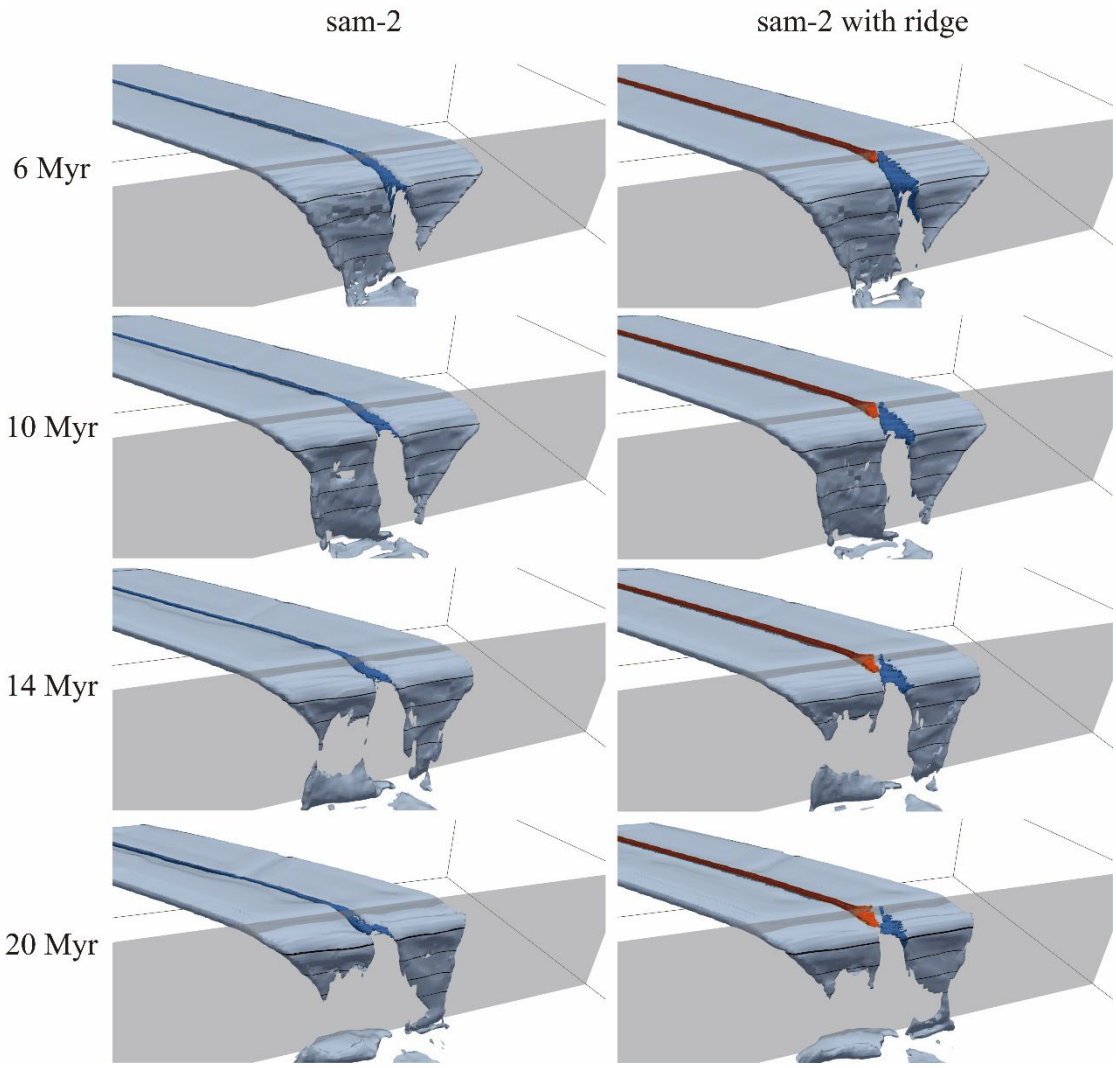

Figure S5. Oceanic plate tearing evolution of sam-2 without a ridge (left) and with a ridge (right). Light blue is the oceanic lithosphere. Dark blue is the weak zone (transform-fault), red is the ridge crust, and yellow is the ridge mantle.

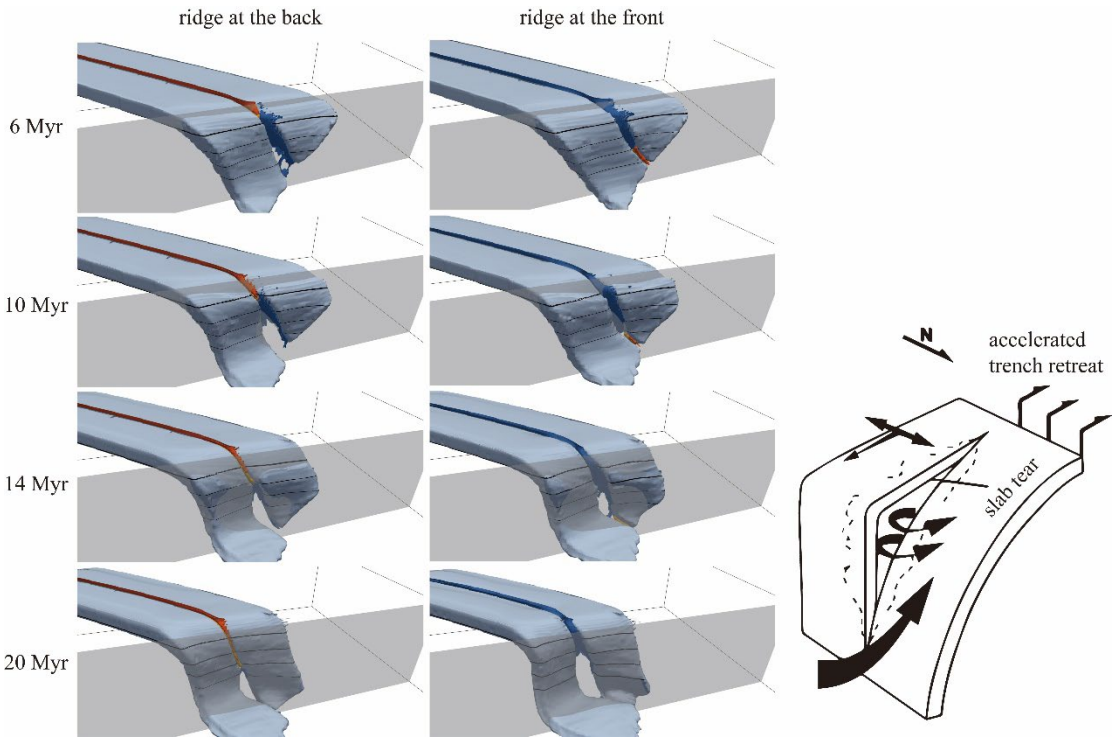

Figure S6. Oceanic plate tearing evolution of ridge at the plate's back segment (left) and the front segment of the plate (right). Light blue: oceanic lithosphere, dark blue: weak zone (transform-fault), red: ridge crust, yellow: ridge mantle. The latter is similar to the tearing phenomenon shown in the lower right cartoon. (Gianni et al., 2019).

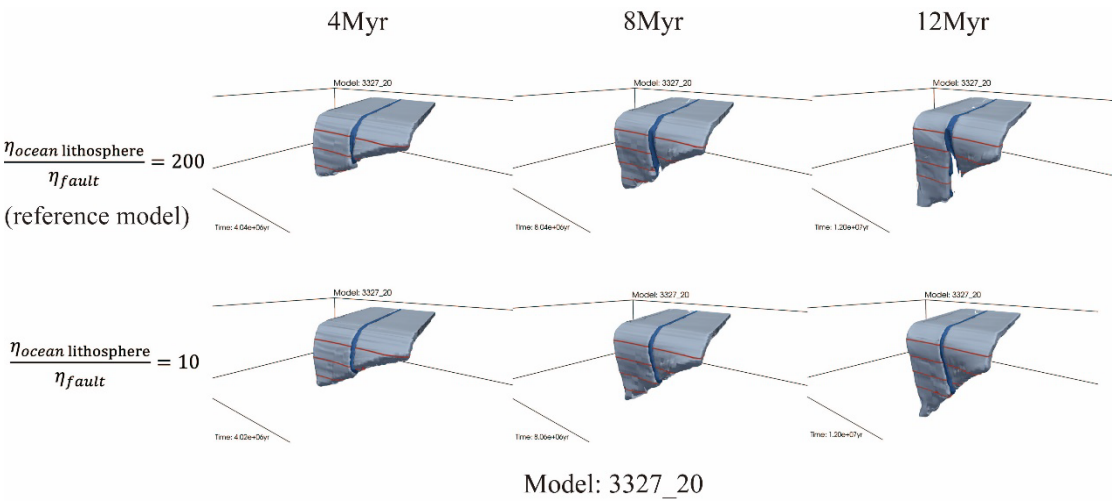

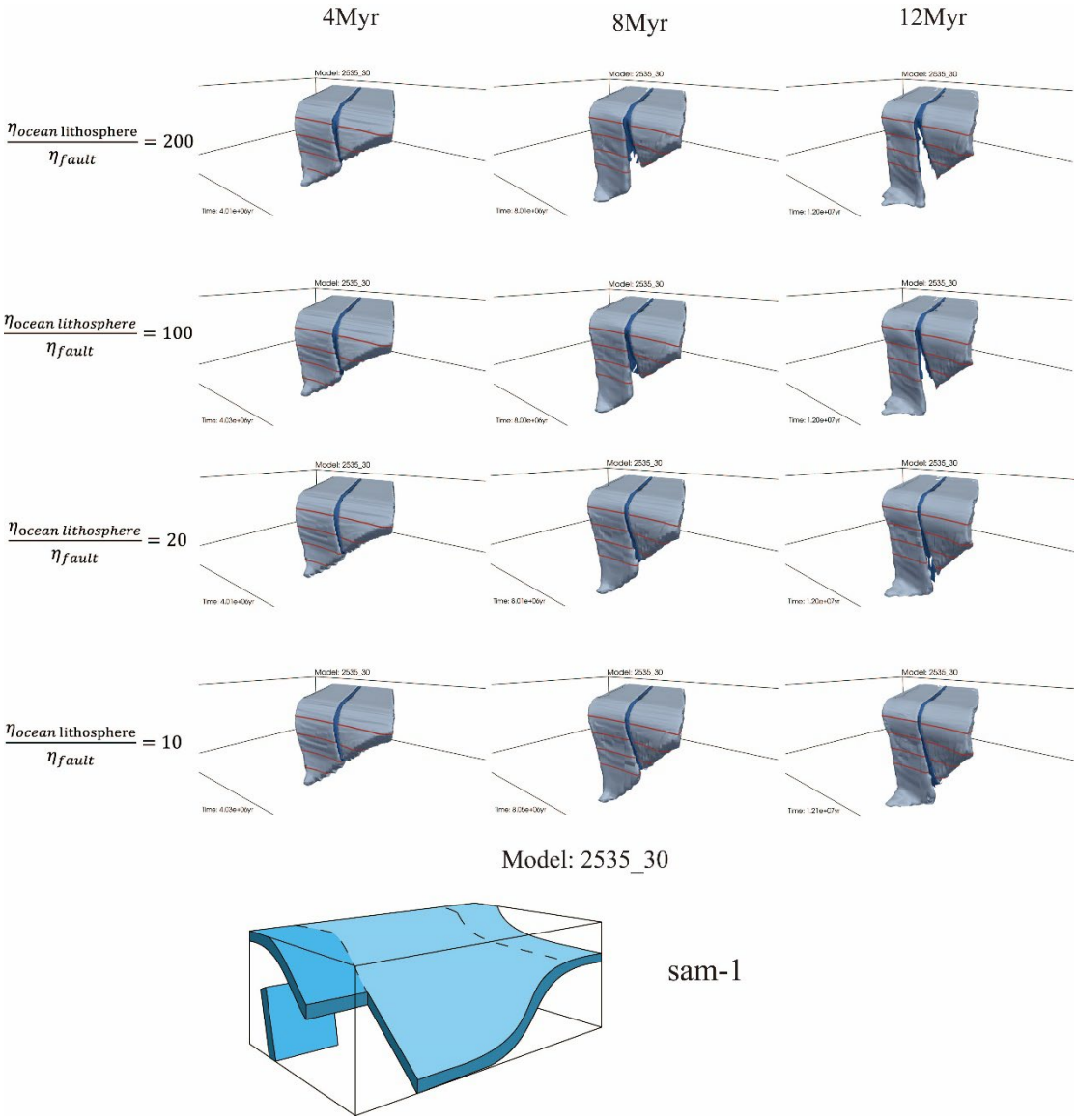

Figure S7. The effect of fault viscosity on tearing. The high viscosity results in a phenomenon similar to the continuous variation of the subduction dip angle along the trench direction (as shown on the right side of the sam-1 cartoon (Pesicek et al., 2012)).

2. Original computed data of tearing widths and tearing patterns

Table S1-S4 shows the specific values for the two stages involved in the tearing width (displacement magnitude) of text Figure 4 and the transform-fault-based tearing pattern of article Figure 5. Table S5-S6 are trench-based tearing pattern of the two time-stages. Table S7 shows the specific values for the tear widths in Figure S3.

Table S1. Tearing width of stage 1 [a]. (unit: km)

	0°	**10°**	**20°**	**30°**	**40°**
1.4(1318)	63	31	83	55	94

1.2					
1.0(1515)	51	40	87	92	100
0.8(1713)	38	76	72	105	84
0.6(1911)	80	88	73	89	
1.4(2535)	48	45	69	96	108
1.2(2733)		48	76	95	108
1.0(3030)	30	72	81	95	115
0.8(3327)	37	79	89	107	145
0.6(3823)	59	102	101	127	
0.4(4317)	153	154	121		124
1.4(5070)	70	45	67	83	71
1.2(5565)	45				
1.0(6060)		57	69	85	74
0.8(6753)	39	66	78	88	74
0.6(7545)	63	78	91	102	79
0.4(8634)	68	99	102		

[a] Original data of Figure 4.

Table S2. Tearing width of stage 2 [a]. (unit: km)

	0°	**10°**	**20°**	**30°**	**40°**
1.4(1318)	70	55	81	95	117
1.2					
1.0(1515)	33	35	55	104	132
0.8(1713)	48	77	83	108	151
0.6(1911)	104	119	96	109	
1.4(2535)	52	62	79	126	176
1.2(2733)		40	81	101	162
1.0(3030)	36	67	88	117	174
0.8(3327)	52	88	109	129	211
0.6(3823)	71	133	130	137	
0.4(4317)	171	180	168		174
1.4(5070)	95	51	93	118	128
1.2(5565)	65				
1.0(6060)		54	95	122	131
0.8(6753)	64	68	99	142	146
0.6(7545)	63	88	117	144	144
0.4(8634)	109	111	128		

[a] Original data of Figure 4.

Table S3. Transform-fault-based tearing pattern of stage 1 [a]. (unit: 1)

	0°	10°	20°	30°	40°
1.4(1318)	0.3	0.2	0.4	0.7	1.2
1.2					
1.0(1515)	0.1	0.4	0.4	0.7	1.2
0.8(1713)	0.4	0.5	0.4	0.8	1.3
0.6(1911)	0.5	0.6	0.4	0.7	
1.4(2535)	0.3	0.3	0.5	0.8	1.2
1.2(2733)		1.2	0.8	0.8	1.2
1.0(3030)	0.1	1.0	0.8	0.9	1.3
0.8(3327)	0.2	1	0.8	0.8	1.2
0.6(3823)	0.6	1	0.7	0.9	
0.4(4317)	0.8	0.9	0.8		1.3
1.4(5070)	0.2	0.9	1.5	1.6	5.2
1.2(5565)	0.1				
1.0(6060)		1.5	1.8	1.4	3.2
0.8(6753)	0	1.2	1.4	1.4	2.4
0.6(7545)	0.5	0.9	1.1	1.2	2.2
0.4(8634)	2.3	1.2	0.9		

[a] Original data of Figure 5.

Table S4. Transform-fault-based tearing pattern of stage 2 [a]. (unit: 1)

	0°	10°	20°	30°	40°
1.4(1318)	0.5	0.1	0.2	0.4	0.7
1.2					
1.0(1515)	2.2	0.3	0.2	0.4	0.7
0.8(1713)	0.6	0.5	0.3	0.5	1
0.6(1911)	0.4	0.5	0.5	0.6	
1.4(2535)	0.4	0	1.1	0.9	1.2
1.2(2733)		0.4	1.3	1.1	1.2
1.0(3030)	0.6	1	1.4	1.1	1.3
0.8(3327)	0.3	1	1.2	1.1	1.2
0.6(3823)	0.7	1.1	1	1.1	
0.4(4317)	1	1.1	1		1.1
1.4(5070)	0.2	0.6	2	1.9	2.1
1.2(5565)	0.1				
1.0(6060)		1.2	2.1	1.8	2.2
0.8(6753)	0.1	1.2	2.1	1.6	2.1
0.6(7545)	0.6	1.6	1.1	1.4	1.8
0.4(8634)	4.6	1.6	1		

[a] Original data of Figure 5.

Table S5. Trench-based tearing pattern of stage 1 [a]. (unit: 1)

	0°	10°	20°	30°	40°
1.4(1318)	0.3	0.1	0.1	0.1	0.2
1.2					
1.0(1515)	0.1	0.2	0.1	0.1	0.2
0.8(1713)	0.4	0.3	0.1	0.1	0.2
0.6(1911)	0.5	0.3	0.1	0.1	
1.4(2535)	0.3	0.1	0.2	0.2	0.2
1.2(2733)		0.8	0.3	0.2	0.2
1.0(3030)	0.1	0.7	0.3	0.2	0.2
0.8(3327)	0.2	0.7	0.3	0.2	0.2
0.6(3823)	0.6	0.7	0.3	0.2	
0.4(4317)	0.8	0.6	0.3		0.2
1.4(5070)	0.2	0.7	0.7	0.5	0.6
1.2(5565)	0.1				
1.0(6060)		1.0	0.8	0.5	0.6
0.8(6753)	0.0	0.8	0.7	0.5	0.5
0.6(7545)	0.5	0.6	0.5	0.4	0.5
0.4(8634)	2.3	0.8	0.4		

[a] Original data of Figure 12.

Table S6. Trench-based tearing pattern of stage 2 [a]. (unit: 1)

	0°	10°	20°	30°	40°
1.4(1318)	0.5	0.0	0.0	0.1	0.0
1.2					
1.0(1515)	2.2	0.2	0.1	0.1	0.0
0.8(1713)	0.6	0.3	0.1	0.0	0.1
0.6(1911)	0.4	0.3	0.2	0.1	
1.4(2535)	0.4	0.2	0.5	0.2	0.2
1.2(2733)		0.3	0.6	0.3	0.2
1.0(3030)	0.6	0.7	0.7	0.3	0.2
0.8(3327)	0.3	0.7	0.6	0.3	0.2
0.6(3823)	0.7	0.8	0.5	0.3	
0.4(4317)	1	0.8	0.5		0.1
1.4(5070)	0.2	0.4	0.9	0.6	0.5
1.2(5565)	0.1				
1.0(6060)		0.8	1.0	0.6	0.5
0.8(6753)	0.1	0.8	0.9	0.5	0.4
0.6(7545)	0.6	1.1	0.6	0.4	0.4

0.4(8634)	4.6	1.1	0.5

[a] Original data of Figure 12.

Table S7. Tearing pattern of natural cases, from literature [a].

symbol [b]	Tearing width perpendicular to convergence direction (km)	Tearing width along convergence direction (km)	Tearing pattern
cam-1	50	53.1	1.1
cam-2	95.7	40.6	0.4
car	34.5	66.9	1.9
sam-1 (at depth 1)	132.6	288.1	2.2
sam-1 (at depth 2)	163.7	300.7	1.8
sam-1 (at depth 3)	175.9	292.6	1.7

[a] Original data of Figure S3. [b] The same with Figure 1.

3. Additional figures associated with experimental results

The ridge setup is not a specific construction for a particular area but a more general setting. It consists of two layers: the crustal and the lithospheric mantle, and the distance from ridge to trench (ridge at the back) is 20 km. Table S9 represents some of the geometric and physical parameters of the oblique ridge subduction model in Figure S4-S6. Table S10 shows the specific values of the model results after changing the continental crust density and thermal conductivity, and the specific values of the results of the oblique ridge subduction model involved in Figure S4-S6.

Table S9. Material properties of the ridge.

Composition	Thickness (km)	Density (kg/m^3)	Viscosity (Pa·s)

ridge crust	22 [a]	3340 [b]	1.40E+22 [a]
ridge lithosphere mantle	the same with lithosphere mantle		
oceanic crust	12	3390	2.80E+20
lithosphere mantle	half-cooling model	3390	1.40E+23

[a] (Gerya et al., 2009). [b] (Martinod et al., 2013).

Table S10. Tearing width and tearing pattern of additional experiments.

stage 1 at different depths (km)	tearing width (km)	tearing pattern	average tearing pattern	stage 2 at different depths (km)	tearing width (km)	tearing pattern	average tearing pattern
3327_20 (A)				3327_20 (A)			
100	75	1.3		100	101	1.4	
200	67	0.7		200	102	1.2	
300	89	0.5	0.8	300	109	0.9	1.2
3327_20-thermal_conductivity (B)				3327_20-thermal_conductivity (B)			
100	72	1.4		100	98	1.4	
200	65	0.8		200	100	1.1	
300	86	0.4	0.9	300	103	0.9	1.1
3327_20-density (C)				3327_20-density (C)			
100	67	1.2		100	100	1.4	
200	67	0.6		200	105	1.1	
300	86	0.3	0.7	300	103	1.1	1.2
cal				cal			
100	66	2.1		100	55	3.9	
200	68	2.9		200	97	4.7	
300	75	1.4	2.1	300	95	3.4	
				400	104	1.5	3.4
izu				izu			
100	37	1.5		100	68	3.2	
200	65	4.7		200	86	4.7	
300	66	13.4	6.5	300	101	3.2	
				400	119	1.9	3.3
izu-with ridge				izu-with ridge			
100	36	2.1		100	54	3.2	
200	64	4.5		200	84	6.6	
300	61	28.9	11.8	300	94	3.2	
				400	121	2.1	3.8
sam2				sam2			
100	56	1.5		100	58	1.2	

200	61	0.9		200	76	1.0	
300	86	1.5	1.3	300	95	0.9	
				400	102	0.8	1.0
sam2-with ridge				sam2-with ridge			
100	44	1.6		100	53	1.3	
200	58	1.0		200	71	1.1	
300	89	1.5	1.4	300	92	1.0	
				400	106	0.9	1.1

(A) 3327_20: reference model, thermal conductivity 2 W/m/K, continental crust density 3350 kg/m^3. (B) 3327_20-thermal_conductivity: 5 W/m/K. (C) 3327_20-density: continental crust density 2800 kg/m^3.

References

Carciumaru, D., Ortega, R., Castellanos, J. C., & Huesca-Pérez, E. (2020). Crustal Characteristics in the Subduction Zone of Mexico: Implication of the Tectonostratigraphic Terranes on Slab Tearing. *Seismological Research Letters*, *91*(3), 1781–1793. https://doi.org/10.1785/0220190117

Gerya, T. V., Fossati, D., Cantieni, C., & Seward, D. (2009). Dynamic effects of aseismic ridge subduction: numerical modelling. *European Journal of Mineralogy*, *21*(3), 649–661. https://doi.org/10.1127/0935-1221/2009/0021-1931

Gianni, G. M., Navarrete, C., & Spagnotto, S. (2019). Surface and mantle records reveal an ancient slab tear beneath Gondwana. *Scientific Reports*, *9*(1), 19774. https://doi.org/10.1038/s41598-019-56335-9

Martinod, J., Guillaume, B., Espurt, N., Faccenna, C., Funiciello, F., & Regard, V. (2013). Effect of aseismic ridge subduction on slab geometry and overriding plate deformation: Insights from analogue modeling. *Tectonophysics*, *588*, 39–55. https://doi.org/10.1016/j.tecto.2012.12.010

Meighan, H. E., Pulliam, J., Brink, U. ten, & López-Venegas, A. M. (2013). Seismic evidence for a slab tear at the Puerto Rico Trench. *Journal of Geophysical Research: Solid Earth*, *118*(6), 2915–2923. https://doi.org/10.1002/jgrb.50227

Miller, M. S., Gorbatov, A., & Kennett, B. L. N. (2006). Three-dimensional visualization of a near-vertical slab tear beneath the southern Mariana arc. *Geochemistry, Geophysics, Geosystems*, *7*(6). https://doi.org/10.1029/2005GC001110

Pesicek, J. D., Engdahl, E. R., Thurber, C. H., DeShon, H. R., & Lange, D. (2012). Mantle subducting slab structure in the region of the 2010 M8.8 Maule earthquake (30–40°S), Chile. *Geophysical Journal International*, *191*(1), 317–324. https://doi.org/10.1111/j.1365-246X.2012.05624.x

Stubailo, I., Beghein, C., & Davis, P. M. (2012). Structure and anisotropy of the Mexico subduction zone based on Rayleigh-wave analysis and implications for the geometry of the Trans-Mexican Volcanic Belt. *Journal of Geophysical Research: Solid Earth*, *117*(B5). https://doi.org/10.1029/2011JB008631

Vargas, C. A., & Mann, P. (2013). Tearing and Breaking Off of Subducted Slabs as the Result

of Collision of the Panama Arc-Indenter with Northwestern South America. *Bulletin of the Seismological Society of America*, *103*(3), 2025–2046. https://doi.org/10.1785/0120120328